PUBLICATIONS OF
THE UNIVERSITY OF EASTERN FINLAND

Dissertations in Health Sciences

UNIVERSITY OF
EASTERN FINLAND

ELIAS YLÄ-HERTTUALA

CHARACTERIZING MYOCARDIAL INFARCTION USING NOVEL MAGNETIC RESONANCE IMAGING TOOLS

A comparison between a normal and an insufficient lymphatic circulation

CHARACTERIZATION OF MYOCARDIAL INFARCTION USING NOVEL MAGNETIC RESONANCE IMAGING TOOLS

A COMPARISON BETWEEN A NORMAL AND AN INSUFFICIENT LYMPHATIC CIRCULATION

Elias Ylä-Herttuala

CHARACTERIZING MYOCARDIAL INFARCTION USING NOVEL MAGNETIC RESONANCE IMAGING TOOLS

A COMPARISON BETWEEN A NORMAL AND AN INSUFFICIENT LYMPHATIC CIRCULATION

Publications of the University of Eastern Finland
Dissertations in Health Sciences
No 562

University of Eastern Finland
Kuopio
2020

Distributor:
University of Eastern Finland
Kuopio Campus Library
P.O.Box 1627
FI-70211 Kuopio, Finland
www.uef.fi/kirjasto

Grano, 2020

ISBN: 978-952-61-3375-1 (nid.)
ISBN: 978-952-61-3376-8 (PDF)
ISSNL: 1798-5706
ISSN: 1798-5706
ISSN: 1798-5714 (PDF)

Author's address: A.I. Virtanen Institute for Molecular Sciences
University of Eastern Finland
KUOPIO
FINLAND

Doctoral programme: Doctoral programme in Molecular Medicine

Supervisors: Associate Professor Timo Liimatainen, Ph.D.
Research Unit of Medical Imaging, Physics and Technology
University of Oulu
OULU
FINLAND

Adjunct Professor Mikko Kettunen, Ph.D.
A.I. Virtanen Institute for Molecular Sciences
University of Eastern Finland
KUOPIO
FINLAND

Professor Olli Gröhn, Ph.D.
A.I. Virtanen Institute for Molecular Sciences
University of Eastern Finland
KUOPIO
FINLAND

Reviewers: Professor Damian Tyler, Ph.D.
Department of Physiology, Anatomy & Genetics
University of Oxfrod
OXFORD
UNITED KINGDOM

Assistant Professor Walter Witschey, Ph.D.
Department of Radiology
University of Pennsylvania
PHILADELPHIA
UNITED STATES OF AMERICA

Opponent: Professor Gustav Strijkers, Ph.D.
Department of Biomedical Engineering and Physics
University of Amsterdam
AMSTERDAM
NETHERLANDS

Ylä-Herttuala, Elias
Characterizing myocardial infarction using novel magnetic resonance imaging tools – a comparison between a normal and an insufficient lymphatic circulation
Kuopio: University of Eastern Finland
Publications of the University of Eastern Finland
Dissertations in Health Sciences 562. 2020, 98 p.
ISBN: 978-952-61-3375-1 (nid.)
ISSNL: 1798-5706
ISSN: 1798-5706
ISBN: 978-952-61-3376-8 (PDF)
ISSN: 1798-5714 (PDF)

ABSTRACT

Cardiovascular diseases and ischemic heart diseases are the leading global causes of death. The most common cardiovascular disease is myocardial infarction (MI), which is caused by the occlusion of the coronary arteries preventing the flow of oxygen-rich blood to the myocardium. MI also leads to changes in the lymphatic system, which collects extracellular fluid from the tissues. The lymphatic system controls tissue fluid homeostasis and thus participates in many physiological and pathological processes. Surprisingly, the role of the lymphatic system in the development of MI has been rarely studied and has remained unclear. However, it has been hypothesized that edema increases after the MI in an insufficient lymphatic myocardium and therefore, this can be detected with medical imaging devices. Potentially, the cardiac lymphatic system may have a much more important role in the development of MI than previously believed.

Magnetic resonance imaging (MRI) is a non-invasive medical imaging modality, whose strength is its high soft tissue contrast with high spatial and temporal resolution without subjecting the patient to ionizing radiation. There are numerous ways to generate good contrast in an MR image. These ways are divided mainly into endogenous and exogenous contrasts. MRI is a versatile tool for imaging the heart since it can provide anatomical, functional and pathological information of the myocardial tissue. Traditionally, these approaches have been achieved by applying T_1 based anatomical, T_2 based edema imaging and the gadolinium-based late gadolinium enhancement (LGE) method to determine the presence of scar tissue in the myocardium.

The conventional relaxation times, T_1 and T_2, differ from rotating frame relaxation times ($T_{1\rho}$ and $T_{2\rho}$), where the relaxation occurs during the RF excitation. Both $T_{1\rho}$ and $T_{2\rho}$, have been shown to be more specific than for a fairly narrow range of slow microscopic molecular motions compared to T_2. However, $T_{1\rho}$ and $T_{2\rho}$ suffer from high tissue heating, which limits their use in the clinic.

A novel rotating frame relaxation time method called *relaxation along a fictitious field* (RAFF) was recently developed. Subsequently, RAFF has been extended into higher rotating frames, which is designed as *RAFF in the rotating frame of rank n* (RAFFn). The main reason to adopt higher rotating frames is to reduce tissue heating during the imaging by the tens of percents.

The aim of this thesis was to implement RAFFn in cardiac MRI *in vivo* and apply $T_{1\rho}$ and RAFFn methods to characterize MI without the need of contrast agents. This is the first time that RAFFn has been applied in heart imaging. Additionally, by exploiting different mouse models, new knowledge about fibrosis detection, and the role of cardiac lymphatic vessels during MI development has been obtained.

The findings of this thesis demonstrate that the characterization of chronic MI can be achieved with $T_{1\rho}$ mapping. In addition, we demonstrated the feasibility of using RAFFn to determine the fibrotic MI area in an MI area close to that measured with LGE in mice *in vivo*. Therefore, RAFFn has the potential to be used in the evaluation of MI without administration of contrast agents. Additionally, the cardiac lymphatic system was found to have an important role during the development of MI; these findings were confirmed by histology. In the future, these new methods may become routine in the diagnosis and treatment of myocardial infarction in clinical medicine.

National Library of Medicine Classification: WG 300, WG 310, WH 700, WN 185, WN 180, WG 141.5.M2, QY 60.R6
Medical Subject Headings: Heart; Myocardium; Myocardial Infarction; Lymphatic System; Magnetic Resonance Imaging; Diagnostic Imaging/Methods; Disease Models; Mice
Keywords: RAFFn, $T_{1\rho}$, T_2,

Ylä-Herttuala, Elias
Sydäninfarktin karakterisointi uusilla magneettikuvauksen menetelmillä – normaalin ja tehottoman lymfaattisen kierron vertaileminen sydänlihaksessa
Kuopio: Itä-Suomen yliopisto
Publications of the University of Eastern Finland
Dissertations in Health Sciences 562. 2020, 98 p.
ISBN: 978-952-61-3375-1 (nid.)
ISSNL: 1798-5706
ISSN: 1798-5706
ISBN: 978-952-61-3376-8 (PDF)
ISSN: 1798-5714 (PDF)

TIIVISTELMÄ

Sydän- ja verisuonitaudit sekä iskeemiset sydäntaudit ovat suurimpia kuolleisuuden aiheuttajia maailmanlaajuisesti. Yleisin sydän- ja versuonitaudeista on sydäninfarkti, joka aiheutuu sepelvaltimoiden tukkeutumisesta ja estää hapekkaan veren pääsyn sydänlihakseen. Sydäninfarkti aiheuttaa myös muutoksia sydänlihaksen lymfaattiseen järjestelmään. Lymfaattinen järjestelmä kokoaa ekstrasellulaarinesteen kudoksista ja kontrolloi nestetasapainoa osallistuen moneen fysiologiseen ja patologiseen prosessiin. Lymfaattisen järjestelmän rooli sydänlihaksen infarktin kehittymisen aikana on kuitenkin jäänyt lähes kokonaan tutkimatta ja epäselväksi. On hypotetisoitu, että ödeema lisääntyy sydäninfarktin jälkeen sydänlihaksessa missä on vajavainen lymfaattinen järjestelmä ja tämä ödeema on mahdollista havaita lääketieteellisten kuvantamislaitteiden avulla. Potentiaalisesti lymfaattisella järjestelmällä voi olla paljon merkittävämpi rooli sydäninfarktin patogeneesissä kuin mitä aikaisemmin on tiedetty.

Magneettikuvaus on kudokseen kajoamaton lääketieteellinen kuvantamismenetelmä, jonka vahvuutena on erittäin hyvä pehmytkudoskontrasti hyvällä spatiaalisella ja temporaalisella resoluutiolla. On monia erilaisia tapoja hallita kontrastia, jolla saadaan tuotettua magneettikuva. Kontrastin tuottaminen on yleensä jaettu joko sisäisiin tai ulkoisiin kontrasteihin. Useimmat tavat sisältävät kuvaustapahtuman parametrien muuttamista. Sydämen magneettikuvaus voidaan suorittaa esimerkiksi sydämen anatomian, toiminnan ja sydänlihaksen patologisen informaation kuvantamisella. Perinteisiä lähestymistapoja ovat T_1 pohjainen anatominen, T_2 pohjainen ödeeman kuvantaminen ja gadolinium-pohjainen kontrastiaine myöhäistehostumakuvaus aprikudoksen havaitsemiseen sydänlihaksessa.

Tavanomaiset relaksaatioaikamenetelmät, T_1 ja T_2 ovat erilaisia kuin pyörivän koordinaatiston relaksaatioaikamenetelmät ($T_{1\rho}$ ja $T_{2\rho}$), jossa relaksaatio tapahtuu RF pulssin aikana. $T_{1\rho}$ ja $T_{2\rho}$, ovat spesifisempiä melko kapealle hitaiden mikroskooppisten molekulaaristen liikkeiden alueilla verrattuna T_2. On kuitenkin osoitettu, että $T_{1\rho}$ ja $T_{2\rho}$ aiheuttavat kohdekudoksen lämpenemistä ja näin ollen rajoittavat niiden kliinistä käyttöä.

Uusi pyörivän koordinaatiston relaksaatioaikamenetlmä, nimeltään *relaxation along a fictitious field* (RAFF), on hiljattain kehitetty uusi menetelmä. Tässä väitöskirjatyössä RAFF on käytetty korkeamman asteen pyörivänä koordinaatistona, joka on nimeltään *RAFF in the rotating frame of rank n* (RAFFn). Korkeampien pyörivien koordinaatistojen käytön perusteena on kohdekudoksen lämpenemisen pienentäminen kuvauksen aikana.

Tämän väitöskirjatyön tavoitteena oli toteuttaa RAFFn hyödyntäminen sydämen kuvauksessa *in vivo* sekä $T_{1\rho}$ ja RAFFn menetelmien käyttäminen sydäninfarktin karakterisoinnissa. Lisäksi tässä väitöskirjassa käytettyjen erilaisten hiirimallien avulla on saatu uutta tietoa fibroosin havaitsemisesta sekä lymfasuonten roolista sydäninfarktin kehittymisessä.

Tämän väitöskirjan löydökset osoittavat kroonisen sydäninfarktin karakterisoinnin onnistuvan $T_{1\rho}$ relaksaatioaikakartan avulla. Lisäksi löydökset osoittavat luotettavan tarkasti RAFFn toimivan fibroottisen sydäninfarktin kuvantamisessa yhtä hyvin kuin kontrastiainepohjainen myöhäistehostumakuvas. Näin ollen RAFFn on potentiaalinen menetelmä sydäninfarktin määrittämiseen ilman kontrastiaineita. Lisäksi havaittiin, että sydämen lymfaattisella järjestelmällä on tärkeä rooli sydäninfarktin kehittymisessä ja nämä löydökset vahvistettiin histologian avulla. Nyt kehitettyjä uusia sydämen kuvantamismenetelmiä voitaneen tulevaisuudessa käyttää kliinisessä lääketieteessä parantamaan sydäninfarktin diagnostiikkaa ja hoitoa.

Luokitus: WG 300, WG 310, WH 700, WN 185, WN 180, WG 141.5.M2, QY 60.R6
Yleinen suomalainen asiasanasto: sydän; sydäninfarkti; magneettikuvaus
Avainsanat: Lymfaattinen järjestelmä, RAFFn, $T_{1\rho}$, T_2

To my beloved family

ACKNOWLEDGEMENTS

This study was done in the Cardiovascular Imaging group in the Biomedical Imaging Unit of the A.I. Virtanen Institute for Molecular Sciences in the University of Eastern Finland. I am sincerely thankful to all the people with whom I have worked in these years and who have contributed to my research.

First of all, I would like to thank my principal supervisor, Associate Professor Timo Liimatainen, Ph.D. I am grateful that he gave me the opportunity to work in his research team. His support and guidance throughout the process have been extremely helpful to me. I am also grateful to my second supervisor Adjunct Professor Mikko Kettunen, Ph.D., for sharing his vast knowledge about MRI and MRI devices. I would like to thank my third supervisor Professor Olli Gröhn, Ph.D., for his expert guidance and for allowing me to be a part of his Biomedical Imaging Unit group.

My sincere thanks go to the official reviewers of this thesis, Professor Damian Tyler from the University of Oxford and Assistant Professor Walter Witschey from the University of Pennsylvania whose contsructive comments helped me to improve this thesis. I am honored that Professor Gustav Strijkers has accepted the invitation to be my opponent at the public defence. I also want to thank Ewen MacDonald for the language revision.

I would like to thank all the current and former members of the Cardiovascular Imaging and Bio-NMR groups for great advices, discussions and the companionship. I truly enjoyed working with you! Especially I want to thank Hanne Laakso for her help at the magnet, in the lab and in the office. I am grateful that I have been able to work with you! I also want to thank my roommates Viivi Hyppönen and Ali Abdollahzadeh for the great discussions and friendship during these years.

I would like to thank all the researchers in the SYH group with whom I was able to do great research. Especially, I wish to thank Taina Vuorio for great collaboration during these hectic years. Your optimism, innovative and outstanding ideas saved us many times from catastrophy! I also want to thank Svetlana Laidinen for being all the time so positive and whose magic fingers performed such excellent and irreplaceable work in the animal operations. I want to send special thanks I want to say to Mohan Babu and Annakaisa Tirronen, whose collaborations with incredible discussions have been very important to me. My sincere gratitude goes to the excellent secretary Helena Pernu whose help has been so significant during these years. I also want to thank Jokke for great company and friendship during the many years, which we have spent together.

My deepest gratitudes goest to all of my lovely friends. To all the people in the OOK group, I am grateful to have you in my life and be able to relax in your company! I want to send a special thanks to all my current and former teammates from the ice hockey rink for great friendship and the good times that we have spent together! I also want to thank Family Issukka for the incredible times that we have

spent together. Family Vatanen has a special place in my heart and it has been an honour to be able to spend lovely times with you! I also want thank Family Selinummi for the outstanding companionship with all the high level discussions and support. I also want to kindly thank my parents-in-law Eija and Pentti, sister-in-law Saana and her partner Teemu, and brother-in-law Henri; I am so pleased that I have met you and got to know you and the life in Lapland. The holidays with you have fully relaxed me and I have enjoyed your company so much!

Sincere and special thanks are sent to my parents Marja and Seppo who have always supported and believed in what I have been doing. This thesis would have never been completed without their deep kindness, guidance and love. My deepest gratitude and respect goes to my big brother Aleksi, whose support has been priceless; you have a special place in my mind and heart is permanent!

Finally, my deepest and most sincere thanks go to my loving wife Salla and our perfect daughter Hilla. Hilla, your smile, utterances and actions have melted my heart! Salla, your companionship and the joy, happiness and love are the best thing that has happened to me! I love you Salla today more than yesterday but not as much as tomorrow! Thank you Salla for being so supportive and understanding of the long working days, evenings and nights spent with my hobbies, which have taken a lot of our time. Thank you for believing in me at every step in my personal and our mutual journeys! Hopefully I can do the same for you!

This work has been funded by the Doctoral Program of Molecular Medicine of the University of Eastern Finland, Instrumentarium Foundation, Veritas Foundation, Aarne and Aili Turunen Foundation, Finnish Foundation for Cardiovascular Research, Ida Montin Foundation, Antti and Tyyne Soininen Foundation, Kuopio University Foundation, and Finnish Cultural Foundation.

Kuopio, 7th April 2020

Elias Ylä-Herttuala

LIST OF ORIGINAL PUBLICATIONS

This dissertation is based on the following original publications:

I Musthafa HS, Dragneva G, Lottonen L, Merentie M, Petrov L, Heikura T, **Ylä-Herttuala E**, Ylä-Herttuala S, Gröhn O, Liimatainen T. Longitudinal rotating frame relaxation time measurements in infarcted mouse myocardium in vivo. Magnetic Resonance in Medicine 69(5):1389-1395, 2013

II **Ylä-Herttuala E**, Laidinen S, Laakso H and Liimatainen T. Quantification of myocardial infarct area based on T_{RAFFn} relaxation time maps – comparison with cardiovascular magnetic resonance late gadolinium enhancement, $T_{1\rho}$ and T_2 in vivo. Journal of Cardiovascular Magnetic Resonance 20(1):34, 2018

III Vuorio T, **Ylä-Herttuala E**, Laakkonen JP, Laidinen S, Liimatainen T, Ylä-Herttuala S. Downregulation of VEGFR3 signaling alters cardiac lymphatic vessel organization and leads to a higher mortality after acute myocardial infarction. Scientific Reports 8:16709, 2018

IV **Ylä-Herttuala E**, Vuorio T, Laidinen S, Ylä-Herttuala S and Liimatainen T. Lymphatic insufficiency increases cardiac edema and has distinct fibrosis content after myocardial infarction as assessed by magnetic resonance T_{RAFFn} and T_2 relaxation times. Under review.

The publications were adapted with the permission of the copyright owners.

CONTENTS

ABBREVIATIONS

AFP	Adiabatic Full Passage
AHP	Adibatic Half Passage
AOD	Area Of Difference
AOE	Area Of Overestimation
B_0	Static Magnetic Field
B_1	RF Magnetic Field
BW	Bandwidth
CA	Contrast Agent
CO	Cardiac Output
CVD	Cardiovascular Disease
CW	Continuous Wave
ECG	Electrocardiogram
EF	Ejection Fraction
EDV	End Diastole Volume
ESV	End Systole Volume
FISP	Fast Imaging with balanced Steady state Precession
Gd	Gadolinium
H_1	Effective Magnetic Field
HS	Hyperbolic Secant
LGE	Late Gadolinium Enhancement

LV	Left Ventricle
LAD	Left Anterior Descending
MI	Myocardial Infarction
MRI	Magnetic Resonance Imaging
NMR	Nuclear Magnetic Resonance
RAFF	Relaxation Along a Fictitious Field
RAFFn	Relaxation Along a Fictitious Field in the nth rotating frame
RRTD	Relative Relaxation Time Difference
RF	Radiofrequency
SAN	Sinoatrial Node
SAR	Specific Absorption Rate
S	Spin angular momentum vector
SL	Spin-Lock
SV	Stroke Volume
TE	Echo Time
TI	Inversion Time
TR	Repetition Time
TSL	Time-spin-lock
T_1	Longitudinal relaxation time
T_2	Transversal relaxation time
$T_{1\rho}$	Longitudinal rotating frame spin-lock relaxation time
VEGF	Vascular Endothelial Growth Factor

1 INTRODUCTION

Cardiovascular disease (CVD) and in particular myocardial infarction (MI) are the leading cause of death all around the world (Global Health Estimates 2016, Mozaffarian D et al. 2015). MI occurs when coronary artery is completely or partially blocked and this leads to arrhythmia, a prolonged absence of perfusion and chronic inflammation (Blankesteijn WM et al. 2001; Ertl G et al. 2005). The absence of perfusion will mean that the myocardium suffers from a lack of oxygen, which causes the loss of myocytes, triggers harmful remodeling of the myocardium including the formation of fibrosis and collagen and eventually finally leading to heart failure (Ertl G et al. 2005; Virag JL et al. 2003). The prevention of CVD is still challenging since major clinical symptoms are lacking during the early phase of CVD progression.

The lymphatic system collects extracellular fluid from the body and the myocardium and thus it has exerts effects on cardiac physiology and pathology such as maintaining tissue fluid balance and regulating inflammation (Huang LH et al. 2017). When the function of lymphatic system is disturbed, e.g. due to a malfunctioning vascular endothelial growth factor (VEGF) receptor 3 for VEGF-C and VEGF-D ligands, it has effects on the function of myocardium (Yla-Herttuala S et al. 2007). However, the effects of the lymphatic system on the pathogenesis of MI development have only occasionally been evaluated and these have often consisted of assessing the disturbance of fluid balance, which has been changed by the reduced carcdiac output (Huang LH et al. 2017; Yla-Herttuala S et al. 2007).

Magnetic resonance imaging (MRI) is a non-invasive medical imaging method, which has excellent soft tissue contrast and high spatial and temporal resolution to image anatomy and function of tissue (McRobbie DW et al. 2007; Haacke EM et al. 1999). Additionally, MRI does not require ionizing radiation, in contrast to computed tomography (McRobbie DW et al. 2007) or the administration of radioactive tracers, like in positron-emission tomography and single-photon emission computed tomography (McRobbie DW et al. 2007; Haacke EM et al. 1999). The basis of MRI was established as nuclear magnetic resonance (NMR) in 1946 (Bolch et al. 1946; Purcell et al. 1946) and the first NMR image was collected in 1973 (Lauterbur 1973). After these milestones and the development of technologies, MRI has become one of the main imaging modalities in clinical use all around the world.

MRI can be used beneficially with high flexibility in several ways for imaging of biological tissues of any age. It is capable for repeated images e.g. for monitoring disease development and for assessing therapy outcomes, which are all processes which change the detectable contrasts of specific tissue or events. The contrasts obtained with conventional MRI rely on proton density, T_1 and T_2 relaxation time (McRobbie DW et al. 2007, Haacke EM at el. 1999). T_1 weighted MR image is generally referred to as an anatomical image and T_2 weighted MR image is sensitive to the amount of water content in the tissue, which can change due to pathological processes, such as inflammation and edema (McRobbie DW et al. 2007).

Endogenous relaxation methods are used clinically for the assessment of many diseases. However, endogenous contrasts for the specific pathologies *in vivo* have not worked effectively, for example in the case of MI. Nonetheless, MRI can reveal in a visual manner the differences between disease processes and their surroundings by exploiting different kinds of intrinsic contrasts. Novel MRI methods have been devised to develop and improve the detection of different pathologies, since it is vital to distinguish the diseased area and its structures from its healthy surroundings. MRI has a high potential to achieve the differentiation of MI from remote and healthy areas in the myocardium. However, it would be even more advantageous to be able to reveal different pathological states from each other, e.g. differentiating edema and inflammation from fibrosis and necrosis. If one wishes to visualize these different pathological states, one needs to have specific and quantitative characterization tools. Additionally, diagnostic tools are needed for differentiating the stages of disease progression from its earliest state of disease all the way through to clinically severe symptoms. Conventional MRI methods, e.g. including T_1 and T_2 relaxation time mappings, are non-specific for the determination of different pathological states. Therefore, novel MRI methods have been developed to create new endogenous contrasts; these, should provide more detailed information about the different pathological states. A longitudinal rotating frame spin-lock relaxation time method called $T_{1\rho}$ has demonstrated the potential to determine the MI area without using gadolinium (Gd) based contrast agents (Witschey WR et al. 2010, Stoffers RH et al. 2017, van Oorschot JWM et al. 2014). Clinically, weak spin-lock pulse powers can be applied to improve specificity what can be gained with T_2 in MI imaging; however, a much higher contrast between the MI area and the myocardium can be obtained if stronger spin-lock pulse powers are used (Witschey WR et al. 2010; van Oorschot JWM et al. 2015). Nonetheless, one critical limitation of the $T_{1\rho}$ method in a clinical setting is its relatively high specific absorption rate (SAR). SAR describes the energy absorbed into tissue i.e. heating of the tissue during the imaging (Witschey WR et al. 2010; van Oorschot JWM et al. 2015).

One relaxation time method to reduce SAR in the rotating frame of reference is Relaxation Along a Fictitious Field (RAFF) (Liimatainen T et al. 2010). The RAFF in the nth rotating frame of reference, called RAFFn, was introduced recently (Liimatainen T et al. 2015). It uses amplitude and frequency-modulated radiofrequency (RF) pulses in a sub-adiabatic regime. Reduced SAR is obtained with RAFF by exploiting the fictitious field as a component of a spin-locking field (Liimatainen T et al. 2010). The relaxation time of RAFFn method, called T_{RAFFn}, has demonstrated the potential to reveal more detailed information about the different myocardium pathologies in comparison with conventional T_1 and T_2 relaxation times and longitudinal rotating frame $T_{1\rho}$ relaxation time methods. Nonetheless, few studies have been done with RAFFn to characterize the properties of the myocardium (Ylä-Herttuala E et al. 2019), which include imaging of MI and hypertrophic myocardium (Khan MA et al. 2018). In the MI study, it was found that T_{RAFFn} was increased when edema was present in the myocardium, which is suggesting that T_{RAFFn} could be also increased in insufficient lymphatic myocardium after the MI.

The aim of this thesis was to characterize MI in a normal and an insufficient lymphatic myocardium with $T_{1\rho}$ and RAFFn MRI tools. $T_{1\rho}$ and RAFFn relaxation time mapping was used to investigate MI development at various time points after MI in different mouse models *in vivo*. Comparisons of novel MRI findings to conventional MRI tools, contrast agent imaging and histology were also performed.

2 REVIEW OF THE LITERATURE

2.1 MAGNETIC RESONANCE IMAGING, MRI

2.1.1 Theoretical basis of Nuclear Magnetic Resonance

The basis of NMR and MRI is in nuclei that have an intrinsic non-zero angular momentum and magnetic dipole moment properties e.g. due to mass and charge. Rotating nuclei with odd atomic mass numbers, have a spin angular momentum vector (S) that renders as them the source of the NMR signal. From the MRI point of view, the most important nuclei is that of hydrogen (^{1}H) in water, fat and other organic molecules, which are present in the various environments in different tissues. ^{1}H has the simplest atomic nucleus with only one proton and no neutrons and its S exists in two quantized states, $\pm 1/2\hbar$, where $\hbar$ is the Planks' constant, $\hbar = 1.054 \cdot 10^{-34}$ Js, divided by 2π (Levitt MH 2008). In the absence of an external magnetic field ($\mathbf{B_0}$), ^{1}Hs are randomly oriented (Figure 1A). When ^{1}Hs are placed into $\mathbf{B_0}$ (Huettel SA et al 2004), according to quantum mechanics, ^{1}Hs have $2S+1 = 2$ possible energy eigenstates, which are depending on $\mathbf{B_0}$ (Haacke EM et al. 1999) (Figure 1). Therefore, $\mathbf{B_0}$ influences the ^{1}H magnetic dipole-dipole condition and moments and causes the precession of the ^{1}H about the $\mathbf{B_0}$ field direction (Haacke EM et al. 1999). The precessing motion of ^{1}H can be understood as a spinning gyroscope that is also electrically charged, which is capable of interacting with $\mathbf{B_0}$ as well as producing its own magnetic field known as the magnetic dipole moment vector (Haacke EM et al. 1999). Therefore, magnetic dipole moment causes that S is aligned either in parallel (+ ½ i.e. lower energy state) or in anti-parallel (- ½ i.e. higher energy state) to the $\mathbf{B_0}$ (Figure 1). The difference between lower and higher energy states (Figure 1B) depends linearly on the magnitude of $\mathbf{B_0}$ as described

$$\Delta E = \gamma \hbar B_0 \, , \qquad (1)$$

where γ is the gyromagnetic ratio of nucleus. For ^{1}H, $\gamma = 2.675 \cdot 10^8$ rad/s/T. Boltzmann distribution describes the population ratio of the two states

$$\frac{n_-}{n_+} = e^{-\frac{\Delta E}{kT}} \, , \qquad (2)$$

where n_- and n_+ are the numbers of S in anti-parallel and parallel states, respectively, $k = 1.38066 \cdot 10^{-23}$ J/K is the Boltzmann constant, and T is the temperature in degrees Kelvin. The ratio in Eq (2) is also known as the thermal equilibrium. Although the ratio in Eq (2) is close to unity at room temperature since the thermal energy is millions of times larger than quantum energy difference (Eq (1)), there is still a slightly higher fraction of S in the parallel state than in the anti-parallel state and the difference in spin populations leads to a detectable NMR signal. Since all systems have more + ½ *S*s than - ½ *S*s from all possible ^{1}Hs when $\mathbf{B}_0$ is affecting them, at the macroscopic level, the sum of all nuclei *S*s in a unit volume forms the net magnetization $\mathbf{M}_0 = [M_{x0}, M_{y0}, M_{z0}]$, which can be thought as the component of the magnetic moment vector along the $\mathbf{B}_0$ (Figure 1A). $\mathbf{M}_0$ is aligned in parallel to $\mathbf{B}_0$ and precesses around $\mathbf{B}_0$ with a specific angular frequency called the Larmor frequency:

$$\omega_0 = -\frac{\gamma}{2\cdot\pi} B_0 \,, \qquad (3)$$

which is derived from the energy difference between the states (Haacke EM et al. 1999).

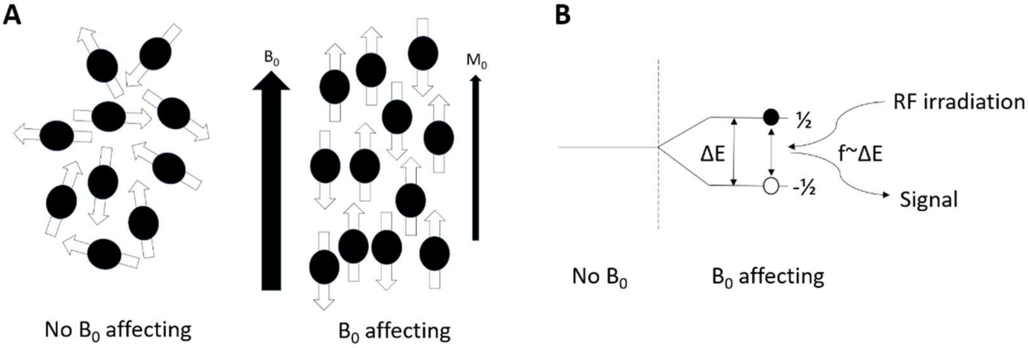

Figure 1. A schematic view of energy states for spin ±½ particles placed in an external magnetic field and the formation of net magnetization (A) and also the energy difference between the energy states (B).

The $\mathbf{M}_0$ along $\mathbf{B}_0$ cannot be detected, so the $\mathbf{M}_0$ needs to be perturbed from thermal equilibrium *z*-direction towards the *xy*-plane with an external burst of energy. The perturbation is achieved with electromagnetic radiation at or close to the Larmor frequency. The frequency is at radiofrequency (RF) and consequently perturbing electromagnetic radiation is called RF. It is produced by the transmit coil, which is located nearby (Haacke EM et al. 1999). In the classical way of thinking, the external energy burst, or the RF pulse forms magnetic field ($\mathbf{B}_1$) that gives the necessary energy to $\mathbf{M}_0$ to move from the *z*-direction towards the *xy*-plane. This phenomenon is known as the excitation of the spin population. The $\mathbf{B}_1$ field is applied perpendicular to $\mathbf{B}_0$, and it rotates with the Larmor frequency around the $\mathbf{B}_0$. This induces the tilting of $\mathbf{M}_0$ towards the *xy*-plane. The magnetic field produced by the precessing spin population with the **M** is changing the magnetic flux and this is detected by induction of an electromotive force (emf), as a voltage in the nearby receiver coil (Haacke EM et al. 1999). The tilt angle, or flip angle, between **M** and *z*-axis is determined as

$$\theta = \gamma B_1 t\,, \quad (4)$$

where t is the duration of the RF pulse (Haacke EM et al. 1999; Bernstein MA et al. 2004).

The motion of **M** after the RF pulse can also be described in the rotating frame of reference, where the reference frame is rotating around the z-axis with the Larmor frequency and **M** is therefore stationary. When the frequency of **B$_1$** does not match the Larmor frequency (i.e. it is off-resonance), the components of the effective magnetic field **H$_1$**(t) are the **B$_1$** field and the field component from off-resonance $\Delta B(t) = \gamma^{-1} \cdot [\omega_0 - \Delta\omega_{RF}(t)]$, given by the difference between the frequency of the RF pulse and the Larmor frequency (in rad/s). Then **M** is precessing and rotating around **H$_1$**, whose amplitude is defined as

$$H_1(t) = \sqrt{B_1^2(t) + \Delta B^2(t)}\,. \quad (5)$$

The **B$_1$** field consists of both magnetic and electric field components. The magnetic field component interacts with **M**, while the electric field component creates the potential source of energy deposition in the tissue.

2.2 RELAXATION IN THE LABORATORY FRAME

When the RF irradiation is switched off, **M** starts to relax towards the initial equilibrium state while it precesses around the **B$_0$**. After the RF pulse, excited spin populations are returning to the original state releasing the absorbed energy to the surroundings. The xy-plane components of **M** induces an emf, which is detectable with a receiver coil nearby. The signal is known as the free induction decay (FID) (Nishimura DG 2010). During the relaxation back to thermal equilibrium, we can observe a longitudinal spin-lattice (T_1) and transversal spin-spin (T_2) relaxation. These relaxation mechanisms are used to generate MRI contrasts.

2.2.1 Longitudinal Relaxation

The recovery, or the rate of the regrowth, of component M_z from **M** to initial thermal equilibrium after RF irradiation is called longitudinal relaxation or T_1 relaxation. This recovery, or relaxation, depends on the interaction between spin populations and their atomic surroundings. Thus this relaxation is called the spin-lattice relaxation. The recovery of **M** is described by

$$M_z(t) = M_z(0)e^{-\frac{t}{T_1}} + M_0\left(1 - e^{-\frac{t}{T_1}}\right), \qquad (6)$$

which is a solution of the famous Bloch equation in the direction of z-axis (Haacke EM et al. 1999; Nishimura DG 2010). We can see from Eq (6) that the recovery is expressed as exponential growth where the time constant T_1 characterizes the growth rate.

At the microscopic level, the spin population in a unit volume and its atomic surrounding lattice experiences some molecular motion, for example vibration and rotation, which are slightly fluctuating the magnitude and the direction of the local magnetic field of *S*. The origin of T_1 relaxation lies in these dipole-dipole interactions between the spin population in a unit volume and its atomic surroundings. Thermal motion is formed by magnetic moments of molecular lattice in $\mathbf{B}_0$ and viscosity between adjacent molecular lattices. Interactions between adjacent molecular lattices can induce some molecular motion between adjacent molecular lattices, which can be described by the spectral density function. The spectral density function shows the distribution of correlation times of molecular motions and its form for spin-lattice relaxation is (Gadian DG 1995)

$$J(\omega) = \frac{\tau_c}{1+\omega^2\tau_c^2}, \qquad (7)$$

where ω is the angular frequency of the motion and τ_c is the correlation time, which describes the rate of microscopic molecular tumbling. τ_c describes the time what it takes for a molecule to rotate one radian. τ_c is in 9.4 Tesla about 10^{-6}-10^{-9} s for water molecule meaning that the water is loosely bounded as compared to free water molecule which τ_c is around 10^{-12}. The T_1 and τ_c are connected by

$$\frac{1}{T_1} = K[J(\omega_0) + 4J(2\omega_0)], \qquad (8)$$

where $K = 3 \cdot \mu_0^2 \cdot \hbar^2 \cdot \gamma^4 \cdot (160 \cdot \pi^2 \cdot r^6)^{-1}$ is a constant, which includes the information of the local field fluctuations and the average distance between spin populations at "fluid" system where there is an assumption of $\tau_c << T_1$ (Cowan B. 1997). In the case where molecular motion is close to ω_0 frequency, the energy level transitions and also the energy exhange between the spin populations and the lattice is at its most efficient. This causes the **M** to return to a thermal equilibrium with the most rapid rate. Therefore, T_1 relaxation is the most sensitive to molecular motions, which occur at close to the Larmor frequency.

Typical MRI pulse sequences to measure T_1 relaxation are saturation recovery (SR) and inversion recovery (IR) as shown in Figure 2. In the SR sequence, flipping of **M** into the *xy*-plane is repeated so that M_z is allowed to recover a defined repetition time (TR), which leads to partial saturation of the signal. Thus, by varying TR, the time between two separate RF pulses in repeated measurements of SR sequence, T_1 relaxation can be quantified. In the IR sequence, a 180° RF pulse first inverts the **M** into the direction of –*z*. The time between inversion and excitation of 90° RF pulse, which is the classical way to conduct IR measurements, is called the inversion time (TI) and during this time, the signal is recovering through T_1 relaxation. After this 90° RF pulse the signal is measured. T_1 can be quantified by varying TI values in IR sequence.

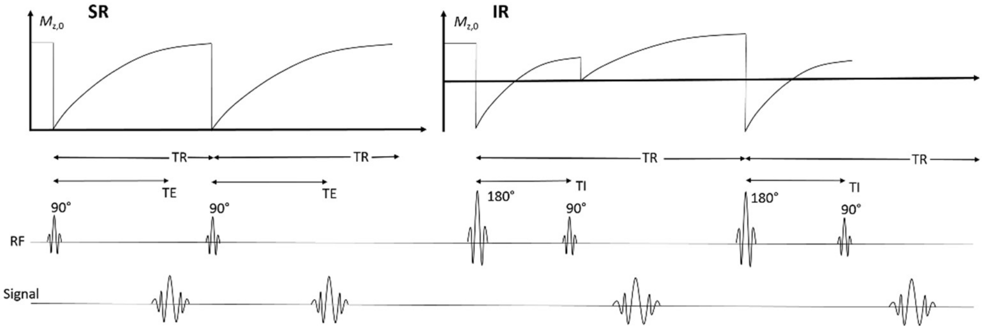

Figure 2. On the left, a schematic view of the start of saturation recovery (SR) sequence and on the right, the start of inversion recovery (IR) sequence, which are typically used to measure the T_1 relaxation time. M_{z0}: the net **M** in *z*-direction.

2.2.2 Transversal Relaxation

The decay of the transversal component of **M** (M_{xy}) after the RF pulse is characterized by its T_2 relaxation time, or spin-spin relaxation time. The origin of T_2 relaxation is a spin-spin interaction or energy exchange between the nuclei, not with the surrounding lattice as in T_1. There are also other processes contributing to T_2 relaxation time such as microscopic and macroscopic interactions including diffusion through local field gradients and chemical exchange.

M consists of a large number of *S*s that are precessing independently on their Larmor frequencies both during and immediately after the RF irradiation. The surroundings of nuclei e.g. intramolecular and intermolecular dipolar interactions are slightly different leading to a different local magnetic field for each nucleus. This is reflected as differences in their Larmor frequencies. After RF irradiation is turned off, the differences in local Larmor frequencies lead to an increase in the phase incoherence between spin populations. The surroundings of nuclei and their orientation with respect to $\mathbf{B_0}$ influence the total magnetic field what they experience. This frequency distribution is the key to the loss of the phase coherence, known as dephasing, between the spin populations. This will lead to a dispersion of the phases and therefore, the disappearance of the M_{xy} and the detectable signal.

The time constant T_2 describes the rate of the exponential decay of transversal component $\mathrm{M_{xy}}$ of **M** (Nishimura DG 2010):

$$M_{xy}(t) = M_{xy}(0)e^{-\frac{t}{T_2}}, \qquad (9)$$

where $M_{xy}(0)$ is the initial transversal component of **M**. In addition, T_2 and correlation time has a connection (Levitt 2008)

$$\frac{1}{T_2} = \frac{K}{2}[3J(0) + 5J(\omega_0) + 2J(2\omega_0)]. \qquad (10)$$

Therefore, the transversal relaxation is most effective, or the decay is fastest, when the correlation time is long, and the molecular motion is slow (i.e. close to ω_0).

T_2 relaxation is different in solid and in liquid environments (Nishimura DG 2010). However, in both solid and liquid environments, all of the possible orientations of ^{1}Hs can exist but the distribution of possible orientations are more constricted in a solid environment than in liquid environment. In a solid environment, the motional interactions between adjacent ^{1}Hs are not averaged away, whereas in a liquid environment, ^{1}Hs and molecules are rotating, vibrating, and tumbling, and thus experiencing greater motional averaging. Therefore, a solid environment supports a more rapid decay of M_{xy} as compared to a liquid environment. Therefore, for example the presence of edema or extracellular fluid in a tissue increases the T_2 relaxation time.

Static field inhomogeneities together with spin-spin interactions, induce dephasing. For example, sources of static inhomogeneities are magnetic susceptibility differences between adjacent samples (i.e. bone vs. air) or $\mathbf{B}_0$ inhomogeneities. The energy exchange between adjacent spin populations is a random process where random molecular motion occurs in combination with static dephasing and susceptibility differences due to local field gradients, which is known as the T_2^* mechanism. When there are multiple randomly precessing nuclei next to each other, the dephasing effect is increasing; this leads to a decreased signal. For example, dynamic dephasing is caused by the proton exchange. Proton exchange means that the proton is changing its location and its local magnetic field changes, which leads to more signal dephasing and faster relaxation. The net effect of all of the factors influencing the signal decay is characterized by T_2^* constant

$$\frac{1}{T_2^*} = \frac{1}{T_2} + \frac{1}{T_2'}, \quad (11)$$

where T_2' includes the net effect of static inhomogeneities.

There are two typical measurement types to refocus spin populations and therefore to measure T_2 relaxation. One refocusing method is spin-echo (SE) and the other is gradient echo (GE) (Figure 3). In the SE sequence (Hahn 1950), the T_2 measurement starts with RF excitation and after the first RF pulse, *S*s next to each other lose the coherence of precession and start to dephase. The idea of refocusing is that it reverses the effects of static dephasing and it is performed by applying the 180° RF pulse. *S*s are refocused and then the echo signal is acquired (Figure 3). The time between 90° RF pulse and the signal acquisition is called echo time (TE). Therefore, the duration of TE affects the intensity of the obtained signal T_2 relaxation time is calculated based on the data acquired with different TE values. The selection of TE values is crucial since TE determines how much the measured signal contains dynamic dephasing effects. This is important because a variation of TE values alters the sensitivity of measured T_2 signal to different relaxation processes such as proton exchange and diffusion. T_2 can be determined also with the multi-echo sequence (for example Carr HY et al. 1954) where multiple spin-echoes are used, and the data is collected after each refocusing pulses.

GEs are another way to deliberately refocus the neighbouring spin populations for spatial encoding purposes. In the GE, instead of a 180° refocusing pulse, the refocusing is done with field gradient system (Haacke EM et al. 1999) (Figure 3). Here, after the slice selective RF pulse, a gradient with an opposing sign compared to the slice selective gradient is turned on, allowing the formation of a readout dephase-rephase pair. Generally, it is possible to use shorter TE values in the GE sequence as compared to SE sequence. In other words, the relaxation occurring in GE sequence is measured as T_2^*, not as T_2 as in the SE sequence.

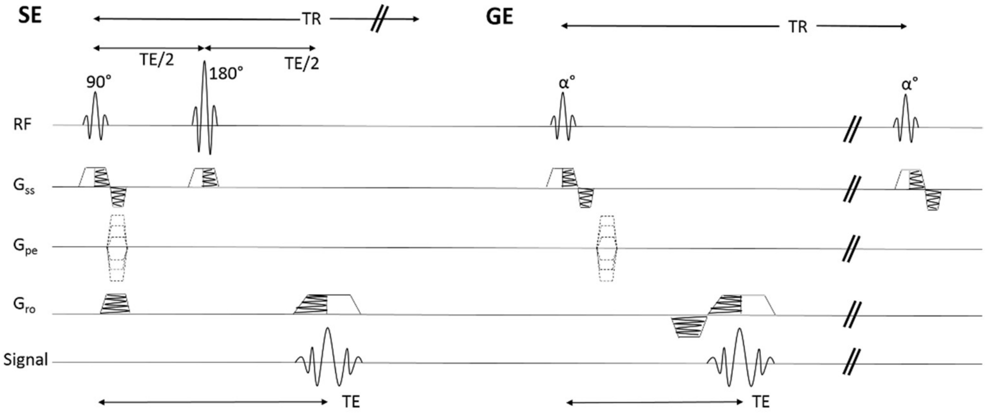

Figure 3. On the left, a schematic view of spin echo (SE) sequence and on the right, gradient echo (GE) sequence, which are typically used in MRI. G_{SS}: slice selection gradient, G_{PE}: phase encoding gradient, G_{RO}: readout gradient.

2.3 ROTATING FRAME RELAXATION

Relaxation in the rotating frame of reference was introduced in the NMR field (Redfield AG. 1955; Ailion DC et al. 1965; Jones GP. 1966) and later in the MRI field (Sepponen RE et al. 1985). The rotating frame of reference was developed to simplify the analysis and visualization of **M** by eliminating the rotation of the Larmor frequency. The main idea behind the rotating frame of reference is that the reference is rotating around the *z*-axis with the Larmor frequency, which causes **M** to be stationary in this frame of reference. This rotating frame of reference is denoted as *x′*, *y′* and *z′*.

The component of **M**, which is parallel to $\mathbf{H}_1$ relaxes with the $T_{1\rho}$ time constant during the RF irradiation (Figure 4). If the component of **M** is perpendicular to $\mathbf{H}_1$, it relaxes with $T_{2\rho}$ time constant during the RF irradiation (Figure 4).

The relaxation time constant $T_{1\rho}$ is also known as longitudinal or T_1 relaxation in the rotating frame. The simplest form of $T_{1\rho}$ measurement is the on-resonance spin-lock (SL) measurement. In this case, **M** is first flipped to the *xy*-plane and *S*s are then locked with the RF irradiation for a specific time duration, which is called the time-spin-lock (TSL). If **M** has some precessing, transverse **M** parts in the direction of $\mathbf{B}_1$ field and it is initially along $\mathbf{H}_1$ field with the resonance frequency, and then **M** relaxes according to the equation (Cowan E. 1997)

$$M(t) = M_0(t)e^{-\frac{TSL}{T_{1\rho}}}. \qquad (12)$$

Dipolar interactions affecting the $T_{1\rho}$ relaxation time at close to the Larmor frequency can be described by

$$\frac{1}{T_{1\rho}} = \frac{K}{2}\left[3J\left(2\omega_{H_1}\right) + 5J(\omega_0) + 2J(2\omega_0)\right], \qquad (13)$$

where is ω_{H_1} the angular frequency of the effective SL field (Jones GP. 1966, Cowan E. 1997). Since the $T_{1\rho}$ relaxation occurs during the RF pulse, the $T_{1\rho}$ relaxation is sensitive to a slow molecular motion, which is dependent on the used RF pulse power with the range of zero to few kHz. This means that τ_c is between 10^{-1}-10^{-5} s and thus water molecule is now tightly bounded. Therefore, the fastest $T_{1\rho}$ relaxation occurs when the irradiated SL frequency ($H_1 = \gamma \cdot B_{1,SL}$) is near to the frequency of this phenomenon, which affects the relaxation. However, a higher contrast between the MI area and the rest of the myocardium can be obtained by applying stronger SL pulse powers in the bigger kHz range than in lower kHz range, which will also cause more heat within the tissue (Witschey WR et al. 2010; van Oorschot JWM et al. 2015). When the amplitude of $B_{1,SL}$ reaches zero, the SL reaches zero and the **M** starts to decay as T_2^* after RF irradiation. Therefore, when $B_{1,SL}$ approaches zero, $T_{1\rho}$ relaxation approaches to T_2^* relaxation.

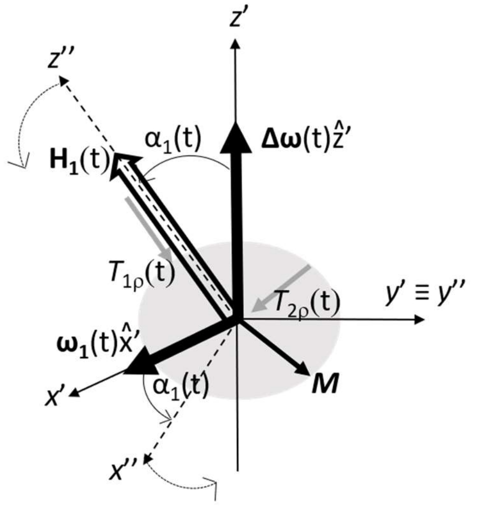

Figure 4. A schematic view of the first rotating frame during the adiabatic rotation, where the effective field $\mathbf{H}_1$(t) (rad^{-1}) and both longitudinal, $T_{1\rho}$, and transversal, $T_{2\rho}$, relaxations are shown. There are also dashed axes (*x*'', *z*'') rotating around the axis *y*' representing the second rotating frame.

2.3.1 Continuous Wave $T_{1\rho}$

The most classical measurement approach to determine $T_{1\rho}$, is the on-resonance continuous wave (CW) SL measurement (Figure 5). In CW-SL, **M** are first flipped to the x' axis followed by CW pulse along the x' axis (Figure 5). **M** is locked during the specific time period, TSL. After TSL, the reversed 90° RF pulse is used to flip the **M** back to the z-direction, which is used in fast imaging sequences. These steps can be repeated with different durations of TSL (i.e. the length of the CW pulse), which enables the quantification of $T_{1\rho}$. The $T_{1\rho}$ relaxation time measurements can be also done with off-resonance RF pulses so that the off-resonance field $\Delta B(t)$ component is also created as described in Eq (5).

The classical on-resonance CW-SL has three main difficulties, i.e. possible damage of transmit coil, high SAR and $\mathbf{B}_1$ imperfections. To overcome these difficulties, an off-resonance "rotary echo", or 180° pulse (Podkorytov IS et al. 2004), is added during the SL pulse (Witschey WR et al. 2007). Off-resonance SL increases the $\Delta\omega_0$ component, which decreases the SL RF field strength ω_1 for the same effective field ω_E and therefore reduces the SAR and ω_1 power demands on the RF coil. Additionally, a rotary echo is a way of reducing artifacts due to $\mathbf{B}_1$ inhomogeneity (Witschey WR et al. 2007). This kind of $T_{1\rho}$ measurement differs intrinsically from on-resonance $T_{1\rho}$ measurements by combining both $T_{1\rho}$ and T_1–type contrasts (Witschey WR et al. 2007).

2.3.2 Adiabatic $T_{1\rho}$ and $T_{2\rho}$

Measuring the $T_{1\rho}$ relaxation with the CW-SL method is not the only method to measure $T_{1\rho}$ relaxation. Time-varying $T_{1\rho}$ relaxation can be also measured with a train of adiabatic pulses (Michaeli S et al. 2006) (Figure 5) or with gradient modulated low-power adiabatic pulses (Andronesi OC et al. 2014) to reduce the SAR. If $\mathbf{H}_1$ is initially aligned along the **M** field, the **M** follows the $\mathbf{H}_1(t)$, i.e. **M** is locked along the $\mathbf{H}_1(t)$, during the adiabatic rotation (Figure 4). The relaxation rate during the adiabatic pulse depends on the amplitude and the direction of $\mathbf{H}_1(t)$ during the pulse and also the initial direction of **M** in relation to $\mathbf{H}_1(t)$ (Figures 4, 5). **M** remains aligned with $\mathbf{H}_1(t)$ if the adiabatic condition is fulfilled. The definition of the adiabatic condition is $|\mathbf{H}_1| >> |d\alpha_1/dt|$, where $d\alpha_1/dt$ is the angular velocity of $\mathbf{H}_1(t)$. The adiabatic condition can be described so that the amplitude of $\mathbf{H}_1(t)$ needs to be much greater than the rate at which its direction changes.

The transversal relaxation in the rotating field $T_{2\rho}$, can be measured when **M** is tilted to $x'y'$ plane with 90° RF pulse before the train of adiabatic pulses to make **M** perpendicular to the $\mathbf{H}_1$ (Figures 4, 5). The following train of adiabatic pulses then keeps **M** perpendicularly locked. Thus, the relaxation of **M** occurs in the transverse plane, with the relaxation time $T_{2\rho}$.

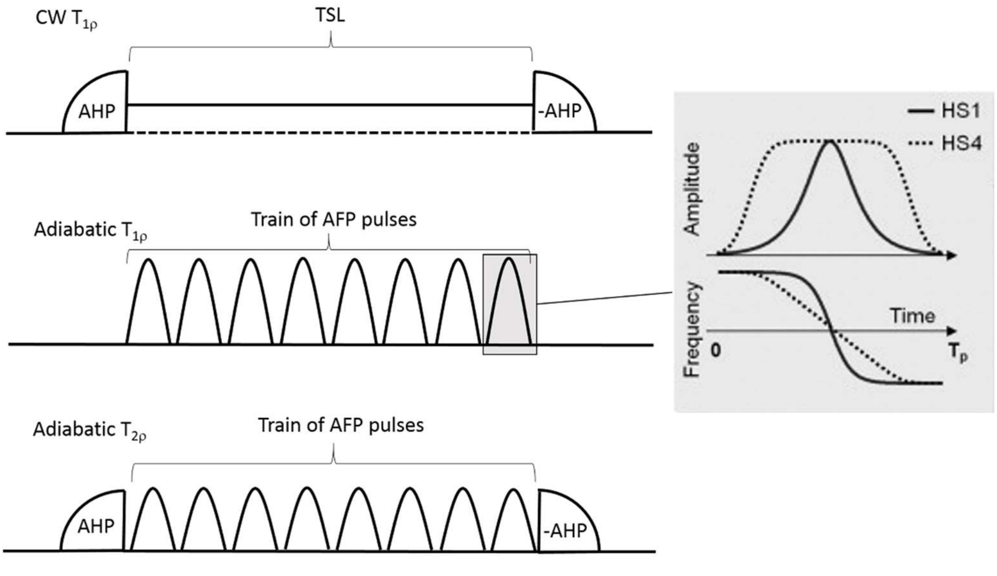

Figure 5. A schematic view of RF pulse modulations used in front of the data acquiring sequence (which is not seen in the figure) in measurements of continuous wave (CW) $T_{1\rho}$, adiabatic $T_{1\rho}$ and adiabatic $T_{2\rho}$. In adiabatic $T_{1\rho}$ and $T_{2\rho}$ pulse sequences, a train of adiabatic full passage RF pulses are used. Additionally, the amplitude and frequency modulations of HS1 and HS4 RF pulses are shown in the inset (Ellermann J et al. 2013). AHP: adiabatic half passage, AFP: adiabatic full passage.

Since adiabatic pulses are created by modulating the amplitude and the frequency of the RF pulse, the locking field varies during the SL (Michaeli S et al. 2008). Therefore, the source of relaxation differs inherently depending on the method used. Time dependency of adiabatic $T_{1\rho}$ measurement leads to the **M** to be mostly off-resonance, and therefore, adiabatic $T_{1\rho}$ is considered as off-resonance $T_{1\rho}$. Using the time dependent amplitude and frequency modulated adiabatic RF pulse, the sweep of $\mathbf{H}_1$(t) is produced. This sweep of $\mathbf{H}_1$(t) happens in relation to z'-axis (z-axis) with an angle of $\alpha_1(t)$:

$$\tan(\alpha_1(t)) = \frac{\omega_1(t)}{\Delta\omega(t)}. \qquad (14)$$

Adiabatic $T_{1\rho}$ measurements are usually done by applying an excitation pulse followed by a train of adiabatic full passage (AFP) inversion pulses and adiabatic $T_{2\rho}$ measurements are usually performed by adding adiabatic half passage (AHP), or 90° RF pulse, in front of the train of AFP inversion pulses and after the train of AFP, inversed AHP is applied (Tannús A et al. 1997) (Figure 5). Generally adiabatic pulses in $T_{1\rho}$ measurements are based on hyperbolic secant (HSn) pulses (Silver MS et al. 1984), where n (=1, 2, 3,…) is a stretching factor defining the amplitude and frequency modulations of the RF pulse (Tannús A et al. 1996; Garwood M et al. 2001) (Figure 5). Increasing n increases the flatness of pulse amplitude-modulation and the linearity in frequency sweep (Figure 5). Therefore, n has an important role in the time evolution of **M**, and it can be changed by modifying n during the pulse.

Time-bandwidth product is also an important property of the adiabatic pulses, and it is described as

$$\mathrm{R} = \frac{AT_p}{\pi}, \qquad (15)$$

where A is the amplitude of the frequency sweep in rad/s and T_p is the duration of the adiabatic pulse (Mangia S et al. 2009). Eq (15) describes that the value of R with a given specific T_p determines A. If A's unit is hertz, then R will be determined as $R=2 \cdot A \cdot T_p$ and therefore, the bandwidth (BW) of the adiabatic pulse is calculated as $BW = R/T_p$.

2.3.3 Relaxation Along a Fictitious Field, RAFF

Relaxation along a fictitious field, RAFF, is an advanced rotating frame relaxation method where the relaxation of **M** occurs along, fully or partly, a fictitious magnetic field. The existence of a fictitious field phenomena was originally detected in low frequency NMR experiments by Whitfield & Redfield (1957), and introduced into high-field MRI by Liimatainen et al. 2010. The time constant of RAFF relaxation is called T_{RAFF}. RAFF exploits sine/cosine amplitude and frequency modulated RF pulses, and acts in the subadiabatic regime, which makes T_{RAFF} different from the previously described $T_{1\rho}$ and $T_{2\rho}$. In the subadiabatic regime (Bendall MR et al. 1986), the adiabatic condition is intentionally violated, and the frequency sweep changes so fast that **M** is no longer able to follow $\mathbf{H}_1$. A fast sweep of $\mathbf{H}_1$ into $x'z'$ plane generates a fictitious magnetic field component $d\alpha_1/dt$ along the y' axis. $\mathbf{H}_1$ and $d\alpha_1/dt$ together form a final effective field, which is a geometrical sum of $\mathbf{H}_1$ and $d\alpha_1/dt$ (Eg 16). **M** keeps locked along this final effective field. When using sine/cosine pulses, a constant $d\alpha_1/dt$ component can be created (Liimatainen T et al. 2010).

When **M** is along the final effective field and the fictitious field is created in the second rotating frame with a sine/cosine pulse, the method is called RAFF2. To help to understand the concept of RAFF2 method, it is useful to move from the first to the second vector analysis (x'', y'', z'') in the rotating frame of reference. Now the rotating frame is rotating according to the sine/cosine pulse so that z'' is along $\mathbf{H}_1$ (Figure 6). When the frequency sweep in the second rotating frame is performed, the effective field in the second frame, $\mathbf{H}_2$, is the vector sum of $\mathbf{D}_1$ ($\equiv \mathbf{H}_1$) and the fictitious field component $\mathbf{C}_1 = d\alpha_1/dt$, and therefore, the amplitude of $\mathbf{H}_2$ is

$$H_2 = \sqrt{D_1^2 + C_1^2}\,, \qquad (16)$$

and the angle between $\mathbf{H}_2$ and z'' is

$$\tan(\alpha_2) = \frac{C_1(t)}{D_1(t)}. \qquad (17)$$

The amplitude of $\mathbf{H}_2$ is constant when the field components of $\mathbf{D}_1$ and $\mathbf{C}_1$ are time invariant. Modifications of orientation and amplitude of $\mathbf{H}_2$ are achievable by altering the relationship between field components $\mathbf{D}_1$ and $\mathbf{C}_1$. Eq (17) demonstrates that when sine/cosine pulses $\alpha_2 > 45°$ are used in RAFF method, the amplitude of both the $\mathbf{C}_1$ and $\mathbf{H}_2$ are larger than the amplitude of the $\mathbf{B}_1$.

The pulse duration (T_P) for RAFF2 is selected so that the frequency sweep is close to the resonance condition of the RF pulse and the RF pulse amplitude is close to its maximum value (Liimatainen T et al. 2015, inset in Figure 5). Therefore, T_P for RAFF2 is defined

$$\mathrm{T_p} = \frac{4\pi}{\sqrt{2}\,\omega_1^{\max}}. \qquad (18)$$

When the maximum power of RAFF2 pulse is defined as $\frac{\omega_1^{\max}}{2\pi} = 625\,Hz$, T_P of the pulse is calculated as 2.26 ms.

The complete RAFF2 pulse sequence to measure RAFF2 is shown in Figure 7. RAFF2 pulse consists of four segments of RF amplitude and phase modulations, which are marked as *P* (Figure 7). The first *P* rotates **M** from the *z''* axis through a revolving and evolving cone (defined by the angle of $\alpha_2 = \pi/4$ and $\mathbf{H}_2$) around the *z''* axis, to the *y''* axis. The second segment, an inversion pulse P^{-1}, brings the **M** from the *y''* axis back to the *z''* axis. The inversion pulse P^{-1} in the amplitude and phase modulation format is done by adding π to *P* phase together with reversing the time dependencies of those functions.

In living tissues, different frequency shifts, for example due to $\mathbf{B}_0$ inhomogeneities and susceptibility differences, may arise. These frequency shifts can be reversed by adding π to the phases of *P* and P^{-1}. The new pulse pair is called $P_\pi P_\pi^{-1}$, and it is added right after the first two segments containing the segments of PP^{-1}. Therefore, the whole RAFF2 pulse is described as $PP^{-1}\,P_\pi P_\pi^{-1}$ with the total length of T_P (Eq (18), Figure 7 inset). It is noteworthy that the compensation for frequency shifts in RAFF2 pulse is the same as that used in adiabatic pulse BIR-4 (Garwood M et al. 1995). Thus, RAFF2 is a rotary echo method which refocuses **M** (Solomon I. 1959). This leads RAFF2 to be less sensitive to changes in frequency-offset and also to $\mathbf{B}_0$ and $\mathbf{B}_1$ inhomogeneties.

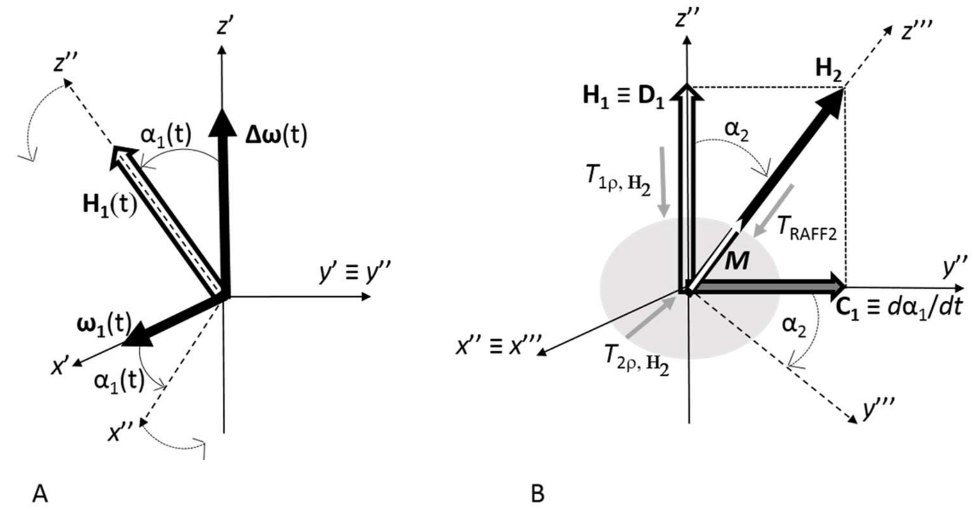

Figure 6. The coordinate system of A: 1st (*x*', *y*', *z*') and 2nd (*x*'', *y*'', *z*'') rotating frames and B: 2nd and partly 3rd (*x*''', *y*''', *z*''') rotating frames. Notice that *z*'' is parallel with **H₁** and *z*''' is along with **H₂**. Additionally, it is noteworthy that *T*RAFF2 relaxation takes place along the **H₂**.

The **M** can be determined, when the **M** is initially aligned in the *z*-direction, in the RAFF2 measurement with the following equation

$$M_{\pm} = M_{\pm 0} e^{-\frac{t}{T_{RAFF2}}} - M_{SS} e^{-\frac{t}{T_{RAFF}}}, \quad (19)$$

where $M_{\pm 0}$ is the magnetization before the RAFF2 pulses depending if there is an inversion pulse or not, and M_{SS} is the steady-state **M**. Steady-state **M** is formed in RAFF2 due to a periodical pattern of RF irradiation and therefore, M_{SS} needs to be taken into account in the fitting of the relaxation time (Liimatainen et al. 2010).

An important detail in the RAFF2 method is that the amplitude of **H₂** is at least the same as in **H₁** (Liimatainen T et al. 2011). Furthermore, the amplitude of **H₂** approaches the maximum level when α_2 approaches 90° (Liimatainen T et al. 2011). These details allow RAFF2 measurements to achieve a larger SL field without increasing the RF power.

One major advantage of rotating frame methods is that they can be tuned so that they can be sensitive to a wide range of slow molecular motions by modifying the amplitude and the orientation of the desired effective field. Molecular motions can also be studied with the Carr-Purcell-Meiboom-Gill multi-echo method, where the repetition rate of 180° pulses, i.e. the time between discrete echoes, allows one to determine the sensitivity regime of the molecular motion. The RAFF2 method combines both above methods. The tuning of the sensitivity of molecular motional regime is done by varying the magnitude and the orientation of the fictitious field component and the time between rotary echoes. It has already been shown that the

RAFF2 method is sensitive to long rotational correlation times ($\tau_c >> \omega_0^{-1}$) (Liimatainen et al. 2010). Additionally, the RAFF2 relaxation time and α_2 are dependent from each other. This is important because dipolar interactions, diffusion and proton exchange, which are the major relaxation pathways affecting the *in vivo* contrast, are all within the regime of this dependency (Liimatainen T et al. 2011).

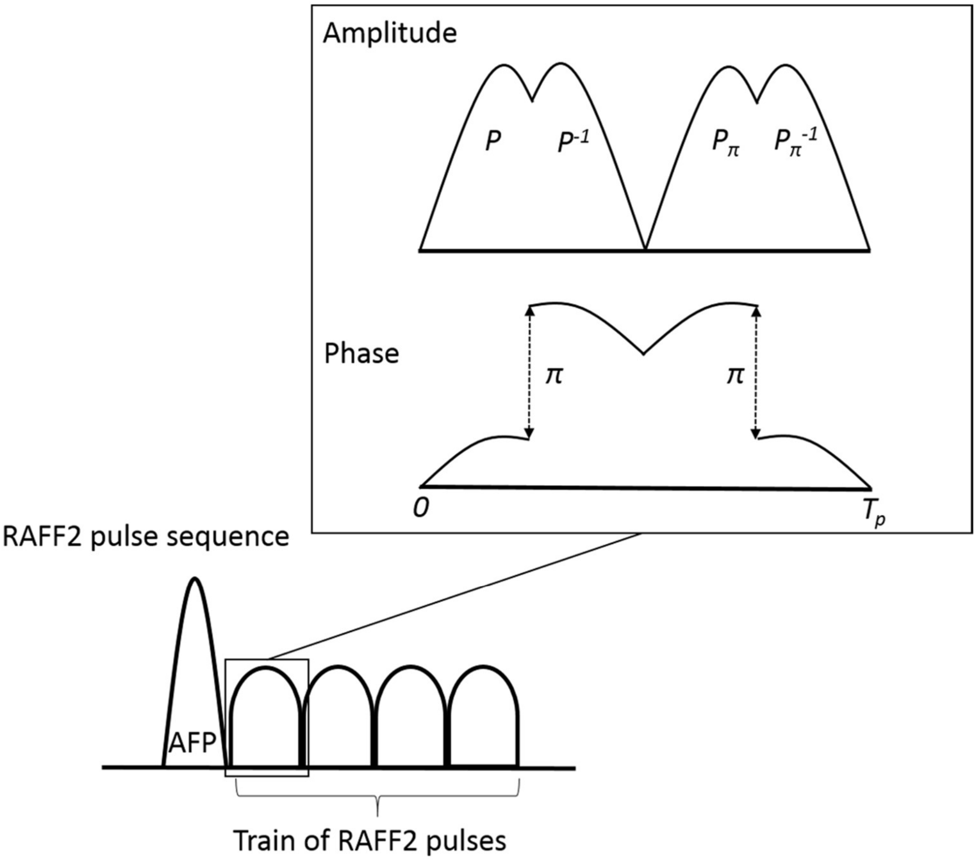

Figure 7. A schematic view of the RAFF2 pulse sequence with an AFP inversion pulse in front of RAFF2 sequence. RAFF2 can be measured also without the AFP inversion pulse. The inset describes the amplitude and phase modulations of RAFF2 pulse.

It is possible to continue this transformation of the coordinate system to higher ranks (Liimatainen T et al. 2015; Deschamps M et al. 2008). The next transformation will be performed around x'' axis and the next transformation after that around the y''' axis (Figure 8). The amplitude of the effective field in the n^{th} rotating frame is presented as:

$$H_n(t) = \sqrt{D_{n-1}^2(t) + C_{n-1}^2(t)}\ , \quad (20)$$

and the angle between $\mathbf{H}_n$ and z^n is given by

$$\tan(\alpha_n) = \frac{C_{n-1}}{D_{n-1}}. \qquad (21)$$

When the transformation ranks are added n times, the rotating frame relaxation time method is called RAFFn. As n increases in RAFFn, the tolerance for frequency alterations due to refocusing of the $\mathbf{M}$ increases (Solomon I. 1959), and therefore there are increases in the tolerance for both $\mathbf{B}_0$ and $\mathbf{B}_1$ inhomogeneties. Additionally, increasing n lowers the tilt angle in laboratory frame, which increases the bandwidth of the pulse. Furthermore, bandwidth remains relatively constant during the increase of the length of the RAFFn pulse trains (Liimatainen T et al. 2010), which is able to compensate for the inhomogeneity of $\mathbf{B}_0$. As the tilt angle of $\mathbf{M}$ decreases as n increases in the RAFFn pulses and the amplitude of $\mathbf{H}_1$ is greater than applied RF field, it is possible to produce an increased SL field with a lower RF power (Liimatainen T et al. 2010; Liimatainen T et al. 2011; Liimatainen T et al. 2015). This leads to remarkably reduced SAR values with the RAFFn method (Liimatainen T et al. 2010; Liimatainen T et al. 2011; Liimatainen T et al. 2015). Even though T_{RAFFn} differs from $T_{1\rho}$ and $T_{2\rho}$, T_{RAFFn} consists of both longitudinal $T_{1\rho}$ and transversal $T_{2\rho}$ relaxation components in that specific nth frame, which might not be the same when the frame is transferred to some other frame (Liimatainen T et al. 2010).

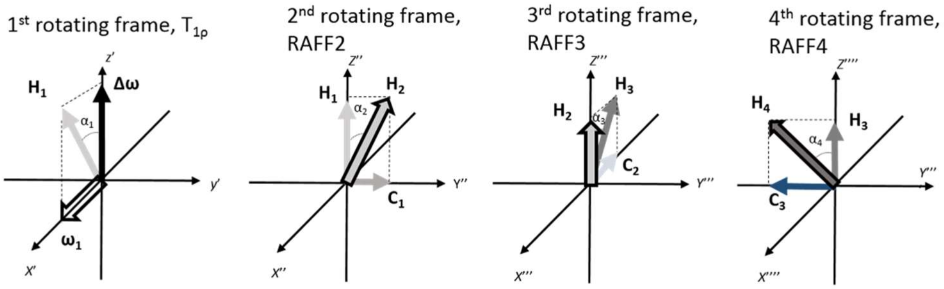

Figure 8. A schematic view from the rotating frames of rank n = 1 to 4 used to describe RAFFn.

2.4 CONTRAST-ENHANCED MRI

All of the above methods are attempting to create a contrast between adjacent tissues without any contrast agents (CA); this is known as endogenous contrast. However, obtaining good contrast in MRI images with endogenous contrast methods sometimes takes a substantial amount of time. Thus, often it is easier to obtain good contrast in MRI images with the help of CAs. An external CA can be used to enhance the contrast between adjacent tissues (McRobbie DW et al. 2007). A CA can consist of ferro- or paramagnetic ions. The CA introduces a local magnetic field inhomogeneity in the targeted tissue, which then creates a contrast between adjacent tissues (Haaf P et al. 2016). This inhomogeneity property is created with ferro- and paramagnetic ions, which are shortening the T_1 and T_2 relaxation times (McRobbie DW et al. 2007). In particular, a shortening of the T_1 relaxation time shortens the imaging time (McRobbie DW et al. 2007).

2.4.1 Gadolinium, Gd

Gadolinium (Gd) is a paramagnetic element at physiological temperatures. The atomic number of Gd is 64. For biological applications, Gd ion is attached to a chelate molecule, which reduces the toxicity of free Gd ion and makes it possible to inject Gd into a living organism. The chelate molecule can be formed so that its surface has specific features, which enable the protons of the extracellular water to interact and to move easily as close to Gd as possible, either penetrating into the chelate molecule or being attached to the outer surface of the chelate. This changes the magnetic properties and relaxation times of tissue, especially the T_1 relaxation times (Krouse W 2002; Laurent S et al. 2006). The chelate has a good mobility in the living organism, it is non-specific and it accumulates into extracellular space of the tissue (Laurent S et al. 2006). The majority of the chelates are excreted from the body in 24 h through the kidneys (Bhave G et al. 2008). If the chelate and Gd attached to it are not excreted from the body, for example due to the kidney insufficiency, the Gd ion might separate from the chelate molecule and evoke toxicity (Bhave G et al. 2008). This can be seen as allergic reactions, which in the worst case scenario, can be fatal. Gd can also accumulate in breast milk and therefore it cannot be administreted to pregnant patients (McRobbie DW et al. 2007).

2.4.2 Late Gadolinium Enhancement, LGE

The use of Gd chelate in the detection of MI with MRI is achieved by the late Gd enhancement (LGE) (Price AN et al. 2011). The use of Gd chelate in MI detection is based on a wash-in-wash-out phenomenon. In this situation, the Gd chelate is washed through the healthy tissue rather quickly but it does not pass out of the structured MI area as rapidly. Therefore, Gd chelates accumulate in the area of MI. Since this accumulation of Gd chelates takes some time, LGE is imaged at approximately 10 min after the injection of the Gd chelate (McRobbie DW et al. 2007).

Since Gd especially shortens the T_1 relaxation time, the T_1 weighted MR image is acquired 10 min after the Gd chelate injection in order to acquire hyperintensity in the MI area in the MR image. If one wishes a greater contrast between MI and healthy myocardium, then one can use the inversion recovery sequence with TI, which can be optimized to nullify the signal from normal tissue. In the resulting MR image healthy myocardium is visualized as a dark area and the MI as a bright area.

2.5 IMAGE FORMATION

The goal of imaging is to correlate the series of measured signals with different spatial locations. This is done by spatially changing the magnetic field across the sample, which is producing the measurable signal and this signal has spatially varying frequency components (Haacke EM et al. 1999). The basis of locating the spatial signal and thus for forming a MRI image lies in three orthogonal magnetic field gradients, which are known as slice selection, phase encoding and read-out gradients (Haacke EM et al. 1999). These three magnetic field gradients cause a distribution of resonance frequencies and phases over the imaged sample, which makes it possible to encode the spatial locations of the MR signal by ensuring that the Larmor frequency and the spatial location are linearly dependent on each other.

It is possible to excite the signal from the imaging slice by applying a static slice selection gradient together with finite BW RF irradiation centered at the Larmor frequency. After this excitation step, two additional orthogonal magnetic field gradients are applied to obtain a 2D raw data matrix which contains the frequency and phase information, which together is called a *k*-space (Brown et al. 2003). The phase encoding gradient is applied before the signal acquisition to spatially disperse the phases in the *k*-space. This can be detected so that each row in the 2D raw data matrix has a unique phase. The dispersion of phases depends on the duration and the strength of the applied phase encoding the magnetic field gradient. Measurement of a one line of *k*-space includes RF irradiation and the read-out gradient with a specific phase (Haacke EM et al. 1999). This event needs to be repeated at the next line and so on. Therefore, the number of phase encoding steps is the same as the number of rows in the *k*-space data matrix and therefore, this determines the time of the imaging. The read-out, or frequency encoding, gradient is applied during the signal acquisition where the spatial location is encoded in the frequency information present in the acquired signal. The read-out gradient is able to form a specific resonance frequency for each column in the 2D raw data matrix. After the signal acquisition, the acquired frequency and phase information is transferred to the spatial, or time, domain with inverse discrete Fourier Transform formula in order to form a recognizable image (Haacke EM et al 1999).

There are numerous ways to collect the *k*-space data matrix, for example Cartesian, radial or spiral acquistions. The most common approach is Cartesian *k*-space acquisition where the signal is collected line by line through the whole *k*-space. When the whole *k*-space is sampled in this way, a Cartesian grid is formed. These steps are repeated with different phase encoding gradient strengths in order to gather enough phase information. When the whole *k*-space is collected, Fourier transformation is used to transform the data from the frequency space to the spatial, or time, space. The non-Cartesian method to sample the data is done by modulating the magnetic field gradients, which allows one to collect the *k*-space points in different paths or trajectories (McRobbie et al. 2007). However, the transformation from the frequency space to the spatial, or time, space is usually more challenging than in the Cartesian approach.

The synchronization of three magnetic field gradients and RF irradiation is managed by a pulse sequence, which modulates the orientation of **M** for example by applying different weighting methods such as T_1, T_2, $T_{1\rho}$ or T_{RAFF2}. After all these modifications, the signal is acquired with specific modifications of **M**.

2.6 THE HEART

The heart is a muscle which pumps blood to provide oxygen and nutrients to the body (Taber CW et al. 2009). The mouse has a heart rate of around 400-500 beats/min, its cardiac output (CO) is about 8-12 ml/min with a stroke volume (SV) of around 20 μl/beat (Kurtz TW et al. 2014). In humans, the heart rates are much slower, 50-70 beats/min, cardiac outputs are in a range from 2.3-2.7 (L min^{-1} m^{-2}) and stroke volumes are approximately 38-49 (mL m^{-2}) (Heida M et al. 2019). The heart is located in the thoracic cavity between the left and the right lungs.

2.6.1 The anatomy of the heart

Figure 9 shows a cross-sectional image of the heart. The pericardium is the tissue around the heart, which connects the heart to its surroundings. Additionally, the space between the pericardium and the heart contains pericardial liquid, which ensures the low friction movement of the heart. The heart is formed by three specific layers, i.e. the epicardium, the myocardium and the endocardium. The epicardium is the outermost layer of the heart, and it seals the pericardial fluid within the pericardium. The myocardium is composed of elongated and webbed oriented cardiomyocytes, whose contractions never cease. The third layer, the endocardium, is located inside the heart, forming heart chambers by a seal between the cardiac muscle cells and the epicardium. (Hurst JW 2011)

The heart has four different chambers, which are the left and the right atriums and ventricles (Hurst JW 2011). During diastole, blood flows from the atriums into the ventricles (Rhoades R et al. 2003). Subsequently, during systole, blood is ejected from the ventricles to aorta and pulmonary arteries (Rhoades R et al. 2003). Since the ventricles are pushing blood outside the heart, they have more resistance to overcome and therefore, the myocardium has thicker muscle layers than the walls of the atrium (Rhoades R et al. 2003). The heart has valves between the chambers and blood vessels to ensure that blood flows in only one direction.

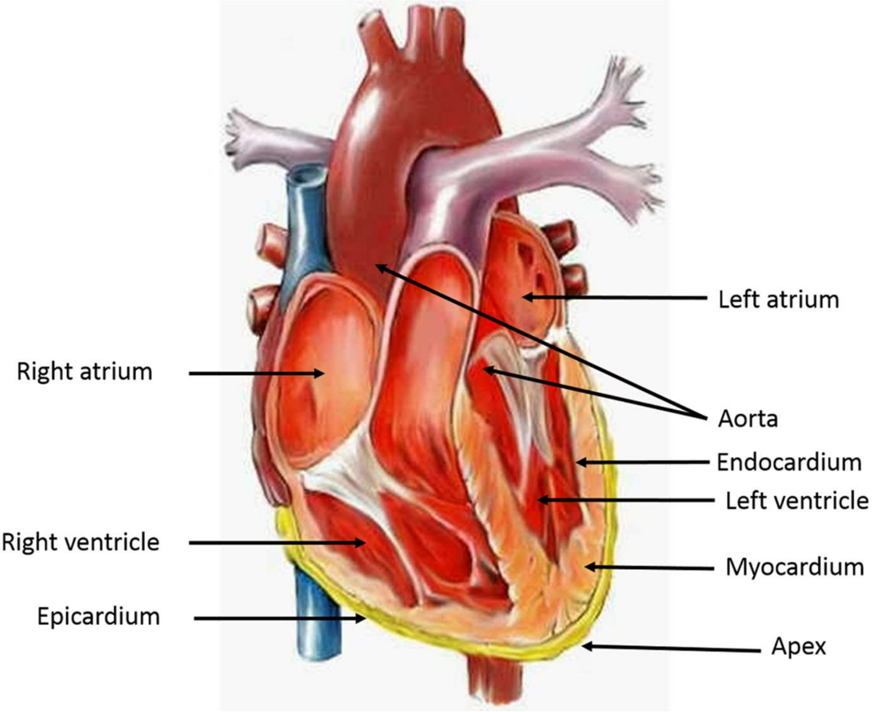

Figure 9. A cross-section image of the human heart (Modified from Hurst JW 2011).

2.6.2 The function of the heart

The function of the heart can be said to have its foundation in electrical impulses (Hurst JW 2011). The electrical impulse in humans originates from the sinoatrial node (SAN) located in the upper posterior wall of the right atrium near the entrance of the superior vena cava (Klabunde RE 2017). The shape of SAN is ellipsoidal in humans; it has a triangular planar shape in the mouse (Torrente AG et al. 2015). The cardiac conduction system includes SAN, the atrioventricular node, the bundle of His, bundle branches and Purkinje fibres (James TN et al. 1971). The conduction system is similar in humans and mice (Torrente AG et al. 2015). The electrical impulse travels through the cardiomyocytes via the electrical conduction system (Saffitz JE et al. 2016), which is formed by the sequential activation and inactivation of different current-carrying ion channels (Nerbonne JM et al. 2005). The electrical impulse travels first through the atria walls inducing the atrias to contract (Rhoades R et al. 2003). The contraction of the atria only lasts for a small period of time. The electrical impulse continues to travel via the cardiac conduction system and ultimately it induces the ventricles to contract, i.e. systole. Systole also only lasts for a short period of time and then the contraction ends (Hall JE 2011). After systole, there is a time gap, which is defined as the relaxation period when the atria become filled with blood. This relaxation period is known as diastole (Rhoades R et al. 2003). After diastole, the new electrical impulse is triggered in the SAN. The electrical impulses of the heart can be measured on the skin from the electrocardiogram (ECG) (Klabunde RE 2017).

2.6.3 Myocardial infarction, MI

MI occurs when the coronary artery is partly or fully occluded, which will lead to a prolonged interruption of perfusion in the myocardium, followed by inflammation (Hurst JW 2011; Thygesen K et al. 2012). The absence of perfusion leads to the lack of oxygen and nutrients in the myocardium and the necrotic death of cardiomyocytes (Kumar V 2015). This affects the volume of extracellular space and increases the free water content in the myocardium. This initiates a cascade of biological events, which strive to heal damaged area of the myocardium i.e. inflammatory cells start clearing the debris of dead myocytes and extracellular matrix from the infarcted area (Frangogiannis NG 2014). Eventually, this leads to the formation of fibrosis and also the formation of a collagen-based matrix, mainly type I collagen (van Oorschot JWM et al. 2015) in the damaged area (Robbers LF et al. 2012). Cross-linking of collagen increases the tensile strength of the scar and this affects the contraction of the myocardium and the propagation of electrical impulses in the heart. Additionally, the inflammation increases the formation of cardiac fibrosis and if the accumulation of the extracellular fluid is prolonged, the stiffness of the myocardium is increased, further decreasing myocardial contraction (Davis KL et al. 2000; Talman et al. 2016). All these phenomena associated with the MI can eventually lead to a pathological remodeling of the heart, i.e. hypertrophy, dilation of the chambers (Colucci WS 1997; Jarvelainen H et al. 2009) and finally heart failure (Kumar V 2015).

2.6.4 The detection of the MI area

MI can be detected and determined with various imaging modalities. MRI is beneficial in the detection of MI and section 2.10 will discuss the various uses of MRI in the detection and evaluation of MI. Hyperpolarized MRI (hMRI) is a novel MR technique for the determination of real-time metabolic activity in the area of the MI; the most common application is dynamic nuclear polarization (DNP) (Ylä-Herttuala E et al. 2019, Apps A et al. 2018, Timm KN et al. 2018). MI, the metabolism of the MI and the perfusion of the whole myocardium can also be detected with nuclear imaging based positron-emission tomography (PET) and single photon-emission computed tomography (SPECT) techniques where concentrations of radiotracers and their kinetics in the myocardium can be measured at very high sensitivities (Bengel FM et al. 2009). The MI area can be determined by x-ray based computed tomography (CT) (Vliegenthart R et al. 2012) and ultrasound (Faust O et al. 2017); however, these techniques are mainly applied for imaging the anatomy and the function of the whole heart. The disadvantages of PET, SPECT and CT are the use of ionizing radiation and the invasiveness of PET and SPECT techniques. Therefore, there is a huge advantage associated with the non-invasive and non-radiating MRI techniques in the detection of the MI area with high temporal and spatial resolution. Thus, the development of novel MRI sequences would be highly advantageous.

2.7 LYMPHATIC SYSTEM

The lymphatic network is a closed tubular system to transfer lymphatic fluid (Sherwood L 2012). The lymphatic system contains lymphatic capillaries, collecting lymphatic vessels, lymph nodes and lymphatic organs, such as tonsils and spleen. Lymphatic vessels can be found in almost all vascularized tissues, except in bone marrow (Warwick R et al. 1973). Lymphatic fluid flow starts from small lymphatic capillaries, which collect the extracellular fluid, immune cells and macromolecules from tissues (Aspelund A et al. 2016). Lymphatic capillary endothelia is formed by a single layer of endothelial cells, which are connected by collagen fibers in the extracellular matrix (Aspelund A et al. 2016). Therefore, the extracellular fluid, immune cells and macromolecules are able to enter into the small lymphatic capillaries (Warwick R et al. 1973). Lymphatic fluid flows from the lymphatic capillaries into large and tighter lymphatic vessels (Warwick R et al. 1973). The surrounding skeletal muscles help lymphatic flow to move towards the lymphatic collectors, the lymph nodes and lymphatic organs (Norma S et al. 2016). The lymphatic vessels possess valves to prevent the backflow (Warwick R et al. 1973). Lymphangiogenesis is dependent on the presence of vascular endothelial growth factor (VEGF)-C and VEGF-D protein ligands and their receptor 3 (VEGFR-3), which are cruical in allowing the growth of the lymphatic vessels (Vuorio T et al. 2017; Karkkainen MJ et al. 2004).

The lymphatic system is a key regulator of tissue fluid balance (Breslin JW 2014; Wiig H et al. 2012) as well as regulating the trafficking of immune cells (Kim KW et al. 2017) and soluble antigens (Aspelund A et al. 2016) and it is also involved in the transport of dietary fats from the intestine to the liver (Martel C et al. 2013). Since lymphatic capillaries and vessels regulate the tissue fluid balance, they have an important role in inflammatory reactions (Alitalo K 2011) associated with protection of tissues against pathogens, damaged cells and irritants (Medzhitov R 2010). Additionally, the activation of lymphangiogenesis and the remodelling of lymphatic vessels occur in inflammatory diseases (Kim H et al. 2014). The regulation and trafficking of immune cells exert a significant effect on immune defence since lymphatic vessels transport immune cells and soluble antigens from tissues to the lymphatic collectors and present antigens to immune defence cells (Randolph GJ et al. 2017). The lymphatic system has a vital role during the MI development since the lack of oxygen causes cell death, which is the stimulus for the inflammatory cells to start to remove dead cell debris through the lymphatic system and furthermore, the replacement of necrotic areas with fibrotic tissue involves the lymphatic system

(Aspelund A et al. 2016). Additionally, the cardiac lymphatic vessels undergo ectopic VEGF-C stimulation and enhance the lymphangiogenic response, which results in a transient improvement in cardiac function after MI (Klotz L et al. 2015). It is hypothesized that the disturbance of lymphatic system and thus, the fluid and nutrient balance of the tissue, can cause the apperance of edema in tissue, which subsequently affects the cardiac function (Huang LH et al. 2017; Yla-Herttuala S et al. 2007).

The lymphatic network is distributed through all layers of the myocardium and heart valves (Kholova et al. 2011; Ratajska A et al. 2014) since it is vital that there is a homeostasis in the fluid balance in the heart. It has been shown in canine models that cardiac lymph flow begins at the endocardium and passes through the whole myocardium as far as the epicardium. In the epicardium, the lymph fluid is collected into larger pre-collecting lymphatic vessels, which lead to mediastinal lymph nodes. In diastole, the increased pressure in the ventricle chambers pushes the lymphatic fluid from the endocardium to the inner myocardium. The lymphatic fluid is then moved through the lymphatic capillaries inside the myocardium to the epicardial lymphatics with the help of contracted cardiac myocytes during the systole. (Norma S et al. 2016; Huang LH et al, 2017).

2.8 VASCULAR ENDOTHELIAL GROWTH FACTORS (VEGFS)

VEGFs are a protein ligand family, which play an important role in myocardial angiogenesis (Yla-Herttuala S et al. 2017) (Figure 10). In this thesis, the main focus was placed on VEGF-D and its receptor VEGFR-3 since VEGF-C knockout mice are embryonically lethal (Janssen L et al. 2016). VEGF-D can stimulate both myocardial lymphangiogenesis and angiogenesis (Yla-Herttuala S et al. 2017, Lähteenvuo JE et al. 2009). However, when there is a malfunctioning of the VEGFR-3, both lymphangiogenesis and angiogenesis are blocked and therefore, the normal development and maintenace of lymphatic vessels no longer occurs in the myocardium although this is not vital for the survival of the mouse. Additionally, VEGF-D may be involved in mediating lymphangiogenesis during local inflammatory reactions (Bui HM et al. 2016). The putative therapeutic properties of VEGF-D have also been examined in several preclinical studies (Nurro J et al. 2016, Rissanen TT et al. 2003).

VEGFR-3 is the primary receptor for VEGF-C (Joukov V et al 1996) and VEGF-D (Achen MG et al 1998) and it is mainly located in the lymphatic endothelium (Kaipainen A et al. 1995) (Figure 10). Mutations in VEGFR-3 gene cause primary lymphedema; this is called Milroy's disease where a swelling is found in the extremities (Karkkainen MJ et al. 2000). Additionally, VEGFR-3 functions as the main receptor for lymphangiogenic signalling, and it can also control the activation of VEGFR-2 (Heinolainen K et al. 2017).

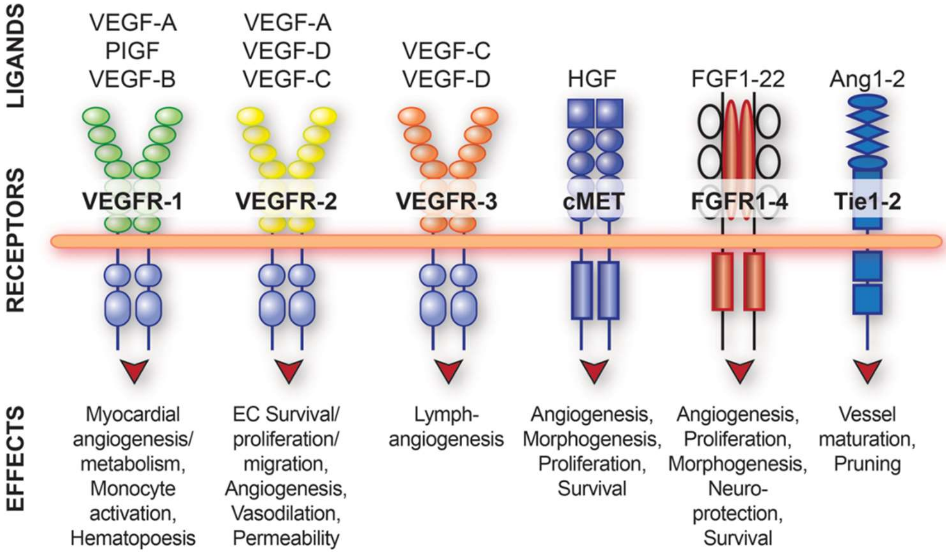

Figure 10. Different members of VEGF family, their receptors and effects in surrounding tissues (Modified from Yla-Herttuala S et al. 2017).

2.9 K14 MOUSE MODEL

The mouse model sVEGFR3 x LDLR$^{-/-}$/Apob$^{100/100}$ has the genotype of K14-sVEGFR3. This means that the mouse expresses a fusion protein consisting of the ligand-binding portion of the VEGFR-3 extracellular domain together with the fragment of a crystallizable domain of the immunoglobulin–chain under the K14-keratinocyte protein (Makinen T et al. 2001). Mice with this genotype have a phenotype of lymphedema and a lack of cutaneous lymphatic vessels (Makinen T et al 2001, Olsson AK et al. 2006). In other words, this mouse model has lymphatic vessels but the VEGFR-3 is malfunctioning and therefore, the development and the maintenance of lymphatic vessels do not function properly.

2.10 SMALL ANIMAL CARDIAC MRI

Cardiac MR imaging can be divided into functional and anatomical imaging (Biederman RW et al. 2011; Biederman RW et al. 2008). In most mouse models, both imaging modalities uses respiration and ECG triggers (Zamorano JL et al. 2015). With the help of these triggers, the MR images can be acquired every time at the right phase of the heart cycle and the movement of the heart and respiration can be neglected. However, both imaging modalities can also be performed without external triggers; this reduces the total scan time and is more comfortable for patients (Beer M et al. 2010) and animals (Bakermans AJ et al. 2015, Krämer M et al. 2015).

2.10.1 The anatomy and the function of the heart

The anatomy of the heart is assessed such that the whole heart is imaged to contain data from one heart cycle (Biederman RW et al. 2011; Biederman RW et al. 2008). The single heart cycle includes diastole-systole-diastole periods. The most common method used to image the anatomy of the heart is a stack of short-axis slices covering the whole heart (Moghari MH et al. 2018). One short-axis slice contains one heart cycle in one specific location of the heart. The information from this single short-axis slice is valuable since it can be used to determine the function of the heart and calculate the ejection fraction (EF), left ventricle (LV) volume in both end diastole volumes (EDV) and end systole volumes (ESV), stroke volume (SV) and cardiac output (CO) (Stuckey DJ et al. 2008, Stuckey DJ et al. 2008, Schneider JE et al. 2008). Imaging of the function of the heart is possible with a movie mode technique (Zamorano JL et al. 2015), which is based on the heart rate and that determines the number of T_1–weighted images, which need to be acquired (McRobbie DW et al 2007). During a single heart cycle, the whole heart cycle is imaged so that a pre-specific amount of *k*-space lines are acquired for every cine image (McRobbie DW et al 2007). After one heart cycle comes the next one and the acquiring of every *k*-space line continues where it ended in the last heart cycle (McRobbie DW et al 2007). By calculating the functional parameters from all of the short-axis slices, it is possible to determinate the functional parameters of the whole heart (Stuckey DJ et al. 2008). Additionally, one can calculate the thickness and the volume of the myocardium from the pack of short-axis slices (Leiner T et al. 2018). From the pack of MR images, the animation from the movements of the left ventricle can be created to visualize the function of the heart (Bakermans AJ et al. 2015). Imaging the whole heart with 3D acquisition is becoming more common in clinical settings (Moghari MH et al. 2018) and this has been reported to allow the reliable determination of cardiac function parameters (Liu J et al. 2017).

2.10.2 The anatomy and the function of the heart in MI

If a patient suffers an MI, this disturbs radically the function and the anatomy of the heart (Biederman RW et al. 2008). Since MI causes a malfunction in some areas of the myocardium, this can be detected as a reduced movement of the myocardium in those areas during the heart cycle. The reduced movement can be quantified as decreased EF and CO values (Protti A et al. 2012; Khan JN et al. 2017; Palazzuoli A et al. 2015, Sanches PG et al. 2017). Additionally, there is a decrease in the thickness in those areas of the myocardium (Opie LH et al. 2006) as the myocardium strives to compensate for the malfunctioning areas to maintain the same blood volume, or constant SV, being demanded by the circulation system and the body (Protti A et al. 2012). The compensation leads to an increase of ESV, EDV and LV mass, which can be accurately determined from the MR images acquired in either horizontal (Protti A et al. 2012; Galli A et al. 2016) or vertical (Tyler DJ et al. 2006) bore MR systems.

2.10.3 Gd in MI

The LGE technique is currently the gold standard to assess and locate the chronic MI area in clinics (McRobbie DW et al 2007; van Oorschot JW et al. 2015). LGE is based on a decreased tissue perfusion together with a compromised cellular integrity and extracellular edema (Geelen T et al. 2012, Strijkers GJ et al. 2007). Its wash-in-wash-out feature and its fast T_1 relaxation mean that the LGE technique has become the most widely used MR imaging modality if one wishes to distinguish an MI area from its surroundings (Krumm P et al. 2017; Ishida M et al. 2009; Geelen T et al. 2012). When Gd is bound to albumin, the alterations of the signal were associated with remodeling between acute and chronic MI (Lavin B et al. 2018). Therefore, it is impossible to determine exactly the MI borders from the normal myocardium with LGE since the border area contains mixed amounts of healthy cardimyocytes, collagen and fibrotic scar tissue, which all have different wash-in-wash-out-rates for the Gd chelate (Saeed M et al. 2017; Maestrini V et al. 2014). In some cases, it is hard to distinguish the MI area from blood but adding the T_2 preparation between the inversion pulse and the signal acquisition can resolve this problem (Fahmy AS et al. 2018). Additionally, small MI areas in the endocardium might not be detected due to the high signal of the blood pool in the LV (Saeed M et al. 2017). There are some negative features associated with the LGE technique including an inability to determine the composition of the scar tissue, highlight the extracellular water content, and a failure to determine diffuse fibrosis and global alterations in the myocardium (Saeed M et al. 2017; Maestrini V et al. 2014). Different kinds of Gd-based imaging methods, such as LGE and T_1 mapping, have been used for the detection of diffuse fibrosis in myocarditis, amyloidosis, sarcoidosis, hypertrophic cardiomyopathy due to aortic stenosis, restrictive cardiomyopathy, arrythmogenic right ventricular dysplasia and hypertension, which result in hyperintensity MR images in the damaged area of the myocardium (Saeed M et al. 2017).

Gd can also be used to determine the extracellular volume (ECV) which is possible by imaging the T_1 map before and after the Gd injection (Leiner T et al. 2018, Saeed M et al. 2017; Captur G et al. 2016). Additionally, one needs to have information about the hematocrit values in order to be able to calculate the exact ECV value (Saeed M et al. 2017; Captur G et al. 2016). The ECV fraction in the MI area is higher than in the other areas of the myocardium (Klein C et al. 2004). The ECV technique is able to determine the distribution of the cellular and extracellular matrix compartments (Mavrogeni S et al. 2017). The ECV has been associated with the extent of myocardial fibrosis and has been validated against collagen volume fraction (Messroghli DR et al. 2017; Haaf P et al. 2016) together with a better agreement to the collagen volume fraction as compared to post-contrast T_1 alone (Sibley CT et al. 2012).

2.10.4 T_1 mapping in MI

T_1 relaxation time can be calculated by acquiring multiple T_1 weighted MR images and fitting a curve to signal intensities in a pixel-by-pixel manner (Maestrini V et al. 2014) with the outcome being a T_1 map. The T_1 relaxation time map makes it possible to determine both visually and quantitatively the MI area in the whole myocardium (Garg P et al. 2018; Bulluck H et al. 2017; Sanz J et al. 2016, Coolen BF et al. 2011). This reliable tissue characterization is based on the alterations in the composition of the whole myocardium, which are caused by the changes in the intrinsic water properties inside the myocardium (e.g. edema) and the formation of collagen with an increase in the interstital space (e.g. fibrosis of infarction) (Garg P et al. 2018). These alterations within the myocardium will increase the T_1 relaxation time and generate a contrast difference within the myocardium (Garg P et al. 2018).

The T_1 relaxation time has been shown to increase during the development of the MI (Mavrogeni S et al. 2017; Garg P et al. 2018; Radenkovic D et al. 2017). However, in chronic MI, the T_1 relaxation time is not as greatly elevated as in the acute phase of the MI (Kali et al. 2014). This is due to the development of edematous and necrotic tissues, which are later replaced partly by extracellular collagen (Kali et al. 2014). Therefore, T_1 mapping is used to globally determine the pathological changes within the myocardium after MI (Mavrogeni S et al. 2017; Radenkovic D et al. 2017).

2.10.5 T_2 mapping in MI

The T_2 relaxation time mapping is beneficial for visualizing and quantifying the whole myocardium with MI (Messroghli DR et al. 2017; Garg P et al. 2018). Since the T_2 relaxation time is sensitive to alterations in the extracellular free water content, the use of T_2 mapping is appropriate for the determination of the acute MI (Messroghli DR et al. 2017; Mavrogeni S et al. 2017). The extracellular free water content increases if there is reversible tissue damage as well as in the presence of edema, which is seen as increased T_2 relaxation times and explains the use of T_2 mapping in the determination of acute MI (Mavrogeni S et al. 2017; Messroghli DR et al. 2017, Coolen BF et al. 2012). The increase in the extracellular free water content in damaged tissue is attributable to an increased movement of water molecules between the cell and the extracellular space and also due to the dissociation of water molecules from proteins (Abdel-Aty H et al. 2004). However, this is not the only reason for the increase in the amount of extracellular space since 1) the loss of sarcomere membrane integrity, 2) the presence of fibrotic tissue (Saeed M et al. 2015) and 3) the change in the scar tissue in the necrotic area are also able to influence the interstital volume (Garg P et al. 2018). For these reasons, there is a contrast formed between the damaged area and the normal area (Garg P et al. 2018). A distributed contrast-to-noise-ratio and elevated sensitiveness to motion artefacts are factors limiting the accuracy of T_2 mapping (Mavrogeni S et al. 2017; Garg P et al. 2018). Additionally, there is also bleeding in the MI area, which increases the amount of deoxy hemoglobin in the MI area and this decreases the T_2 relaxation time because deoxyhemoglobin is a paramagnetic molecule (Mavrogeni S et al. 2017; Verhaert D et al. 2011; Saeed M et al. 2017).

2.10.6 $T_{1\rho}$ mapping in MI

$T_{1\rho}$ relaxation is sensitive to slow molecular motions, which occur in the frequency range of 0.1 to 5 kHz. It is worthwhile comparing this range to the T_1 relaxation range, which is sensitive at close to the Larmor frequency (i.e. the range of 10-500 MHz). The sensitivity to slow molecular motion (i.e. the range of 0.4-2.0 kHz and τ_c is around of 10^{-1}-10^{-5} s) and macromolecular interactions explains the increased $T_{1\rho}$ relaxation time in a fibrotic and necrotic MI area, with increased extracellular space together with the higher free water content and reduced interaction between macromolecules and the water molecules (Sepponen RE et al. 1985; Kis E et al. 2018; van Oorschot JW et al. 2015). Therefore, $T_{1\rho}$ mapping is able to differentiate the MI area without the need for CAs and this has also been demonstrated in human patients (van Oorschot JW et al. 2014; Huber S et al. 2006). Additionally, an increased $T_{1\rho}$ relaxation time has been associated with a senstivity to cardiac fibrosis (van Oorschot JW et al. 2015; Sepponen RE et al. 1985; Kis E et al. 2018, Ferrari VA et al. 2011), myocardial fibrosis in ischemic cardiomyopathy patients (van Oorschot JW et al. 2017) as well as in the determination of chronic MI area in swine (Witschey WR et al. 2010; Witschey WR et al. 2012). Increased $T_{1\rho}$ relaxation time without the need for CAs has been associated also with fibrosis in cardiac hypertrophy in human patients (Wang C et al. 2015) and in mice (Khan MA et al. 2018). Furthermore, $T_{1\rho}$ is sensitive to relaxation mechanisms, such as proton exchange between water and amide, amine and hydroxyl functional groups, which may also help to characterize diseased myocardial tissue (Han Y et al. 2014; Robbers LF et al. 2012). The $T_{1\rho}$ measurement exposes tissue to heating and SAR may exceed safety limits (van Oorschot JW et al. 2015). Therefore, the power of SL RF pulse needs to be limited to lower values, which leads to a decreased contrast-to-noise ratio. However, one technique to reduce SAR and imaging time in $T_{1\rho}$ method is to utilize the $T_{1\rho}$ method with a single-shot technique together with motion correction (Berisha S et al. 2016).

2.10.7 $T_{\mathrm{RAFF}n}$ mapping in MI and other applications

The RAFFn method has been used to determine the MI area in a few studies. Since the $T_{\mathrm{RAFF}n}$ relaxation time method is an advanced version of the $T_{1\rho}$ relaxation time method, $T_{\mathrm{RAFF}n}$ relaxation time is also sensitive to slow molecular motions, which occur in the frequency range of 0.1 to 5 kHz (τ_c is around of 10^{-1}-10^{-5} s). It has been demonstrated that $T_{\mathrm{RAFF}n}$ mapping can determine accurately the MI area from its surroundings and also $T_{\mathrm{RAFF}n}$ mapping has been found to be more sensitive than $T_{1\rho}$

mapping in the detection of fibrotic area in the hypertrophic myocardium in mice (Khan MA et al. 2018). The SAR values with the same effective field ranges are significantly lower in the $T_{\mathrm{RAFF}n}$ relaxation time method as compared to the $T_{1\rho}$ relaxation time method which is an advantage of the $T_{\mathrm{RAFF}n}$ relaxation time method (Liimatainen et al. 2015). Lower SAR values become more obvious with the higher n ranks (Liimatainen et al. 2015). A recent study revealed that RAFF2 and RAFF3 methods with steady state extraction could be used as an alternative technique for ECV mapping of MI in humans (Mirmojarabian A et al. 2020).

The RAFFn method has also been used in some applications outside the heart. A high correlation was detected between T_{RAFF4} and histology together with early regenerative changes in a T_{RAFF4} relaxation time map in skeletal muscle after the induction of ischemia in mice (Laakso H et al. 2018). In brain, RAFFn has been associated with the histologically derived cell density in a rat glioma model where tha animals were being treated with gene therapy (Liimatainen et al. 2012), i.e. T_{RAFF2} relaxation was seen to be driven by the $T_{2\rho}$ relaxation pathway in a rat cerebral ischemia model together with a finding the differentiation of the RAFF2 time course from magnetic transfer (Jokivarsi et al. 2013). Furthermore, $T_{\mathrm{RAFF4,5}}$ has demonstrated a high sensitivity for detecting the myelin content and it has been used for selective myelin mapping in the rat brain (Hakkarainen H et al. 2016); RAFFn has also proven to be a valuable method to image demyelination lesions in a non-invasive manner (Lehto LJ et al. 2017). In prostate cancer mouse models T_{RAFF2} was found to outperform continuous wave $T_{1\rho}$ and T_2 in the determination of the severity of the prostate tumor (Jambor et al. 2016a; Jambor et al. 2016b) and for assessing the efficacy of chemotherapy in treating the prostate tumor (Laakso H et al. 2020). Additionally, T_{RAFF2} has been found to be sensitive to trypsin-induced bovine cartilage degeneration (Ellermann J et al. 2013) and the T_{RAFF2} correlated strongly with the biomechanical parameters associated with cartilage degeneration (Rautiainen J et al. 2015).

3 AIMS OF THE STUDY

This thesis focused on the characterization of myocardial infarction and its size using novel non-invasive magnetic resonance imaging tools without the need to administer contrast agents. Furthermore, the association between the cardiac lymphatic system and the progression of myocardial infarction was determined by exploiting novel magnetic resonance imaging tools.

The specific aims of this study were:

1. To measure $T_{1\rho}$ relaxation times in acute and chronic myocardial infarction areas in mice.
2. To characterize acute and chronic myocardial infarction with the novel T_{RAFFn} approach.
3. To examine the role of VEGFR3 and the cardiac lymphatic system in the healing process occurring after a myocardial infarction.
4. To explore relationship between lymphatic insufficiency and cardiac edema after a myocardial infarction.

4 SUBJECTS AND METHODS

Applications of MRI relaxation time methods $T_{1\rho}$ (**I**) and RAFFn were used to detect MI in wild type mice (**II**) and in mice with an insufficient lymphatic vasculature together with their littermates (**III, IV**). All animal experiments were performed in the A.I. Virtanen Institute for Molecular Sciences in Kuopio. Detailed descriptions of the methods are provided in the original publications (**I-IV**); in the following sections summarized versions of these methods are presented.

4.1 ANIMALS

All animal experiments were performed according to the guidelines approved by the University's Institutional Animal Care and Use Committee and Provincial government consistent with the EU Directive 2010/63/EU. All animal experiments were approved by the Finnish National Animal Experiment Board (ELLA) and were carried out in accordance with the Act on the Protection of Animals Used for Scientific or Educational Purposes (497/2013). All efforts were taken to minimize the number of animals used and the suffering of the animals.

4.1.1 Mice (I-IV)

Mice were chosen to be used in studies (**I-IV**) because 99 % of human genes have direct murine orthologs. Furthermore, mice have a relatively high breeding rate, which makes it possible to mimic the disease at an accelerated phase (Camacho P et al. 2016; Recchia FA et al. 2007). Additionally, mice are easy to handle and house, they have a short gestation time, they can be genetically modified to produce new transgenic strains and also they have low maintenance costs (Camacho P et al. 2016; Recchia FA et al. 2007). Normal and genetically manipulated mouse models can be established and extended into larger animal models and eventually into humans (Camacho P et al. 2016; Milani-Nejad N et al. 2014). Additionally, the A.I. Virtanen Institute for Molecular Sciences in Kuopio already had all of the mice models ready for the experiments of studies (**I-IV**).

In studies (**I**) and (**II**), 12 week old 20-25 g female C57BL mice (n=7 in (**I**), n=10 in (**II**)) were examined to determine the MI area with the various MRI contrasts described in sections 2.0.-2.10. and the contrasts were compared with histology. In study (**III**), 13-17 week old weighting 20-25 g female and male sVEGFR3 (n=22), control (n=22) and Chy (n=4) mice were used to determine the effects of the lymphatic system on the development of the MI. sVEGFR3 mice are genetically modified so that the function of VEGFR-3 is blocked and therefore lymphangiogenesis is insufficient, causing a dysfunction of lymphatic vessels (Vuorio T et al. 2014). The blockade of sVEGFR3 was examined in hyperlipidemic LDLR$^{-/-}$ x ApoB$^{100/100}$ mice, which originate from a C57BL strain. Additionally, Chy mice (Vuorio T et al. 2014) were also bred with hyperlipidemic LDLR$^{-/-}$ x ApoB$^{100/100}$ mice. LDLR$^{-/-}$ x ApoB$^{100/100}$ littermates which were bred from sVEGFR3 mice were used as controls. In study (**IV**), mice with the same genetical background (sVEGFR3 (n=11) and sVEGFR3 littermates (n=14)) of a similar age (13-17 week old) and weight (20-25 g) were used to determine the MI area with different MRI methods as well as with histology.

4.2 ANIMAL PREPARATION

4.2.1 Induction of MI (I-IV)

Mice were anesthetized with 4 % isoflurane in a 70 % N_2 and 30 % O_2 gas mixture. The anesthesia was maintained by reducing the level down to 2 % of isoflurane. The left anterior descending (LAD) coronary artery was occluded in all mice by pulling the heart out from the thorax cavity as described (Gao E et al. 2010). The LAD was ligated with a 6.0 silk suture approximately at the midway level between the base of the heart and its apex. After the LAD ligation, the heart was replaced in its original location. After the operation, analgesics were injected subcutaneously with the treatments being repeated on days 1 and 2 after the operation.

4.2.2 Preparation for MRI experiments (I-IV)

Before the MRI experiments, mice were anesthetized with 4 % isoflurane with 70 % N_2 and 30 % O_2 gas mixture and the anesthesia was maintained by reducing the isoflurane level to 1 to 1.5 %. Body temperature of the mice was maintained close to 37 °C with a warm water pad placed under the animals. ECG was measured from the forepaws of the mice using needle electrodes. Respiration was monitored by a pneumatic pillow placed under the mice. Both ECG and respiration signals were used to gate the MRI experiments.

4.3 MRI

Study (**I**) was performed with the same horizontal 9.4 T magnet as in studies (**II-IV**); however, a Varian DirectDrive™ console (Varian Inc., Palo Alto, CA) was used to control the magnet. Additionally, a half volume quadrature RF transceiver coil with a diameter of 35 mm (Virtumed, Minneapolis, MN) was uset to transmit and acquire the MR signal. Studies (**II-IV**) were performed using a horizontal 9.4 T magnet

(Varian Inc. Palo Alto, California, USA) equipped with a gradient set capable of a maximum gradient strength of 600 mT/m, which were controlled by a Bruker console (Bruker GmbH, Ettlingen, Germany). A quadrature volume transceiver with 35 mm diameter (Rapid Biomed GmbH, Ettlingen, Germany) was used to transmit and acquire the MR signal.

4.3.1 Cine imaging

Cine imaging in studies (**I-IV**) were acquired with a stack of short-axis slices covering the whole heart. Cine images were taken using fast imaging with a balanced stedy state precession (FISP) readout sequence. The cine image parameters are shown in Table 1. The number of movie frames was dependent on the mouse's heart rate and therefore, 10-12 movie frames were taken. Additionally, approximately 8-11 slices were imaged to cover LV.

4.3.2 T_2 relaxation

T_2 relaxation weightings in studies (**I-IV**) were done with a preparation module, which was placed in front of the FISP readout. The T_2 weighting module used a Hahn double echo, i.e. SE and contained an AHP excitation pulse, a delay of TE/4, one HS1 pulse, a delay of TE/2, another HS1 pulse, a delay of TE/4 and a reversed AHP pulse. Details about the parameters of T_2 weighted preparation module and the FISP readout are shown in Table 1.

4.3.3 $T_{1\rho}$ relaxation

$T_{1\rho}$ relaxation weightings in studies (**I-IV**) were also performed with a preparation module. The $T_{1\rho}$ relaxation weighting preparation module included an AHP excitation pulse, a continuous wave SL pulse and an AHP back pulse. The parameters used to achieve the $T_{1\rho}$ weighting are shown in Table 1. After the rotating frame preparation, the FISP readout was used to collect the MR signal. In study (**I**), the dispersion of $T_{1\rho}$ measeurements were done by varying the SL power in a range of 1.25-5.0 kHz with TR = 3.5 ms and TE = 1.6 ms in a TurboRARE read out.

4.3.4 RAFFn relaxation

RAFFn (n=2,4) relaxation weightings in studies (**II-IV**) were also done with a preparation module. The rotating frame preparation module consisted either RAFF2 or RAFF4 pulses with a varying number of pulses in pulse trains (Table 1). After the rotating frame preparation, the FISP readout was used to acquire the MR signal.

4.3.5 B_1 field

To map the homogeneity of B_1 magnetic field in studies (**II-IV**), a square RF pulse with a power of 625 Hz and a varying pulse duration were applied. The details about the parameters of B_1 measurement are shown in Table 1. After the block pulse, the FISP readout was used to collect the MR signal.

4.3.6 LGE

LGE measurements were done at the last time point and it was based on inversion preparation followed by the FISP readout in study (**II**). The parameters used for the LGE measurements are shown in Table 1. LGE measurements required a tail vein injection of gadobutrol (Gadovist, Bayern Oy, Turku, Finland) with an intravenous injection volume of 5 ml/kg per mouse.

Table 1. MRI parameters used in studies (**I-IV**).

MRI method	**Description**
Cine	field-of-view (FOV) = 4 x 4 cm^2 (3 x 3 cm^2 in study (**I**)), slice thickness (thk) = 1 mm (1.2 mm in study (**I**)), matrix size = 192 x 192 (128 x 128 in study (**I**)), TE = 1.9 ms (2.7 ms in study (**I**)), TR = 8.0 ms (10.0 ms in study (**I**)) and flip angle (fa) = 10°
T_2	Excitation AHP: power 1250 Hz, duration 3.0 ms, HS1: power 1250 Hz, duration 4.5 ms, reversed AHP: power 1250 Hz, duration 3.0 ms, TEs = 0.05, 2.3, 4.5, 14.0 ms
$T_{1\rho}$	Excitation AHP: power 1250 Hz, duration 2.0 ms (6.0 ms in study (**I**)), continuous wave SL with TSL = 0.4, 9.4, 27.4, 45.4 ms (0, 18, 26, 54 ms in study (**I**)), AHP back pulse: power 1250 Hz, duration 2.0 ms (6.0 ms in study (**I**))
T_{RAFFn}, n=2,4 (**II-IV**)	RF power for RAFF2: 1250 Hz and for RAFF4: 648 Hz, Pulse train lengths: 0, 9.1, 18.2, 36.2 ms
FLASH readout (**I**)	FOV = 3 x 3 cm^2, thk = 1.5 mm, matrix size = 128 x 128, TE = 8.0 ms, TR = 2.0 ms, fa = 90°
TurboRARE readout (**I**)	FOV = 3 x 3 cm^2, thk = 1.5 mm, matrix size = 128 x 128, TE = 1.6 ms, TR = 3.5 ms, fa = 15°
FISP readout (**II-IV**)	FOV = 4 x 4 cm^2, thk = 1 mm, matrix size = 256 x 256, TE = 1.9 ms, TR = 14.9 ms, fa = 90°
B_1	Power: 625 Hz, pulse durations: 0, 0.25, 0.5, 0.75, 1.0, 1.25, 1.5, 1.75 ms; FISP: FOV = 4 x 4 cm^2, thk = 1 mm, matrix 128 x 128, TE = 1.9 ms, TR = 14.9 ms, fa = 90°
LGE	TI: 300 ms, FOV = 4 x 4 cm^2, thk = 1 mm, matrix size 256 x 192, TE = 2.0 ms, TR = 5.6 ms, scan TR = 3000.0 ms, fa = 90°

4.4 HISTOLOGY

Histology is used in the animal studies not only to acquire cellular level information of the studied tissues but it also allows a confirmation of the MRI findings. Histology is an invasive technique and it is done after the sacrifice of the animals i.e. heart samples were collected and prepared for staining (Huusko J et al. 2010). In studies (**I-IV**), histological information were compared with MRI results to obtain cellular level explanations for the differencies or alterations detected by MRI.

In study (**I**), mice were sacrificed on day 20 after the MI. In studies (**II** and **IV**), mice were sacrificed on day 21 after the MI; in study (**III**), mice were sacrificed either on day 4, on day 8 and on day 42 after the MI. Immediately after sacrifice, the hearts were perfused through the LV with phosphate buffered saline, and then the samples were immersion-fixed with 4 % paraformaldehyde with sucrose in phosphate buffered solution for 4 h (Huusko J et al. 2010) after which the hearts were placed in 15 % sucrose.

4.5 ULTRASOUND

In study (**III**), transthoracic echocardiography was performed on day 7 or on day 35 after the MI (VEVO 2100, VisualSonics, Toronto, Canada). High-frequency and high-resolution images were collected during the time when the mice were anesthetized with isoflurane. The imaging system included a transducer probe operating at 18-38 MHz (MS-400, VisualSonics). During the imaging, the ECG signal was acquired to trigger imaging similarly as in MRI and the ECG data were exported from Vevo software (VisualSonics) and analyzed with rodent ECG imaging software (Kubios HRV 2.0, Kuopio Finland).

4.6 DATA-ANALYSIS

4.6.1 ROI analysis

Region-of-interests (ROIs) were manually traced with visual delineations of different areas of the heart, ROIs were drawn using Aedes software package in Matlab platform (Mathworks Inc. Natick, Massachusetts, USA).

4.6.2 Cardiac function

In the determination of the cardiac functions, EDV and ESV ROIs were drawn based on the endocardial border in cine images in studies (**I**-**IV**). The SV was calcuated with a function of $SV=EDV–ESV$. Additionally, CO was calculated as $CO=SV\cdot HR$, where HR is the heart rate of the mouse. The most common parameter to describe cardiac function is EF, which is calculated as $EF=(SV/EDV)\cdot 100\%$. The EF describes how well the LV pumps the blood into the aorta. In study (**I**), LV was also calculated during the systolic phase. In study (**IV**), LV mass was also determined by ROI analysis so that ROI was drawn in the LV area during the diastole phase in every cine image at all time points.

4.6.3 Relaxation time and B_1 maps

All relaxation time data and B_1 were calculated from signal intensities of weighted MR images on a pixel-by-pixel basis using Aedes on a Matlab platform. The signal intensity values from a specific pixel can be connected by fitting a function within the MR images. When the pixel-by-pixel analysis is done, the relaxation time map can be formed.

In study (**I**), $T_{1\rho}$ relaxation time maps were fitted using single monoexponential decay function. In studies (**II**-**IV**), T_{RAFF2} and T_{RAFF4} relaxation time maps were fitted by using a single mono-exponential decay function without taking into account the steady state formation (Eq 19). Additionally, $T_{1\rho}$ and T_2 relaxation time maps were fitted using linear function for linearized data. As B_1 measurements were done by increasing hard pulse lengths, a fit of single cosine function was used to obtain a B_1 map (Vaughan JT et al. 2002) in studies (**II**- **IV**).

4.6.4 Myocardial infarct and remote area determination

In studies (**I**-**IV**), MI and remote areas were determined from the relaxation time maps and cine images using ROIs. The MI area was detected as an increased relaxation time in every relaxation time map and also in the cine images as a thinner myocardium, which was not moving during the heart cycle. The MI area in LGE image was visible as a bright area inside the myocardium (study (**II**)). In all cases, the remote area was determined from the area of normally functioning myocardium.

4.6.5 Relative relaxation time difference, RRTD

In studies (**II, IV**), the RRTD was determined between the relaxation times from the MI area and from the remote area. An RRTD analysis was done with a midline length-based method with a function of $((T_{(infarct)}-T_{(remote)})/T_{(infarct)})\cdot 100\%$, where T denotes either T_{RAFF2}, T_{RAFF4}, $T_{1\rho}$ or T_2 relaxation times.

4.6.6 Infarct percentage

In studies (**I**-**IV**), the MI size from the whole myocardium was determined in relation to the MI size of the whole myocardium. Infarct percentage analysis was done with a midline length-based method with a function of $(L_{(infarct)}/L_{(circumference)})\cdot 100\%$, where L denotes a measured length from either T_{RAFF2}, T_{RAFF4}, $T_{1\rho}$, T_2, LGE (**II**) or histology stained sections.

4.6.7 Amount of overestimation, AOE

Since the LGE measurement in the determination of the MI area is currently the gold standard, an amount of overestimation (AOE) analysis reflects the relation between the LGE determined MI area and the MI area determined by relaxation time maps. AOE values can be calculated based on the midline length with a relation function of $((L_{(infarct)}-LGE_{(infarct)})/L_{(infarct)})\cdot 100\%$, where L denotes either T_{RAFF2}, T_{RAFF4}, $T_{1\rho}$ or T_2 relaxation times. AOE values were determined in study (**II**).

4.6.8 Area of difference, AOD

When the LGE measurement is not used, the AOE analysis cannot be performed. A new approach to compensate for this short-coming is to estimate the area of difference (AOD). The idea behind AOD is the same as in the AOE but the relationship is formed between T_2 defined MI area and the rotating frame relaxation defined MI area. AOD is calculated based on the midline length with a relation function of $((A_{T2(infarct)}-A_{(infarct)})/A_{(infarct)})\cdot 100\%$, where $A_{T2(infarct)}$ denotes the length of the MI size in T_2 relaxation time map and $A_{(infarct)}$ denotes the infarct size in either T_{RAFF2}, T_{RAFF4} or $T_{1\rho}$ relaxation time maps. AOD values were determined in the study (**IV**).

4.6.9 Molecular and cell culture

Molecular biology and cell culture were determined in study (**III**). Initially, sVEGFR3 and Chy mice were genotyped with polymerase chain reaction (PCR) using DNA extracted from ear punctures. Then gene expression analysis was done by extracting RNA from snap-frozen tissue samples using RNA extraction kits (Qiagen). Furthermore, a quantitative real-time PCR was done for individual genes. Additionally, Westerm blot was performed to analyze specific protein in plasma or tissue samples.

4.6.10 Statistics

In studies (**I**-**IV**), two-way ANOVA with Bonferroni post-hoc test was applied to compare the spatial and temporal alterations between the MI and remote areas. Analyses were done with GraphPad Prism software (GraphPad Software, La Jolla, CA, USA). In study (**III**), two-tailed unpaired t-test and one-way ANOVA with Bonferroni correction were used.

5 RESULTS

The characterization of MI and its size using non-invasive magnetic resonance imaging tools without the need for administration of contrast agents was the main aim of this thesis. Additionally, the association between the cardiac lymphatic system and the progression of myocardial infarction as assessed by rotating frame and conventional magnetic resonance imaging tools was a further aim of this thesis.

5.1 CARDIAC FUNCTION (I-IV)

Cardiac functional parameters revealed the development of MI as expected. The results of EF and LV results are found in Table 2 and in Figure 11. Other cardiac function parameters, such as SV and CO remained stable at all time points (Table 1 in (**I**), Table 2 in (**II**), Figure 11), and therefore, they are not included in Table 2. EF decreased as a function of time (Table 2), which was due to the development of MI and the stiffness of the myocardium and this caused a progressive reduction in the pumping efficacy of the MI hearts. Additionally, LV mass increased after the MI (Table 2). In study (**I**), the thickness of end systolic LV wall was also measured. There was a 60 % decrease in the LV wall thickness in the MI area and this decrease remained throughout the study (Table 1 in (**I**)).

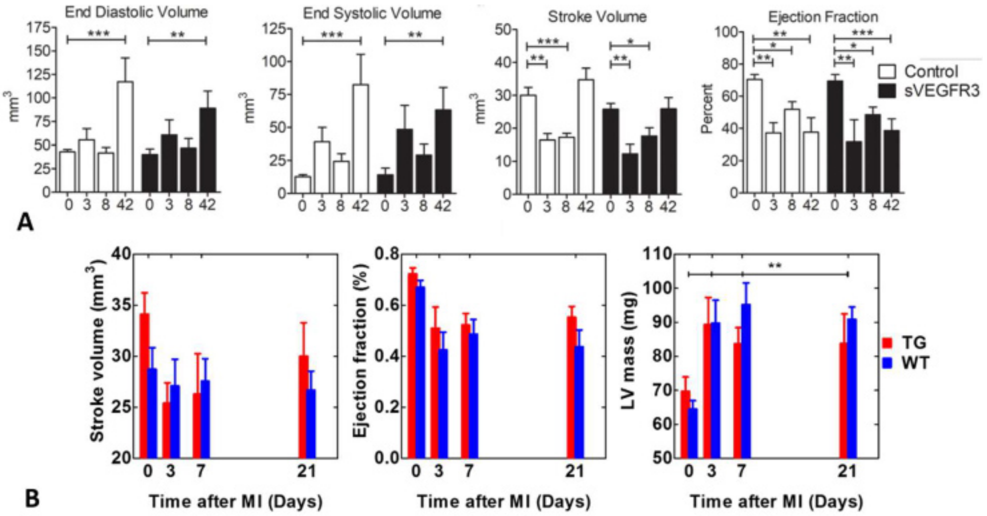

Figure 11. Cardiac function parameters A: from study (**III**) and B: from study (**IV**).

Table 2. Cardiac functional parameters as a function of time in studies (**I-IV**). Statistical analyses were done with either one-way (^^P<0.01) or two-way ANOVA with Bonferroni's post-hoc test (*P<0.05, **P<0.01, ***P<0.001) to test the significance between day -1/0 and other time points.

Functional parameter	**Day -1/0**	**Day 1**	**Day 3**	**Day 7**	**Day 8**	**Day 20**	**Day 21**	**Day 42**
EF (%) (**I**)	68.2 ± 8.9	50.0 ± 4.9	55.3 ± 6.0	50.0 ± 7.4		55.5 ± 5.1		
EF (%) (**II**)		55.0 ± 12.0	56.0 ± 9.0	46.0 ± 9.0			35.0 ± 4.0^^	
EF (%) (**III**)	69.4 ± 5.0		31.7 ± 15.0**		48.8 ± 5.0*			38.6 ± 10.0***
Littermate EF (%) (**III**)	70.4 ± 4.0		37.2 ± 7.0**		51.8 ± 5.0*			37.6 ± 7.0**
EF (%) (**IV**)	72.3 ± 2.3		51.0 ± 8.3	52.2 ± 4.6			55.2 ± 4.3	
Littermate EF (%) (**IV**)	66.9 ± 2.8		42.5 ± 6.8	48.6 ± 5.8			43.7 ± 6.6	
LV (mg) mass diastole (**I**)	71.8 ± 6.1	99.6 ± 12.1	95.9 ± 9.7	82.2 ± 7.2		84.8 ± 2.9		
LV (mg) mass systole (**I**)	77.2 ± 8.6	94.0 ± 9.4	100.6 ± 12.0	88.9 ±6.8		98.29 ± 5.4		
LV (mg) mass (**IV**)	69.7 ± 4.2		89.3 ± 8.0**	83.7 ± 4.7**			83.8 ± 8.6**	
Littermate LV (mg) mass (**IV**)	64.4 ± 2.5		89.7 ± 6.7**	95.2 ± 6.4**			90.8 ± 3.7**	

5.2 QUANTIFICATION OF MYOCARDIAL INFARCTION (I-IV)

5.2.1 Relaxation times at the MI area

The results of different relaxation time constants used in studies (**I-IV**) are found in Table 3. In study (**I**), the dispersion of $T_{1\rho}$ relaxation time was measured at multiple time points. The significant increase in $T_{1\rho}$ relaxation time was found at 7 days after the MI and it remained elevated at the last time point in comparison to the remote areas (Figure 12A). The dispersion of $T_{1\rho}$ relaxation time contained four different SL fields. An improved contrast was detected with increasing SL fields between myocardium and arterial blood pool of left ventricle (Figure 12B).

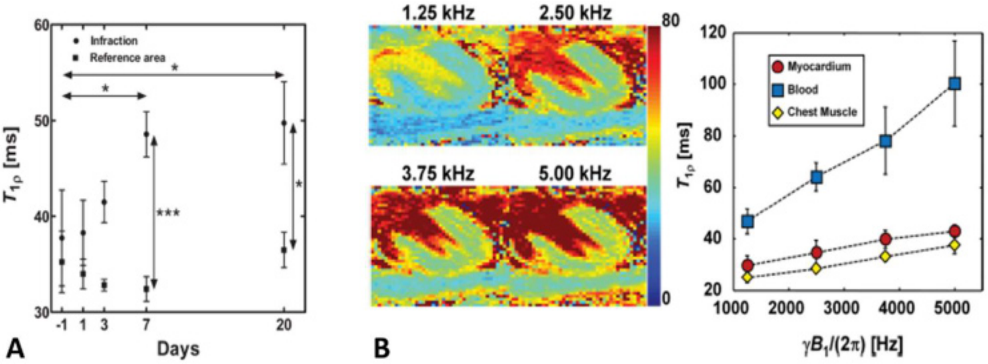

Figure 12. $T_{1\rho}$ relaxation time evolution in A: different time points B: different SL fields in study (**I**). Statistical analyses were done with two-way ANOVA with Bonferroni's post-hoc test (*P<0.05, **P<0.01, ***P<0.001) to test the significance between day -1 and other time points and also between the MI and remote areas.

In study (**II**), all relaxation time constants, T_{RAFF2}, T_{RAFF2}, $T_{1\rho}$ (with different SL powers (1250, 625, 400 Hz)) and T_2, increased in the MI area after LAD ligation (Figure 13). The T_{RAFF2} relaxation time increased significantly up to 7 days after the MI and it remained elevated after the MI as compared to remote areas measured as RRTD values with T_{RAFF2} in a range of 0.62-0.73 and with T_{RAFF2} in a range of 1.22-1.39 in study (**II**) (Figure 13B, Table 1 in study (**II**)). Additionally, T_{RAFF4} relaxation time was elevated in the MI area at all time points in study (**II**) (Figure 13B). All the $T_{1\rho}$ and T_2 relaxation times were significantly elevated at the MI area as compared to remote areas in study (**II**) (Figure 13B). All of these changes can be also seen in RRTD values (Table 1 in study (**II**)).

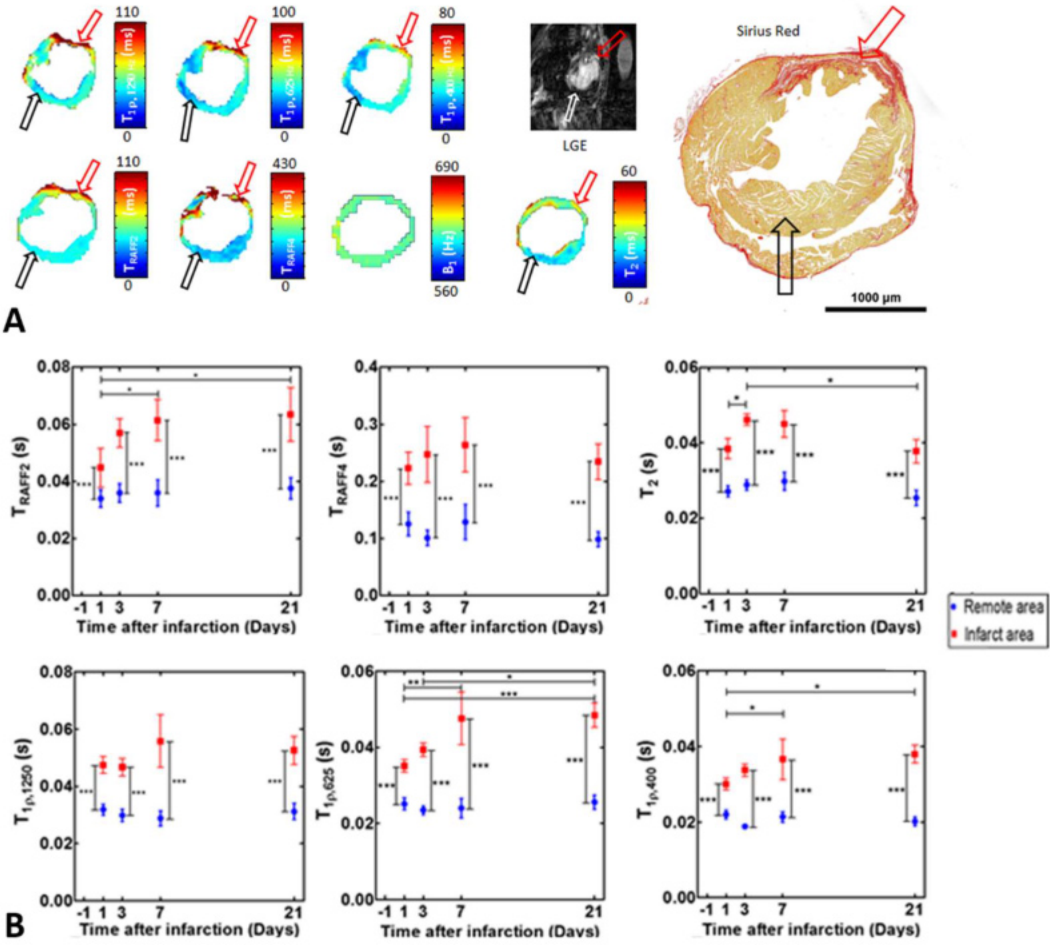

Figure 13. Relaxation times measured in study (**II**) are shown A: visually at the last time point and B: as a function of time. Statistical analyses were done with two-way ANOVA with Bonferroni's post-hoc test (*P<0.05, **P<0.01, ***P<0.001) to test the significance between day -1 and other time points and also between the MI and remote areas.

In study (**III**), T_2 relaxation time was measured in multiple time points but T_{RAFF2}, T_{RAFF4} and $T_{1\rho}$ relaxation times were measured at one time point (7 days after the MI). The T_2 relaxation time was found to increase in the area of MI at 8 and 42 days after MI in both lymphatic insufficient and littermate mice (Figure 14). All rotating frame relaxation time methods were able to determine the MI and remote areas from each other in both mouse groups at 7 days after the MI (Figure 14). One interesting finding was that the T_{RAFF4} relaxation time was significantly higher in the MI area in lymphatic insufficient mice as compared to the MI area in their littermates (Figure 14), evidence of changes in the composition of the MI area in lymphatic insufficient mice after the MI. Measured relaxation time constants of T_{RAFF2}, T_{RAFF4}, $T_{1\rho}$ and T_2 increased significantly in the MI area as a function of time in comparison to the remote area in both lymphatic insufficient and their littermate mice (Figure 14). Additionally, these changes were seen in RRTD values.

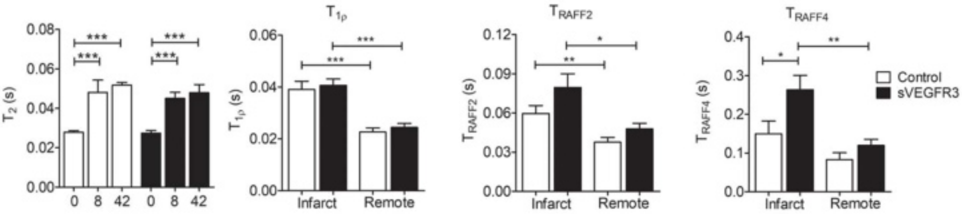

Figure 14. Relaxation times measured in study (**III**). Statistical analyses were done with two-way ANOVA with Bonferroni's post-hoc test (*P<0.05, **P<0.01, ***P<0.001) to test the significance between day 0 and other time points and also between the MI and remote areas.

In study (**IV**), the MI area was visible at the last time point at all relaxation time maps as increased relaxation times (*T*T_{RAFF2}, T_{RAFF4}, $T_{1\rho}$ and T_2), as akinetic area in cine images and fibrotic area in Sirius Red stained histology section (Figure 15A). Additionally, all relaxation times increased significantly in the MI area as compared to remote areas (Figure 15B).

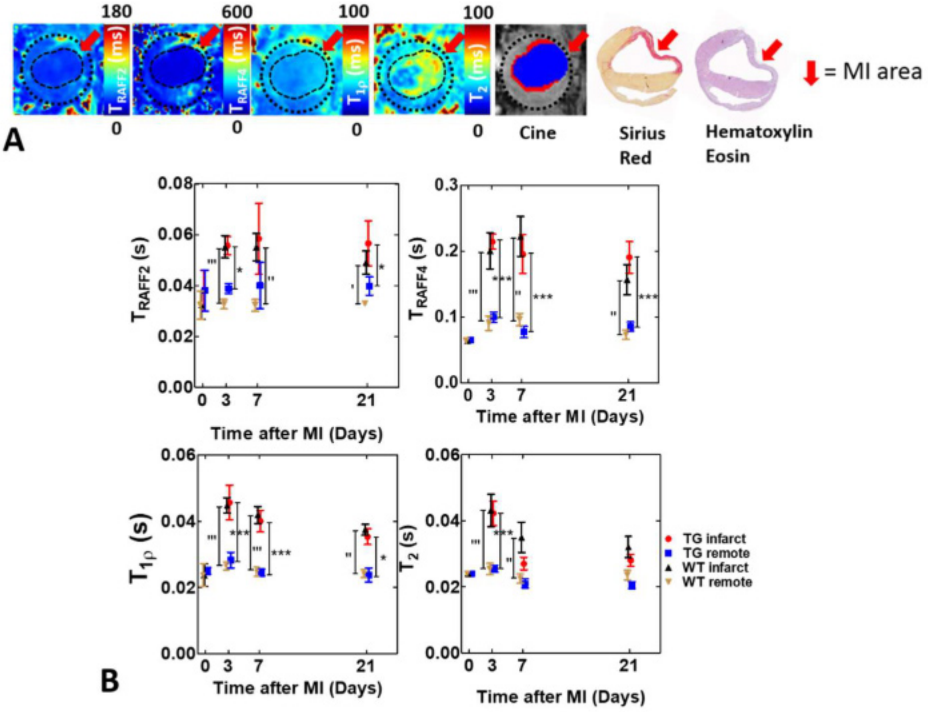

Figure 14. Relaxation time measured in study (**IV**). Statistical analyses were done with two-way ANOVA with Bonferroni's post-hoc test (*P<0.05, **P<0.01, ***P<0.001) to test the significance between day 0 and other time points and also between the MI and remote areas.

Table 3. Results of different relaxation time constants at different time points after the MI in studies (**I**-**IV**). For $T_{1\rho}$, only SL field of 625 Hz (studies (**II**-**IV**)) and 1250 Hz (study (**I**)) are presented in the table. Statistical analyses were done two-way ANOVA with Bonferroni's post-hoc test (*P<0.05, **P<0.01, ***P<0.001) to test the significance between day -1/0 and other time points.

Relaxation time method	**Day-1/0**	**Day 1**	**Day 3**	**Day 7**	**Day 8**	**Day 20**	**Day 21**	**Day 42**
T_{RAFF2} (ms) (**II**)		48 ± 5	57 ± 5	61 ± 7*			63 ± 9*	
T_{RAFF2} (ms) (**III**)				80 ± 11				
Littermate T_{RAFF2} (ms) (**III**)				64 ± 6				
T_{RAFF2} (ms) (**IV**)	38 ± 8		56 ± 4	59 ± 14			57 ± 9	
Littermate T_{RAFF2} (ms) (**IV**)	32 ± 6		55 ± 4	55 ± 5			49 ± 5	
T_{RAFF4} (ms) (**II**)		223 ± 28	247 ± 49	264 ± 48			234 ± 32	
T_{RAFF4} (ms) (**III**)				263 ± 37				
Littermate T_{RAFF4} (ms) (**III**)				149 ± 33				
T_{RAFF4} (ms) (**IV**)	65 ± 2		215 ± 12	196 ± 29			191 ± 24	
Littermate T_{RAFF4} (ms) (**IV**)	64 ± 4		201 ± 27	223 ± 30			171 ± 22	
$T_{1\rho}$ (ms) (**I**)	38 ± 4	39 ± 3	41 ± 2	49 ± 2*		50 ± 4*		
$T_{1\rho}$ (ms) (**II**)		35 ± 2	39 ± 2	48 ± 7**			48 ± 3***	
$T_{1\rho}$ (ms) (**III**)				41 ± 3				
Littermate $T_{1\rho}$ (ms) (**III**)				39 ± 3				
$T_{1\rho}$ (ms) (**IV**)	25 ± 1		46 ± 5	40 ± 3			35 ± 2	

Relaxation time method	**Day-1/0**	**Day 1**	**Day 3**	**Day 7**	**Day 8**	**Day 20**	**Day 21**	**Day 42**
Littermate $T_{1\rho}$ (ms) (**IV**)	24 ± 3		45 ± 2	42 ± 3			37 ± 2	
T_2 (ms) (**II**)		38 ± 3	46 ± 2*	45 ± 4			38 ± 3	
T_2 (ms) (**III**)	27 ± 1				46 ± 3			48 ± 4
Littermate T_2 (ms) (**III**)	28 ± 1				48 ± 6			52 ± 1
T_2 (ms) (**IV**)	24 ± 0		42 ± 4	27 ± 2			28 ± 2	
Littermate T_2 (ms) (**IV**)	24 ± 0		43 ± 5	35 ± 5			32 ± 3	

5.2.2 MI sizes in relaxation time maps

In study **II**, the infarct sizes were calculated based on infarct percentage and AOE analysis techniques (Figure 15A). Infarct percentage values were similar in rotating frame relaxation time maps and the highest infarct percentage values at earlier time points was measured in the T_2 relaxation time map, which is evidence of the increased water content in the area of MI and its surroundings (Figure 15A). The lowest AOE value was found with T_{RAFF2} indicating that the MI size was determined based on T_{RAFF2} is similar to the MI size estimated based on LGE (Figure 15A). MI sizes determined by T_{RAFF2}, T_{RAFF4}, $T_{1\rho}$ and LGE correlated well with the MI size determined from Sirius Red-stained sections (Figure 15B).

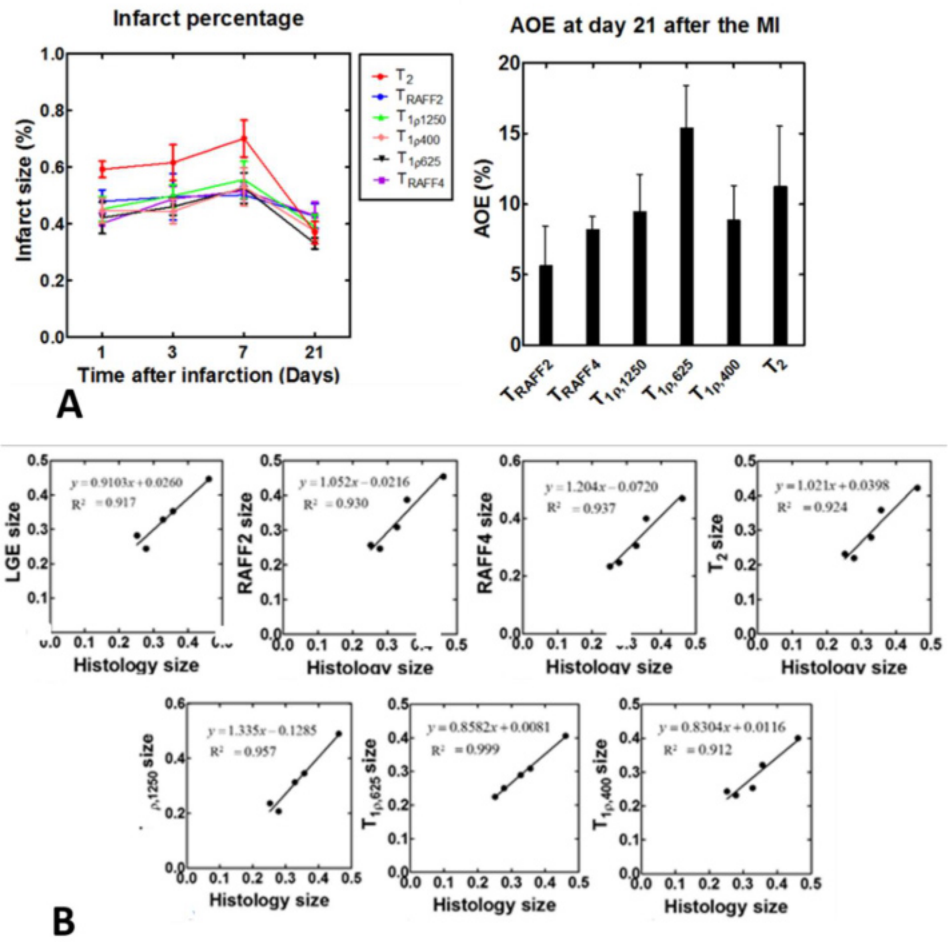

Figure 15. A: Infarct percentages and AOE are shown from study (**II**). B: Linear correlations to histology between the arc of infarct and the circumferences of the whole myocardium determined by the MRI methods in study (**II**). Additionally, the formulas of linear relationships are shown.

In study (**IV**), MI sizes were calculated based on infarct percentage and AOD analysis techniques (Figure 16). MI sizes in all relaxation time maps decreased as a function of time (Figure 16A). The MI size determined in T_{RAFF4} relaxation time map correlated best with Sirius Red stained histology (R^2:0.81, $P<0.05$) in the insufficient lymphatic myocardium. The T_{RAFF2} relaxation time map correlated best with the Sirius Red stained histology (R^2:0.67, $P=0.09$) determined MI area in their littermates' myocardium. Additionally, AOD values measured with T_2 and T_{RAFF2} were significantly larger in the insufficient lymphatic myocardium as compared to their littermates' myocardium except at the earlier time points (Figure 16B). The difference between mouse groups increased between T_2, T_{RAFF4} and $T_{1\rho}$ relaxation time maps as a function of time (Figure 16B). Furthermore, the interaction between the mouse groups differed significantly (Figure 16B).

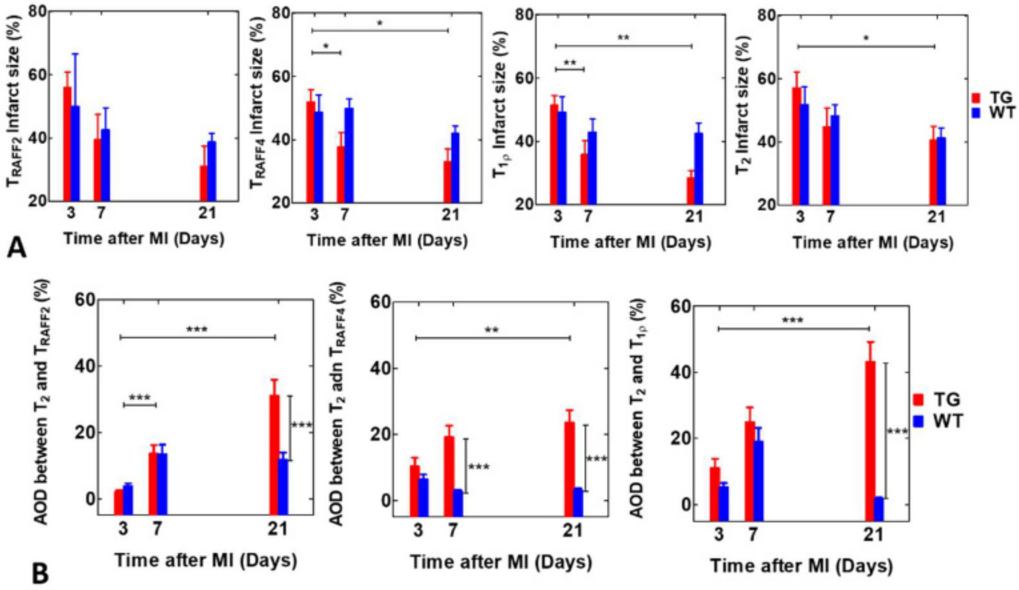

Figure 16. A: Infarct sizes based on increased relaxation time in different relaxation time maps are shown (**IV**). B: AOD values between T_2 and rotating relaxation time maps are shown (**IV**). Statistical analyses were done with two-way ANOVA with Bonferroni's post-hoc test (*P<0.05, **P<0.01, ***P<0.001) to test the significance between day 3 and other time points and also between the MI and remote areas.

5.2.3 Comparison of infarct size by MRI and histopathology

Relaxation time measurements were compared to other methods. In study (**I**), Masson's trichrome staining was used to distinguish the fibrotic area of the infarcted heart. In study (**II**), LGE and Sirius Red stained histology confirmed the good correlation with MRI findings (Figure 15B). An infarct percentage analysis was done between LGE and Sirius Red stained histology. In study (**IV**), Sirius Red and hematoxylin eosin stained histology sections were used to confirm the MRI findings. The best correlation with both histology stainings was obtained with RAFFn (T_{RAFF4} (R^2:0.81, P<0.05) in TG group and T_{RAFF2} (R^2:0.67, P=0.09) in WT group). The MI sizes were estimated with infarct percentage analysis.

5.2.4 MI tissue characterization in lymphatic vessel insufficient mice (III)

Several histology techniques were used to determine the MI area in study (**III**). Lymphatic insufficient mice had larger MI sizes as determined by the Masson's trichrome staining as compared to their littermates. This might explain the significantly higher mortality of mice with an insufficient lymphatic system as compared to littermate controls (25 % vs. 4 %, respectively, $P < 0.05$) (Figure 1 in (**III**)). Additionally, the lymphatic vessels were dilated in the otherwise healthy lymphatic insufficient mice as compared to littermate controls and this is seen as a significantly increased lymphatic vessel area (24.2 %) in lymphatic insufficient mice versus littermate controls (18.7 %) (Figure 3 in (**III**)). The attenuated lymphatic vessel function leads to the accumulation of extracellular water, which is visible in the T_2 relaxation time map (Figure 14).

The histological evaluation conduted in study (**III**) also revealed that the activation of lymphangiogenesis (VEGF-C) was found in both MI and healthy areas and VEGF-C was upregulated in both mouse groups at 8 days after MI (Figure 4 in (**III**)). Lymphatic vessels were forming a dense network in the border zone of the MI area in the littermate controls indicating the activation of lymphangiogenesis. Instead, lymphatic vessels were nearly absent 8 days after the MI in the lymphatic insufficient mice. In fact, the amount of lymphatic vessels was similar for the first 4 days after MI in both mouse groups but the amount of lymphatic vessels had increased significantly in the littermate controls at 8 days after the MI and remained elevated until the last time point. The mice with an insufficient lymphatic supply displayed only a slight increase in the amount of lymphatic vessels and the numbers of lymphatic vessels were significantly lower than in the littermate controls. These findings confirmed that strongly activated lymphangiogenesis exerted a healing effect on the myocardium after the MI.

The greatest capillary density was detected in both mouse groups on 4 day after the MI and the number of capillaries was significantly decreased at the later time points (Figure 5 in (**III**)). It is known that myocardial necrosis recruits inflammatory cells to clear damaged area of dead cells and matrix debris after the MI. Therefore, with the help of F4-80 (macrophages) and CD45 (lymphocytes) antibody stainings, it was possible to reveal the presence of macrophages mainly in the epicardium of the LV myocardium with lymphocytes being scattered throughout the MI area whereas no inflammatory cells were found in the healthy areas of myocardium (Figure 6 in (**III**)). Additionally, after the infiltration of inflammatory cells, proinflammatory signalling was suppressed and fibroblasts changed to become activated myofibroblasts, which started to produce collagen to protect the wall of the myocardium from rupture. In the littermate group, the amount of collagen was found to be significantly decreased at 42 days after the MI as compared to the situation at 8 days (Figure 14). These findings were also seen in Picro-Sirius red stained sections and interestingly, the intensity of collagen was fainter in several lymphatic insufficient mice as compared to littermate mice indicating that there were differences in the composition of the fibrotic area (Figure 14). However, the total amount of collagen was similar in both groups.

6 DISCUSSION

The goal of this thesis was to use recently developed MRI tools for characterizing MI in a normal and a lymphatic insufficient myocardium. One goal of this thesis was to measure $T_{1\rho}$ relaxation time in the MI area in normal mice at early and late time points in a non-invasive manner without the need for CAs *in vivo*. We used also different SL pulse powers to find an optimal contrast between MI and remote areas. The development of the novel RAFFn relaxation time method had been already undertaken to overcome the difficulties of $T_{1\rho}$ method and therefore, a goal of the thesis was to investigate RAFFn method in the characterization of MI at various time points after MI *in vivo* in both normal and lymphatic insufficient mouse models. A comparison was also performed of novel MRI findings to conventional MRI tools, cine imaging, CA imaging and histology.

One of the main finding in this thesis was the significant increase in $T_{1\rho}$ relaxation times at 7 days after the MI. This is in a good agreement with a study of chronic MI which had been examined in a swine model *in vivo* (Witschey WR et al. 2010). It has been shown elsewhere that the MI area is over 90 % necrotic at 2 days after the MI, which is transformed to granulation tissue at 7 days and to scar tissue at 14 days after the MI in mouse myocardium (Virag JL et al. 2003), which can be seen in our results as an increase in the $T_{1\rho}$ relaxation times at the same time points. Additionally, the literature suggests that the $T_{1\rho}$ relaxation time is sensitive to fibrosis (van Oorschot JW et al. 2015), the formation of both granulation and scar tissues (Witschey WR et al. 2010) instead of edema and necrosis during the development of MI. The determination of the MI size with cine imaging was in good agreement with Masson's trichrome histology staining. The decrease of EF in this study agrees well with the data obtained from normal C57BL mice (Schneider JE et al. 2003).

One major limiting factor for the use of $T_{1\rho}$ relaxation time measurement is the relatively high SAR (van Oorschot JW et al. 2015). Based on the experience gained in study **I**, SAR can be reduced by using the 500 Hz SL field with the length of maximum of 50 ms and minimum TR of 2.5 s in TurboRARE readout. However, reducing the SAR by changing imaging parameters or utilizing to lower $\mathbf{B}_0$ strengths, reduces the contrast in $T_{1\rho}$ measurements (Mäkelä HI et al. 2004). Additionally, reducing SAR in $T_{1\rho}$ measurements is not sufficient to avoid the heating of the tissue. Therefore, the development of the RAFFn method was clearly seen as one way to allow the determination of MI and for overcoming the limiting factors associated with the $T_{1\rho}$ measurements. RAFF4 has been proven to reduce SAR values by 80 % and RAFF2 by 30 % compared to $T_{1\rho}$ measurements.

The next goal was to determine whether at different times after an MI, there are different relaxation times by applying a novel relaxation time method called RAFFn. The relaxation time results were compared with LGE and Sirius Red histology results. As far as is known, this is the first time that RAFFn has been utilized in the heart *in vivo*.

The increase in T_{RAFFn} and the increase RRTDs were found in every time point at the MI area compared to the remote area. Additionally, a low AOE-value was determined by T_{RAFFn} relaxation time map and there was found to be a high correlation between increased T_{RAFFn} relaxation times and Sirius Red stained histology. Therefore, we have demonstrated that T_{RAFFn} relaxation time map is a trustworthy method to localize and characterize the MI. The MI area, as determined by the T_{RAFFn} relaxation time map, displayed a high correlation with the MI area in Sirius Red stained histology sections. It is known that the red area in Sirius Red stained histology sections represents the fibrotic areas and therefore, the T_{RAFFn} relaxation time map was able to differentiate fibrotic tissue from healthy tissue in the myocardium in chronic MI. It needs to be noted that our findings are based on quantitative results and not on weighted images. If we had intended to determine fibrosis accurately without CAs, then we would have required a broad range of clinical applications because there is no good non-invasive medical imaging tool for the determination of fibrosis. Fibrosis is a phenomenon involved in various diseases, for example amyloidosis, sarcoidosis and cardiac hypertrophy. Utilizing lower $\mathbf{B}_0$ strengths has an influence on the rotating relaxation times in a similar way as T_1 dependency to $\mathbf{B}_0$ (Mäkelä HI et al. 2004). It is good to bear in mind that our results were found in an MI mouse model with a permanent occlusion in one artery (LAD) and therefore, the adaption of our novel MRI method in the clinic will need further elaboration.

Measurements of $T_{1\rho}$ and T_2 were made for the comparison to RAFFn evaluations. The results demonstrated that the $T_{1\rho}$ relaxation time method was capable of detecting the MI area when the $T_{1\rho}$ relaxation time map was analyzed in various ways. These included the increased relaxation times as a function of time, RRTDs between the MI and remote areas, the MI sizes, small AOE-values, and a comparison with both hyperintensity areas in the LGE images and the red areas in Sirius Red stained histology sections; however, post-MI hemorrhage was not studied with histology. Conventional T_2 relaxation time is a useful tool for the determination of the acute phase of the MI since edema is increased in the acute MI area (Bönner F et al. 2014). We observed a significant increase of T_2 relaxation times at the early time points after the MI, which is in line with previous findings (Abdel-Aty H et al. 2004; Verhaert D et al. 2011; Bönner F et al. 2014). Additionally, due to edema and inflammation, the T_2 relaxation time map tends to overestimate the area of the MI, the findings observed here are supported by previous results (Abdel-Aty H et al. 2004). Finally, conventional cine images revealed decreased EF, increased EDV and ESV, and the dilation of LV as a function of time, which are all in line with published findings (Haberkom SM et al. 2017; Nahrendorf M et al. 2003) and reflect the physiological changes occuring after the MI.

One aim of the thesis was to utilize multiple ways to demonstrate the role of VEGFR-3 with respect to cardiac lymphatic vessels as well as in the healing after the MI. Since VEGFR-3 was malfunctioning, leading to an insufficient lymphatic function in the heart. It was hypothesized that after the MI, a myocardium with insufficient lymphatic vessels would become more edematous as compared to the situation in normal littermates. Thus, conventional T_2 relaxation time was used to assess edema and a cine technique was exploited to image the hearts *in vivo* after the MI. However, there were no significant changes in the T_2 relaxation time maps in the MI area in both groups of mice. Although the cardiac function parameters displayed differences, it is known that even small alterations in the tissue water content can impair the function of the heart (Laine GA et al., 1991; Henri O et al. 2016).

The conventional T_2 approach determines edema in the myocardium and due to findings emerging from the first study of this thesis, a novel MRI relaxation time method RAFFn was used to gather more information about the development of MI. The results showed that there were differences in the T_{RAFF4} relaxation times between the MI areas in the lymphatic insufficient mice and their control littermates. This difference between the MI areas is hypothetized that to have originated from the modified composition of the MI area because the $T_{1\rho}$ relaxation time map was not able to detect this difference whereas this was possible with T_{RAFFn} relaxation time maps. The data showed that the MI area in the mice with an insufficient lymphatic system had a reduced staining of type I and III collagen, which indicates either slower or elevated production of extracellular matrix components that might impair molecular motions in the tissue and therefore, might explain our MRI findings.

The MRI findings were also supported by evaluating the biology of cardiac lymphatics after the MI with multiple methods. Firstly, the downregulation of VEGFR-3 led to a significant dilation of cardiac lymphatic vessels, which modified the cardiac lymphatic morphology. Even though the changes in the structure of the lymphatic network were observed, cardiac lymphatic flow remained sufficient to maintain the fluid balance in the myocardium. This might explain the differences in the MI area in T_{RAFF4} relaxation times when $T_{1\rho}$ and T_2 relaxation times were similar in the MI areas between the different mice groups. Additionally, it is known that among other factors, cardiac edema is caused by the hyperpermeability and the leakiness of vasculature, which can trigger arrhythmias (Weis SM et al. 2005; Cui Y. 2010) and hemorrhages (Ghurge NR et al. 2017). The histology results show that there were large number of red blood cells, or large areas of post-MI hemorrhage, in the MI area at 8 days after MI in the insufficient lymphatic myocardium as compared to their control littermates suggesting that there had been an extravasation of erythrocytes from blood vessels (Figure 5 in study (**III**)); however, this finding was not detected in T_2 relaxation time maps (Figure 14). The presence of erythrocytes changes the local magnetic inhomogeneities, which decrease both T_2 and T_{RAFFn} relaxation times. There were no differences between the hearts of both mouse groups in the amounts of either macrophages or lymphocytes, which might explain similar T_2 relaxation times in both groups at the MI area. However, it is possible that other types of inflammatory cells may have invaded the infarcted area, contributing to a more severe outcome after MI in mice with hearts with an insufficient lymphatic system.

Novel and conventional MRI relaxation time methods were used to study the effects of the cardiac lymphatic system during the development of MI. The lymphatic system regulates many physiological and pathological processes and its role in the development of MI is currently unclear (Vuorio T et al. 2017). Interestingly, the AOD analysis showed that the MI area in the lymphatic insufficient myocardium was significantly larger according to the T_2 relaxation time map as compared to rotating frame relaxation time maps taken at later time points, which indicates that since the lymphatic system was inadequate, there was a larger edema area at the border zone of the MI in the insufficient lymphatic myocardium.

The MI area was more detectable in the T_{RAFFn} relaxation time maps in both mice groups i.e. lymphatic insufficient mice and their littermates when the area was compared to that assessed with the $T_{1\rho}$ and T_2 relaxation time maps, where the edges of MI area were not so clear that they could be detected by the human eye and the same resolution was used in every weighted images. In study (**III**), control littermates formed a denser lymphatic network at the border zone of the MI area whereas these were fainter in the borders of the MI area in the mice with an insufficient lymphatic system. This is support for the AOD results and also the MRI and histology findings, where higher correlations were found in MI sizes between Sirius Red stained secions and rotating frame relaxation time maps as compared to MI sizes in the correlation of Sirius Red stained sections and T_2 relaxation time map. This indicates that the actual infarct was smaller than the area displaying increased T_2 supporting the idea that there was increased edema in TG mice. Additionally, T_{RAFFn} relaxation time maps had the largest RRTD between the MI and remote areas between the mice groups. Findings in studies (**III**) and (**IV**) indicate that the T_{RAFFn} relaxation time together with T_2 relaxation time mapping is a sensitive method for characterizing the scar and the mixture of edema and fibrotic tissues in the MI area. Therefore, the combination of T_2 and T_{RAFFn} relaxation time mappings represents a satisfactory tool to study the effects of impaired lymphatic system after the MI.

Studies of cardiac lymphatic flow in humans (Nilsson JC et al. 2001) and in large animals (Ludwig LL et al. 1997) have indicated that MI decreases the cardiac lymphatic flow, which contributes to cardiac edema. Even though the results show a similarity between T_2 relaxation times, significant differences between the AOD-values and the observations of an unsharper MI area in Sirius Red stained sections in the lymphatic insufficient myocardium are evidence of the increased edema and fibrotic tissue in the border zone of the MI area in the mice with an insufficient lymphatic system in their myocardium. These findings highlight the importance of the lymphatic system during the development of MI.

Overall, the road to the development novel MRI relaxation time method RAFFn has been successful. The results of this thesis have revealed the potential of RAFFn for determining and localizing fibrotic MI *in vivo* non-invasively without any CAs and to overcome the limitations of the $T_{1\rho}$ relaxation time method. As well as its advantages in the determination and localization of the MI, RAFFn was able to differentiate the MI area in the myocardium of the lymphatic insufficient mice versus their littermate controls. T_{RAFFn} is sensitive at the same time to dipolar interactions, diffusion and exchange between adjacent *S*s, which are all factors that affect the contrast in the *in vivo* images.

Lower SAR values, together with a larger bandwidth and tolerance to $\mathbf{B}_0$ inhomogeneities, are beneficial properties for imaging the heart with RAFFn in clinics. There is an ongoing study where human MI hearts are being imaged with RAFFn (Mirmojarabian A et al. 2020) and the inital results have been promising.

Another advantage associated with the RAFFn method is its sensitivity to slow microscopic molecular motions, which occur in the frequency range of rotating frame RF pulses (τ_c is around of 10^{-1}-10^{-5} s). This advantage is useful in the determination of MI where slow microscopic molecular motions occur in the fibrotic, granulated, collagen-based matrix and scar tissues. Even though T_2 is also sensitive to slow molecular motions, the mechanism to measure the relaxing **M** with a different range of frequencies and τ_c's (around of 10^{-6}-10^{-9} s) after the RF pulse are making the difference between the T_2 and RAFFn methods in the sources of the measured signals from different bounded water molecules, or *S*s, and their environments. Furthermore, RAFFn measurements usually require less RF power to form the SL field as compared to $T_{1\rho}$ and $T_{2\rho}$ relaxation time measurements, leading to lower SAR values. The RAFFn contrast can be altered by modifying the pulse parameters such as the duration of the pulses, which changes the refocusing time of the irradiation, or the bandwidth and the flip angle of the pulse.

In the current implementation, a simple weighting and readout was used to demonstrate the measurements with a fairly long mapping duration. The imaging time of RAFFn method can be shortened by imaging without triggers, clever and sophisticated *k*-space sampling together with an optimized acquisition duration and 3D sampling but those improvements lie in the future and therefore are beyond the scope of this thesis. Additionally, the absolute origin of the RAFFn contrast is still partly unknown. Therefore, it will be essential to continue to refine the RAFFn technology in the future.

7 CONCLUSIONS

The following conclusions can be made based on the findings emerging from this thesis

1. The characterization of chronic MI with $T_{1\rho}$ mapping can be done accurately without CAs as determined by comparison with histology.

2. The characterization of acute and chronic MI with a novel T_{RAFFn} relaxation time can be achieved with high contrast and accuracy without the need for CAs with clinically tolerable specific absorption rates.

3. Novel MRI methods are able reveal the difference between normal and VEGFR3 downregulated MI; these evoke modifications in the cardiac lymphatic networks.

4. A combination of magnetic resonance imaging methods T_2 and T_{RAFFn} relaxation time mappings, but without having to administer CAs, is a satisfactory way for studying the effects of the impaired lymphatic system on the cardiac tissue after an MI; this tissue is known to contain a mixture of scar, fibrotic and edema tissues.

In summary, the studies in this thesis demonstrated and highlighted for the first time the use of novel T_{RAFFn} relaxation time mapping for a reliable determination of the myocardial infarction *in vivo* without any external contrast agents. Furthermore, the T_{RAFFn} relaxation time was shown to be sensitive to the presence of fibrosis in the myocardial infarct area without any need to increase the specific absorption rate, increasing its possibilities to be used in the clinical determination of fibrosis in the future. Additionally, the function of the lymphatic system during the MI development was found to play an important role, and this can be diagnosed and followed with both conventional and the rotating frame MRI relaxation time methods.

REFERENCES

Abdel-Aty H, Zagrosek A, Schulz-Menger J, Taylor AJ, Messroghli D et al. Delayed enhancement and T2-weighted cardiovascular magnetic resonance imaging differentiate acute from chronic myocardial infarction. *Circulation*. 2004 May 25;109(20):2411-2416.

Achen MG, Jeltsch M, Kukk E, Makinen T, Vitali A et al. Vascular endothelial growth factor D (VEGF-D) is a ligand for the tyrosine kinases VEGF receptor 2 (Flk1) and VEGF receptor 3 (Flt4). *Proc Natl Acad Sci U S A*. 1998 Jan 20;95(2):548-553.

Ailion DC, Slichter CP. Observation of ultra-slow translational diffusion in metallic lithium by magnetic resonance. *Physical Review*. 1965;137(1A):A235-A245.

Alitalo K. The lymphatic vasculature in disease. *Nat Med*. 2011 Nov 7; 17(11):1371-1380.

Andronesi OC, Bhat H, Reuter M, Mukherjee S, Caravan P et al. Whole brain mapping of water pools and molecular dynamics with rotating frame MR relaxation using gradient modulated low-power adiabatic pulses. *Neuroimage* 2014 Apr 1;89:92-109.

Apps A, Lau J, Peterzan M, Neubauer S, Tyler D et al. Hyperpolarized magnetic resonance for in vivo real-time metabolic imaging. *Heart*. 2018 Sep;104(18):1484-1491.

Aspelund A, Robciuc MR, Karaman S, Makinen T, Alitalo K. Lymphatic System in Cardiovascular Medicine. *Circ Res*. 2016 Feb 5;118(3):515-530.

Bakermans AJ, Abdurrachim D, Moonen RP, Motaal AG, Prompers JJ et al. Small animal cardiovascular MR imaging and spectroscopy. *Prog Nucl Magn Reson Spectrosc*. 2015 Aug;88-89:1-47.

Beer M, Stamm H, Machann W, Weng A, Goltz JP et al. Free breathing cardiac real-time cine MR without ECG triggering. *Int J Cardiol*. 2010 Nov 19;145(2):380-382.

Bendall MR, Pegg DT. Uniform sample excitation with surface coils for in vivo spectroscopy by adiabatic rapid half passage. *J magn reson*. 1986; 67:376-381.

Bengel FM, Higuchi T, Javadi MS, Lautamäki R. Cardiac positron emission tomography. *J Am Coll Cardiol*. 2009 Jun 30;54(1):1-15.

Berisha S, Han J, Shahid M, Han Y, Witschey WR. Measurement of myocardial $T_{1\rho}$ with a motion corrected, parametric mapping sequence in humans. *PLoS One*. 2016 Mar 22;11(3):e0151144.

Bernstein MA, King KF, Zhou XJ. *Handbook of MRI pulse sequences*. 1st ed. USA: Academic Press.

Bhave G, Lewis JB, Chang SS. Association of gadolinium based magnetic resonance imaging contrast agents and nephrogenic systemic fibrosis. *J Urol*. 2008; 180(3):830-835.

Biederman RW, Doyle M, Yamrozik J, 2008. *The Cardiovascular MRI Tutorial: Lectures and Learning*. Lippincott Williams & Wilkins, a Wolters Kluwer business.

Biederman RW, Doyle M, Yamrozik J, 2011. *Cardiac MRI: Guide book on the Go*. Lippincott Williams & Wilkins, a Wolters Kluwer business.

Blankesteijn WM, Creemers E, Lutgens E, Cleutjens JP, Daemen MJ, Smits JF. Dynamics of cardiac wound healing following myocardial infarction observations in genetically altered mice. *Acta Physiol Scand*. 2001 Sep;173(1):75-82.

Bolch F, Hansen W, Packard M, 1946. Nuclear Induction. *Physical Review*. vol. 69, p.127.

Breslin JW. Mechanical forces and lymphatic transport. *Microvasc Res*. 2014 Nov;96:46-54.

Brown MA, Semelka RC. *MRI: Basic principles and Applications*, 3rd ed. Hoboken: John Wiley & Sons, Inc. 2003.

Bui HM, Enis D, Robciuc MR, Nurmi HJ, Cohen J et al. Proteolytic activation defines distinct lymphangiogenic mechanisms for VEGFC and VEGFD. *J Clin Invest*. 2016 Jun 1;126(6):2167-2180.

Bulluck H, Hammond-Haley M, Fontana M, Knight DS, Sirker A et al. Quantification of both the area-at-risk and acute myocardial infarct size in ST-segment elevation myocardial infarction using T1-mapping. *J Carciovasc Magn Reson*. 2017 Aug 1;19(1):57.

Bönner F, Jacoby C, Temme S, Borg N, Ding Z, Schrader J et al. Multifunctional MR monitoring of the healing process after myocardial infarction. *Basic Res Cardiol*. 2014;109(5):430.

Camacho P, Fan H, Liu Z, He JQ. Small mammalian animal models of heart disease. *Am J Cardiovasc Dis*. 2016; Sep 15;6(3):70-80.

Captur G, Manisty C, Moon JC. Cardiac MRI evaluation of myocardial diseases. *Heart*. 2016 Sep 15;102(18):1429-1435.

Carr HY, Purcell EM. Effect of Diffusion on free precession in nuclear magnetic resonance experiments. *Physical Review*. 1954;94(3):630-638.

Colucci WS. Molecular and cellular mechanisms of myocardial failure. *Am J Cardiol*. 1997 Dec 4;80(11A):15L-25L

Coolen BF, Geelen T, Paulis LE, Nauerth A, Nicolay K, Strijkers GJ. Three-dimensional T1 mapping of the mouse heart using variable flip angle steady-state MR imaging. *NMR Biomed*. 2011 Feb;24(2):154-162.

Coolen BF, Paulis LE, Geelen T, Nicolay K, Strijkers GJ. Contrast-enhanced MRI of murine myocardial infarction – part II. *NMR Biomed*. 2012 Aug;25(8):969-684.

Cowan B, 1997. *Nuclear Magnetic Resoance and Relaxation*. New York, Cambridge Univeristy Press.

Cui Y. The role of lymphatic vessels in the heart. *Pathophysiology: the official journal of the International Society for Pathophysiology / ISP*. 2010;17(4):307-314.

Davis KL, Laine GA, Geissler HJ, Mehlhorn U, Brennan M, Allen SJ. Effects of myocardial edema on the development of myocardial interstitial fibrosis. *Microcirculation (New York, N.Y.: 1994)*. 2000;7(4):269-280.

Deschamps M, Kervern G, Massiot D, Pintacuda G, Emsley L, Gradinetti PJ. Superadiabaticity in magnetic resonance. *J Chem Phys*. 2008 Nov 28; 129(20):204110.

Ellermann J, Ling W, Nissi MJ, Arendt E, Carlson CS, Garwood M et al. MRI rotating frame relaxation measurements for articular cartilage assessment. *Magn Reson Imaging*. 2013 Nov;31(9):1537-1543.

Ertl G, Frantz S. Healing after myocardial infarction. *Cardiovasc Res*. 2005 Apr 1;66(1):22-32.

Fahmy AS, Neisius U, Tsao CW, Berg S, Goddu E, Pierce P et al. Gray blood late gadolinium enhancement cardiovascular magnetic resonance for improved detection of myocardial scar. *J Cardiovasc Magn Reson*. 2018 Mar 22;20(1):22.

Faust O, Archarya UR, Sudarshan VK, Tan RS, Yeong CH et al. Computer aided diagnosis of coronary artery disease, myocardial infarction and carotid atherosclerosis using ultrasound images: A review. *Phys Med*. 2017 Jan;33:1-15.

Ferrari VA, Witschey WR, Zhou R. Cardiac magnetic resonance assessment of myocardial fibrosis: honing new clinical tools. *Circ Cardiovasc Imaging*. 2011, Nov;4(6):604-606.

Frangogiannis NG. The inflammatory response in myocardial injury, repair, and remodeling. *Nat Rev Cardiol*. 2014 May;11(5):255-265.

Gadian DG, 1995. *NMR and its applications to living systems*. 2nd ed. United Stated: Oxford University Press.

Galli A, Lombardi F. Postinfarct left ventricular remodeling: A prevailing cause of heart failure. *Cardiol Res Pract*. 2016;2016:2579832.

Gao E, Lei YH, Shang X, Huang ZM, Zuo L, Boucher M et al. *Circ Res*. 2010 Dec 10;107(12):1445-1453.

Garg P, Saunders LC, Swift AJ, Wild JM, Plein S. Role of cardiac T1 mapping and extracellular volume in the assessment of myocardial infarction. *Anatol J Cardiol*. 2018 Jun;19(6):404-411.

Garwood M, Delabarre L. The return of the frequency sweep: designing adiabatic pulses for comporary NMR. *J Magn Reson*. 2001 Dec;153(2):155-177.

Garwood M, Nease B, Ke Y, Degraaf RA, Merkle H. Simultaneous compensation for B1 inhomogeneity and resonance offsets by a multiple-quantum NMR sequence using adiabatic pulses. *J Magn Reson*. 1995; Series A:112(2): 272-274.

Geelen T, Paulis LE, Coolen BF, Nicolay K, Strijkers GJ. Contrast-enhanced MRI of murine myocardial infarction – part I. *NMR biomed*. 2012 Aug;25(8):953-968.

Ghurge NR, Pop M, Thomas R, Newbigging S, Qi X, Barry J et al. Hemorrhage promotes inflammation and myocardial damage following acute myocardial infarction: insights from a novel preclinical model and cardiovascular magnetic resonance. *J of Cardiovasc Magn Reson: official journal of the Society for Cardiovascular Magnetic Resonance*. 2017;19(1):50-017-0361-7.

Global Health Estimates 2016: Disease burden by Cause, Age, Sex, by Countrey and by Region, 2000-2016. Geneva, World Health Organization; 2018.

Haacke EM, Brown RW, Thompson MR, Venkatesan R, 1999. *Magnetic Resonance Imaging: Physical Principles and Sequence Design*, New York: John Wiley & Sons, Inc.

Haaf P, Garg P, Messroghli DR, Broadbent DA, Greenwood JP et al. Cardiac T1 Mapping and Extracellular Volume (ECV) in clical practice: a comprehensive review. *J Cardiovasc Magn Reson*. 2016 Nov 30;18(1):89.

Haberkorn SM, Jacoby C, Ding Z, Keul P, Bönner F, Polzin A et al. Cardiovascular Magnetic Resonance Relaxometry Predicts Regional Functional Outcome After Experimental Myocardial Infarction. *Circ Cardiovasc Imaging*. 2017 Aug;10(8): pii: e006025

Hahn EL. Spin Echoes. *Physical Review*. 1950;80:580-594.

Hakkarainen H, Sierra A, Mangia S, Garwood M, Michaeli S, Gröhn O et al. MRI relaxation in the presence of fictitious fields correlates with myelin content in normal rat brain. *Magn Reson Med*. 2016 Jan;75(1):161-168.

Hall JE, 2011. *Guyton and Hall Textbook of Medical Physiology*. Saundres Elsevier.

Han Y, Liimatainen T, Gorman RC, Witschey WR. Assessing myocardial disease using T1ρ MRI. *Curr Cardiovasc Imaging Rep*. 2014 Feb 1;7(2):9248.

Heinolainen K, Karaman S, D'Amico G, Tammela T, Sormunen R et al. VEGFR3 Modulates Vascular Permeability by Controlling VEGF/VEGFR2 Signaling. *Circ Res*. 2017 Apr 28;120(9):1414-1425.

Henri O, Pouehe C, Houssari M, Galas L, Nicol L, Edwards-Lvey F et al. Selective Stimulation of Cardiac Lymphagiogenesis Reduces Myocardial Edema and Fibrosis Leading to Improved Cardiac Function Following Myocardial Infarction. *Circulation*. 2016;133(15):1484-1497.

Hieda M, Howden EJ, Sarma S, Cornwell W, Lawley JS et al. The impact of 2 years of high-intensity exercise training on a model of integrated cardiovascular regulation. *J Physiol*. 2019 Jan;597(2):419-429.

Huang LH, Lavine KJ, Randolph GJ. Cardiac Lymphatic Vessels, Transport, and Healing of the Infarcted Heart. *JACC: Basic to translat sci*. 2017;2(4):477-483.

Huber S, Muthupillai R, Lambert B, Pereyra M, Napoli A et al. Tissue characterization of myocardial infarction using T1rho: influence of contrast dose and time of imaging after contrast administration. *J Magn Reson Imaging*. 2006 Nov;24(5):1040-1046.

Huettel SA, Song AW, McCarthy G, 2004. *Functional Magnetic Resonance Imaging*. Sinauer Associates, Inc, Sunderland, MA.

Hurst JW, 2011. *Hurst's The Heart*. Mc Graw Hill Medical.

Huusko J, Merentie M, Dijkstra MH, Ryhänen MM, Karvinen H et al. The effects of VEGF-R1 and VEGF-R2 ligands on angiogenic responses and left ventricular function in mice. *Cardiovasc Res*. 2010 Apr 1;86(1):122-130.

Ishida M, Kato S, Sakuma H. Cardiac MRI in ischemic heart disease. *Circ J*. 2009 Sep;73(9):1577-1588.

Jambor I, Pesola M, Merisaari H, Taimen P, Boström PJ, Liimatainen T et al. 2016a. Relaxation along a fictitious field, diffusion-weighted imaging, and T2 mapping of prostate cancer: Prediction of cancer aggressiveness. *Magn Reson Med*. 2016 May;75(5):2130-2140.

Jambor I, Pesola M, Taimen P, Merisaari H, Boström PJ, Minn H et al. 2016b. Rotating frame relaxation imaging of prostate cancer: Repeatibility, cancer detection, and Gleason score prediction. *Magn Reson Med*. 2016 Jan;75(1):337-344.

James TN, Sherf L. Fine structure of the His bundle. *Circulation*. 1971 Jul;44(1):9-28.

Janssen L, Dupont L, Bekhouche M, Noel A, Leduc C et al. ADAMTS3 activity in mandatory for embryonic lymphangiogenesis and regulates placental angiogenesis. *Angiogenesis*. 2016 Jan;19(1):53-65.

Jarvelainen H, Sainio A, Koulu M, Wight TN, Penttinen R. Extracellular matrix molecules: potential targets in pharmacotherapy. *Pharmacol Rev*. 2009 Jun;61(2):198-223.

Jokivarsi KT, Liimatainen T, Kauppinen RA, Gröhn OH, Närväinen J. Relaxation along a fictitious field (RAFF) and Z-spectroscopy using alternating-phase irradiation (ZAPI) in permanent focal cerebral ischemia in rat. *PLoS One*. 2013 Jul 17;8(7):e69157.

Jones GP. Spin-Lattice Relaxation in the Rotating Frame: Weak-Collision Case. *Phyiscal review*. 1966;148(1):332-335.

Joukov V, Pajusola K, Kaipainen A, Chilov D, Lahtinen I et al. A novel vascular endothelial growth factor, VEGF-C, is a ligand for the Flt4 (VEGFR-3) and KDR (VEGFR-2) receptor tyrosine kinases. *EMBO J*. 1996 Apr 1;15(7):1751.

Kaipainen A, Korhonen J, Mustonen T, van Hinsbergh VW, Fang GH et al. Expression of the fms-like tyrosine kinase 4 gene becomes restricted to lymphatic endothelium during development. *Proc Natl Acad Sci U S A*. 1995 Apr 11;92(8):3566-3570.

Kali A, Cokic I, Tang RL, Yang HJ, Sharif B, Marban E et al. Determination of location, size, and transmurality of chronic myocardial infarction without exogenous contrast media by using cardiac magnetic resonance imaging at 3T. *Circ Cardiovasc Imaging*. 2014 May; 7(3):471-481.

Karkkainen MJ, Ferrell RE, Lawrence EC, Kimak MA, Levinson KL et al. Missense mutations interfere with VEGFR-3 signalling in primary lympoedema. *Nat Genet*. 2000 Jun;25(2):153-159.

Karkkainen MJ, Haiko P, Sainio K, Partanen J, Taipale J et al. Vascular endothelial growth factor C is reguired for sprouting of the first lymphatic vessels from embryonic veins. *Nat Immunol*. 2004 Jan;5(1):74-80.

Khan JN, McCann GP. Cardiovascular magnetic resonance imaging assessment of outcomes in acute myocardial infarction. *World J Cardiol*. 2017 Feb 26;9(2):109-133.

Khan MA, Laakso H, Laidinen S, Kettunen S, Heikura T, Ylä-Herttuala S et al. The follow-up of progressive hypertrophic cardiomyopathy using magnetic resonance rotating frame relaxation times. *NMR Biomed*. 2018 Feb;31(2).

Kholova I, Dragneva G, Cermakova P, Laidinen S, Kaskenpaa N, Hazes T et al. Lymphatic vasculature is increased in heart valves, ischemic and inflamed hearts and in cholesterol-rich and calcified atherosclerotic lesions. *Eur J Clinical Investigation*. 2011;41(5):487-497.

Kim H, Kataru RP, Koh GY. Inflammation-associated lymphangiogenesis: a double-edged sword? *J Clin Invest*. 2014 Mar;124(3):936-942.

Kim KW, Song JH. Emerging Roles of Lymphatic Vasculature in Immunity. *Immune Netw*. 2017 Feb;17(1):68-76.

Kis E, Ablonczy L, Reusz GS. Cardiac Magnetic Resonance Imaging of the Myocardium in Chronic Kidney Disease. *Kidney Blood Press Res*. 2018;43(1):134-142.

Klabunde RE. Cardiac electrophysiology: normal and ischemic ionic currents and the ECG. *Adv Physiol Educ*. 2017 Mar 1;41(1):29-37.

Klein C, Nekolla SG, Balbach T, Schnackenburg B, Nagel E et al. The influence of myocardial blood flow and volume of distribution on late Gd-DTPA kinetics in ischemic heart failure. *J Magn Reson Imaging*. 2004 Oct;(20(4):588-593

Klotz L, Norman S, Vieira JM, Masters M, Rohling M et al. Cardiac lymphatics are heterogeneous in origin and respond to injury. *Nature*. 2915 Jun 4;522(7554):62-67.

Krause W. *Contrast Agents 1; Magnetic resonance imaging*, Springer, 2002.

Krumm P, Zitzelsberger T, Weinmann M, Mangold S, Rath D et al. Cardiac MRI left ventricular global function index and quantitative late gadolinium enhancement in unrecognized myocardial infarction. *Eur J Radiol*. 2017 Jul;92:11-16.

Krämer M, Hermann KH, Biermann J, Freiburger S, Schwarzer M et al. Self-gated cardiac Cine MRI of the of the rat on a clinical 3 T MRI system. *NMR Biomed*. 2015 Feb;28(2):162-167.

Kumar V, 2015. *Robbins & Cotran pathologic basis of disease*. Elsevies Saunders.

Kurtz TW, Lujan HL, DiCarlo SE. The 24 h pattern of arterial pressure in mice is determined mainly by heart rate-driven variation in cardiac output. *Physiol Rep*. 2014 Nov 26;2(11). pii: e12223.

Laakso H, Wirth G, Korpisalo P, Ylä-Herttuala E, Michaeli S, Ylä-Herttuala S et al. T_2, $T_{1\rho}$ and T_{RAFF4} detect early regenerative changes in mouse ischemic skeletal muscle. *NMR Biomed*. 2018 May;31(5):e3909.

Laakso H, Ylä-Herttuala E, Sierra A, Jambor I, Poutanen M, Liljenbäck H et al. Docetaxel Chemotherapy Response in PC3 Prostate Cancer Mouse Model Detected by Rotating Frame Relaxations and Water Diffusion. Submitted 3/2020.

Laine GA, Allen SJ. Left ventricular myocardial edema. Lymph flow, interstitial fibrosis, and cardiac function. *Circ Res*. 1991; 68(6):1713-1721.

Laurent S, Elst LV, Muller RN. Comparative study of the physicochemical properties of six clinical low molecular weight gadolinium contrast agents. *Contrast Media Mol Imaging*. 2006; May-Jun;1(3)128-137.

Lauterbur PC. Image Formation by Induced Local Interactions: Examples Employing Nuclear Magnetic Resonance. *Nature*. 1973;242:5394:190-191.

Lavin B, Protti A, Lorrio S, Dong X, Phinikaridou A et al. MRI with gadofosveset: A potential marker for permeability on myocardial infarction. *Atherosclerosis*. 2018 Aug;275:400-408.

Lehto LJ, Albors AA, Sierra A, Tolppanen L, Eberly LE, Mangia S et al. Lysophosphatidyl Choline Induced Demyelination in Rat Probed by Relaxation along a Fictitious Field in High Rank Rotating Frame. *Front Neurosci*. 2017 Aug 3;11:433.

Leiner T, Strijkers G. Advances in cardiovascular MR imaging. *MAGMA*. 2018 Feb;31(1):3-6.

Levitt MH, 2008. *Spin dynamics*, Chichester: John Wiley & Sons Ltd.

Liimatainen T, Source DJ, O'Connell R, Garwood M, Michaeli S. MRI contrast from relaxation along a fictitious field. *Magn Reason Med*. 2010 Oct;64(4):983-994

Liimatainen T, Mangia S, Ling W, Ellermann J, Source DJ, Garwood M et al. Relaxation dispersion in MRI induced by fictitious magnetic fields. *J Magn Reason*. 2011 Apr;209(2):269-276.

Liimatainen T, Sierra A, Hanson T, Sorce DJ, Ylä-Herttuala S, Garwood M et al. Glioma cell density in a rat gene therapy model gauged by water relaxation rate along a fictitious magnetic field. *Magn Reson Med*. 2012 Jan;67(1):269-277.

Liimatainen T, Hakkarainen H, Mangia S, Huttunen JM, Storino C, Idiyatullin D et al. MRI contrasts in high rank rotating frames. *Magn Reason Med*. 2015 Jan;73(1):254-262.

Liu J, Feng L, Shen HW, Zhu C, Wang Y et al. Highly-accelerated self-gated free-breathing 3D cardiac cine MRI: validation in assessment of left ventricular function. *MAGMA*. 2017 Aug;30(4):337-346.

Ludwig LL, Schertel ER, Pratt JW, McClure DE, Ying AJ, Heck CF et al. Impairment of left ventricular function by acute cardiac lymphatic obstruction. *Cardiovasc Res*. 1997 Jan;33(1):164-171.

Lähteenvuo JE, Lähteenvuo MT, Kivelä A, Rosenlew C, Falkwall A et al. Vascular endothelial growth factor-B induces myocardium-specific angiogenesis and arteriogenesis via vascular endothelial growth factor receptor-1-and neuropilin receptor-1-dependent mechanisms. *Circulation*. 2009 Feb 17;119(6):845-856.

Maestrini V, Treibel TA, White SK, Fontana M, Moon JC. T1 mapping for Characterization of Intracellular and Extracellular myocardial Diseases in Heart Failure. *Curr Cardiovasc Imaging Rep*. 2014;7:9287.

Makinen T, Jussila L, Veikkola T, Karpanen T, Kettunen MI et al. Inhibition of lymphangiogenesis with resulting lymphedema in transgenic mice expressing soluble VEGF receptor-3. *Nat Med*. 2001 Feb;7(2):199-205.

Mangia S, Liimatainen T, Garwood M, Michaeli S. Rotating frame relaxation during adiabatic pulses vs. conventional spin lock: simulations and experimental results at 4 T. *Magn Reson Imaging*. 2009;27(8):1974-1087.

Martel C, Li W, Fulp B, Platt AM, Gautier EL, Weterterp M et al. Lymphatic vasculature mediates macrophage reverse cholesterol transport in mice. *J Clin Invest*. 2013 Apr;123(4):1571-1579.

Mavrogeni S, Apostolou D, Argyriou P, Velitsista S, Papa L et al. T1 and T2 mapping in Cardiology: "Mapping the Obscure Object of Desire". *Cardiology*. 2017;138(4):207-217.

Medzhitov R. Inflammation 2010: new adventures of an old flame. *Cell*. 2010 Mar 19;140(6):771-776.

McRobbie DW, Moore EA, Graves MJ, Prince MR, 2007. *MRI from picture to proton*, Cambridge University Press.

Messroghli DR, Moon JC, Ferreira VM, Grosse-Wortmann L, He T, Kellman P et al. Clinical recommendations for cardiovascular magnetic resonance mapping of T1, T2, T2* and extracellular volume: A consensus statement by the Society for Cardiovascular Magnetic Resonance (SCMR) endorsed by the European Association for Cardiovascular Imaging (EACVI). *J Cardiovasc Magn Reson*. 2017 Oct9;19(1):74.

Michaeli S, Sorce D, Springer C, Ugurbil K, Garwood M. $T_{1\rho}$ MRI conrtrast in the huma brain: modulation of the longitudinal rotating frame relaxation shutter-speed during an adiabatic RF pulse. *J Magn Reson*. 2006;181:138-150.

Michaeli S, Sorce DJ, Garwood M. T_2 and $T_{1\rho}$ adiabatic relaxations and contrasts. *Curr Anal Chem*. 2008;4(1):8-25.

Milani-Nejad N, Janssen PM. Small and large animal models in cardiac contraction research: advantages and disadvantages. *Pharmacol Ther*. 2014 Mar;141(3):235-249.

Mirmojarabian A et al. Myocardial infarct characterization using relaxation along fictitious field in the nth rotating frame. Submitted 2020.

Moghari MH, Barthur A, Amaral ME, Geva T, Powell AJ. Free-breathing whole-heart 3D cine magnetic resonance imaging with prospective respiratory motion compensation. *Magn Reson Med*. 2018 Jul;80(1):181-189.

Mozaffarian D, Benjamin EJ, Go AS, Arnett DK, Blaha MJ, Cushman M et al. Heart disease and stroke statistics—2015 update: a report from the American Heart Association. *Circulation* 2015 Jan;131(4):e29-322.

Mäkelä HI, De Vita E, Gröhn OH, Kettunen MI, Kavec M, Lythgoe et al. B0 dependence of the on-resonance longitudinal relaxation time in the rotating frame (T1rho) in protein phantoms and rat brain in vivo. *Magn Reson Med*. 2004 Jan;51(1):4-8.

Nahrendorf M, Hiller KH, Hu K, Ertl G, Haase A, Bauer WR. Cardiac magnetic resonance imaging in small animal models of human heart failure. *Med Image Anal*. 2003 Sep;7(3):369-375.

Nerbonne JM, Kass RS. Molecular physiology of cardiac repolarization. *Physiol Rev*. 2005 Oct;85(4):1205-1253.

Nilsson JC, Nielsen G, Groenning BA, Fritz-Hansen T, Sondergaard L, Jensen BG et al. Sustained postinfarction myocardial oedema in humans visualised by magnetic resonance imaging. *Heart (British Cardiac Society)*. 2001;53(1):639-642.

Nishimura DG, 2010. Principles of Magnetic Resonance Imaging. 1.1st ed.

Norman S, Riley PR. Anatomy and development of the cardiac lymphatic vasculature: its role in injury and disease. *Clinical anat (New York, N.Y.)*. 2016;29(3):305-315.

Nurro J, Halonen PJ, Kuivanen A, Tarkia M, Saraste A et al. AdVEGF-B186 and AdVEGF-DDeltaNDeltaC induce angiogenesis and increase perfusion in porcine myocardium. *Heart*. 2016 Nov 1;102(21):1716-1720.

Olsson AK, Dimberg A, Kreuger J, Claesson-Welsh L. VEGF receptor signaling – in control of vascular function. *Nat Rev Mol Cell Biol*. 2006 May;7(5):359-371.

Opie LH, Commerford PJ, Gersh BJ, Pfeffer MA. Controversies in ventricular remodeling. *Lancet*. 2006 Jan 28;367(9507):356-367.

Palazzuoli A, Beltrami M, Gennari L, Dastidar AG, Nuti R et al. The impact of infarct size on regional and global left ventricular systolic function: a cardiac magnetic resonance imaging study. *Int J Cardiovasc Imaging*. 2015 Jun;31(5):1037-1044.

Podkorytov IS, Skrynnikov NR. Microsecond time-scale dynamics from relaxation in the rotating frame: experiments using spin lock with alternating phase. *J Magn Reson*. 2004 Jul;169(1):164-173.

Price AN, Chaeung KK, Lim SY, Yellon DM, Hausenloy DJ, Lythgoe MF. *J Cardiovasc Magn Reason*. 2011 Sept 5;13:44.

Protti A, Dong X, Sirker A, Botnar R, Shah AM. MRI-based prediction of adverse cardiac remodelling after murine myocardial infarction. *Am J Physiol Heart Circ Physiol*. 2012 Aug 1;303(3):H309-H314.

Purcell E, Torrey H, Puond RPR, 1946. Resonance absorption by nuclear magnetic moments in a solid. *Physical Review*. vol. 69, p 37-38.

Radenkovic D, Weingärtner S, Ricketts LMoon JC, Captur G. T_1 mapping in cardiac MRI. *Heart Fail Rev*. 2017 Jul;22(4):415-430.

Randolph GJ, Ivanov S, Zinselmeyer BH, Scallan JP. The Lymphatic System: Integral Roles in Immunity. *Annu Rev Immunol*. 2017 Apr 26;35:31-52.

Ratajska A, Gula G, Flath-Zabost A, Czarnowska E, Ciszek B, Jankowska-Steifer E et al. Comparative and development anatomy of cardiac lymphatics. *ScientificWorldJournal*. 2014 Jan 27;2014:183170.

Rautiainen J, Nissi MJ, Salo EN, Tiitu V, Finnilä MAJ et al. Multiparametric MRI assessment of human articular cartilage degeneration: Correlation with quantative histology and mechanical properties. Magn Reson Med. 2015 Jul;74(1):249-259.

Recchia FA, Lionetti V. Animal models of dilated cardiomyopathy for translational research. *Vet Res Commun*. 2007 Aug;31 Suppl 1:35-41.

Redfield AG. Nuclear Magnetic Resonance Saturation and Rotary Saturation in Solids. *Physical review*. 1955; 98(6):1787-1809.

Rissanen TT, Markkanen JE, Gruchala M, Heikura T, Puranen A et al. VEGF-D is the strongest angiogenic and lymphangiogenic effector among VEGFs delivered into skeletal muscle via adenoviruses. *Circ Res*. 2003 May 30;92(10):1098-1106.

Rhoades R, Pflanzer R, 2003. *Human Physiology*, 4th edn, Thomson Learining Inc., Oacific Grove, The United States of America.

Robbers LF, Baars EN, Brouwer WP, Beek AM, Hofman MB et al. Ti mapping shows increased extracellular matrix size in the myocardium due to amyloid depositions. *Circ Cardiovasc Imaging*. 2012 May 1;5(3):423-426.

Saaed M, Van TA, Krug R, Hetts SW, Wilson MW. Cardiac MR imaging: current status and future direction. *Cardiovasc Diagn Ther*. 2015 Aug;5(4):290-310.

Saeed M, Liu H, Liang CH, Wilson MW. Magnetic resonance imaging for characterizing myocardial diseases. *Int J Cardiovasc Imaging*. 2017 Sep;33(9):1395-1414.

Saffitz JE, Corradi D. The electrical heart: 25 years of discovery in cardiac electrophysiology, arrhythmias and sudden death. *Cardiovasc Pathol*. 2016 Mar-Apr;25(2):149-157.

Sanches PG, Op 't Veld RC, de Graaf W, Strijkers GJ, Grull H. Novel axolotl cardiac function analysis method using magnetic resonance imaging. *PLoS One*. 2017 Aug 24;12(8):e0183446.

Sanz J, LaRocca G, Mirelis JG. Myocardial mapping with cardiac magnetic resonance: the diagnostic value of novel sequences. *Rev Esp Cardiol (Engl Ed)*. 2016 Sep;69(9):849-861.

Schneider JE, Cassidy PJ, Lygate C, Tyler DJ, Wiesmann F et al. Fast, high-resolution in vivo cine magnetic resonance imaging in normal and failing mouse hearts on a vertical 11.7 T system. *J Magn Reson Imaging*. 2003 Dec;18(6):691-701.

Schneider JE, Lanz T, Barnes H, Medway D, Stork LA et al. Ultra-fast and accurate assessment of cardiac function in rats using accelerated MRI at 9.4 Tesla. *Magn Reson Med*. 2008 Mar;59(3):636-641.

Sherwood L, 2012. *Human Physiology: From Cells to Systems*. Cengage Learning.

Sepponen RE, Pohjonen JA, Sipponen JT, Tanttu JI. A method for T1ρ imaging. *J Comput Assist Tomogr*. 1985 Nov-Dec;9(6):1007-1011.

Sibley CT, Noureldin RA, Gai N, Nacif MS, Lui S et al. T1 Mapping in cardiomyopathy at cardiac MR: comparison with endomyocardial biopsy. *Radiology*. 2012 Dec;265(3):724-732.

Silver MS, Joseph RI, Hoult DI. Highly selective π/2 and π pulse generation. *J Magn Reson*. 1984 Sep;69:347-351.

Stoffers RH, Madden M, Shahid M, Contijoch F, Solomon J, Pilla JJ et al. Erratum to: Assessment of myocardial injury after reperfused infarction by T1ρ cardiovascular magnetic resonance. *J Cardiovasc Magn Reason*. 2017 Mar 25;19(1):42.

Strijkers GJ, Mulder WJ, van Tilborg GA, Nicolay K. MRI contrast agents: current status and future perspectives. *Anticancer Agents Med Chem*. 2007 May;7(3):291-305.

Stuckey DJ, Carr CA, Tyler DJ, Clarke K. Cine-MRI versus two-dimensional echocardiography to measure in vivo left ventricular function on rat heart. *NMR Biomed*. 2008 Aug;21(7):765-772.

Stuckey DJ, Carr CA, Tyler DJ, Aasum E, Clarke K. Novel MRI method to detect altered left ventricular ejection and filling patterns in rodent models of disease. *Magn Reson Med*. 2008 Sep;60(3):582-587.

Solomon I. Relaxation processes in a system of two spins. *Physical Review*. 1955;99(2):559-565.

Solomon I. Rotary spin echoes. *Physical Review Letters*. 1959;2(7):201-305.

Taber CW, Thomas CL, Venes D, 2009. *Taber's Cyclopedic Medical Dictionary*. 19th ed. F. A. Davis Co. pp: 1018-1023.

Talman V, Ruskoaho H. Cardiac fibrosis in myocardial infarction-from repair and remodeling to regeneration. *Cell Tissue Res*. 2016 Sep;365(3):563-581.

Tannús A, Garwood M. Adiabatic pulses. *NMR Biomed*. 1997;10(8):423-434.

Tannús A, Garwood M. Improved Performance of Frequency-Swept Pulses Using Offset-Independent Adiabiticity. *J Magn Reson*. 1996; Series A:120(1):133-137.

Thygesen K, Alpert JS, Jaffe AS, Simoons ML, Chaitman BR, White HD, Writing Group on the Joint ESC/ACCF/AHA/WHF Task Force for the Universal Definition of Myocardial Infarction & ESC Committee for Practice Guidelines (CPG) et al. Third Universal definition of myocardial infarction. *Eur Heart J*. 2012 Oct;33(20):2551-2567.

Timm KN, Miller JJ, Henry JA, Tyler DJ. Cardiac applications of hyperpolarized magnetic resonance. *Prog Nucl Magn Reson Spectrosc*. 2018 Jun – Aug;106-107:66-87.

Torrente AG, Zhang R, Zainii A, Giani J, Kang ST et al. Burst pacemaker activity of the sinoatrial node in sodium-calcium exchanger knockout mice. *Proc Natl Acad Sci U S A*. 2015 Aug 4;112(31):9769-9774.

Tyler DJ, Lygate CA, Schneider JE, Cassidy PJ, Neubauer S et al. CINE-MR imaging of the normal and infarcted rat heart using an 11.7 T vertical bore MR system. *J Cardiovasc Magn Reson*. 2006;8(2):327-333.

van Oorschot JW, El Aidi H, Jansen Of Lorkeers SJ, Gho JM, Froeling M, Visser F et al. Endogenous assessment of chronic myocardial infarction wit T(1ρ)-mapping in patients. *J Cardiovasc Magn Reson*. 2014 Dec 20;16:104.

van Oorschot JW, Gho JM, van Hout GP, Froeling M, Jansen Of Lorkeers SJ, Hoefer IE et al. Endogenous contrast MRI of cardiac fibrosis: beyond late gadolinium enhancement. *J Magn Reson Imaging*. 2015 May;41(5):1181-1189.

van Oorschot JW, Guclu F, de Jong S, Charmuleau SA, Luijten PR, Leiner T et al. Endogenous assessment of diffuse myocardial fibrosis in patients with T1ρ-mapping. *J Magn Reson Imaging*. 2017 Jan;45(1):132-138.

Vaughan JT, Adriany G, Garwood M, Yacoub E, Duong T et al. Detunable transverse electromagnetic (TEM) volume coil for high-field NMR. *Magn Reson Med*. 2002 May;47(5):990-1000.

Verhaert D, Thavendiranathan P, Giri S, Mihai G, Rajagopalan S, Simonetti OP et al. Direct T2 quantification of myocardial edema in acute ischemic injury. *JACC Cardiovasc Imaging*. 2011 Mar;4(3):269-278.

Virag JL, Murry CE. Myofibroblast and endothelial cell proliferation during murine myocardial infarct repair. *Am J Pathol*. 2003 Dec;163(6):2433-2440.

Vliegenthart R, Henzler T, Moscariello A, Ruzsics B, Bastarrika G et al. CT of coronary heart disease: Part 1, CT of myocardial infarction, ischemia, and viability. *AJR Am J Roentgenol*. 2012 Mar;198(3):531-547.

Vuorio T, Tirronen A, Ylä-Herttuala S. Cardiac Lymphatics – A New Avenue for Therapeutics? *Trends Endocrinol Metab*. 2017 Apr;28(4):285-296.

Vuorio T, Nurmi H, Moulton K, Kurkipuro J, Robciuc MR et al. Lymphatic vessel insufficiency in hypercholesterolemic mice alters lipoprotein levels and promotes atherogenesis. *Arterioscler Thromb Vasc Biol*. 2014 Jun;34(6):1162-1170.

Wang C, Zheng J, Sun J, Wang Y, Xia R et al. Endogenous contrast T1rho cardiac magnetic resonance for myocardial fibrosis in hypertrophic cardiomyopathy patients. *J Cardiol*. 2015 Dec;66(6):520-526.

Warwick R, Williams PL, 1973. *Grey's anatomy*. 35th ed. London: Longman.

Weis SM, Cheresh DA. Pathophysiological consequences of VEGF-induced vascular permeability. *Nature*. 2005;437(7058):497-504.

Whitfield G, Redfield AG. Paramagnetic resonance detection along the polarizing field direction. *Physical Review*. 1957;106(5):918-920.

Wiig H, Swartz MA. Interstitial fluid and lymph formation and transport: physiological regulation and roles in inflammation and cancer. *Physiol Rev*. 2012 Jul;92(3):1005-1060.

Witschey WR, Borthakur A, Elliott MA, Mellon E, Niyogi S et al. Compentsation for spin-lock artifacts using an off-resonance rotary echo in T1rhooff-weighted imaging. *Magn Reson Med*. 2007 Jan;57(1):2-7.

Witschey WR, Pilla JJ, Ferrari G, Koomalsingh K, Haris M, Hinmon R et al. Rotating frame spin lattice relaxation in a swine model of chronic, left ventricular myocardial infarction. *Magn Reson Med*. 2010 Nov;64(5):1453-1460.

Witschey WR, Zsido GA, Koomalsingh K, Kondo N, Minakawa M et al. In vivo chronic myocardial infarction characterization by spin locked cardiovascular magnetic resonance. *J Cardiovasc Magn Reson*. 2012 Jun 15;14:37.

Yla-Herttuala S, Rissanen TT, Vajanto I, Hartikainen J. Vascular endothelial growth factors: biology and current status of clinical applications in cardiovascular medicine. *J Am Coll Cardiol*. 2007 Mar 13;49(19):1015-1026.

Yla-Herttuala S, Bridges C, Katz MG and Korpisalo P. Angiogenic gene therapy in cardiovascular diseases: dream or vision? *Eur Heart J*. 2017 May 7;38(18):1365-1371.

Ylä-Herttuala E, Saraste A, Knuuti J, Liimatainen T, Ylä-Herttuala S. Molecular imaging to monitor left ventricular remodelling in heart failure. *Curr Cardiovasc Imaging Rep*. 2019 Apr;12:11.

Zamorano JL, Bax J, Knuuti J, Sechtem U, Lancellotti P, Badano L, 2015. *The ESC Textbook of Cardiovascular Imaging*. 2nd ed. Oxford University Press.

APPENDICES

ORIGINAL PUBLICATIONS (I-IV).

ORIGINAL PUBLICATIONS (I – IV)

I

Longitudinal rotating frame relaxation time measurements in infarcted mouse myocardium in vivo

Musthafa HS, Dragneva G, Lottonen L, Merentie M, Petrov L, Heikura T, Ylä-Herttuala E, Ylä-Herttuala S, Gröhn O, Liimatainen T

Magnetic Resonance in Medicine 69(5):1389-1395, 2013

II

Quantification of myocardial infarct area based on T_{RAFFn} relaxation time maps – comparison with cardiovascular magnetic resonance late gadolinium enhancement, $T_{1\rho}$ and T_2 in vivo

Ylä-Herttuala E, Laidinen S, Laakso H and Liimatainen T

Journal of Cardiovascular Magnetic Resonance 20(1):34, 2018

Yla-Herttuala *et al. Journal of Cardiovascular Magnetic Resonance* (2018) 20:34
https://doi.org/10.1186/s12968-018-0463-x

Journal of Cardiovascular
Magnetic Resonance

RESEARCH **Open Access**

Quantification of myocardial infarct area based on T_{RAFFn} relaxation time maps - comparison with cardiovascular magnetic resonance late gadolinium enhancement, $T_{1\rho}$ and T_2 in vivo

Elias Yla-Herttuala[1], Svetlana Laidinen[1], Hanne Laakso[1,2] and Timo Liimatainen[3,4*]

Abstract

Background: Two days after myocardial infarction (MI), the infarct consists mostly on necrotic tissue, and the myocardium is transformed through granulation tissue to scar in two weeks after the onset of ischemia in mice. In the current work, we determined and optimized cardiovascular magnetic resonance (CMR) methods for the detection of MI size during the scar formation without contrast agents in mice.

Methods: We characterized MI and remote areas with rotating frame relaxation time mapping including relaxation along fictitious field in nth rotating frame (RAFFn), $T_{1\rho}$ and T_2 relaxation time mappings at 1, 3, 7, and 21 days after MI. These results were compared to late gadolinium enhancement (LGE) and Sirius Red-stained histology sections, which were obtained at day 21 after MI.

Results: All relaxation time maps showed significant differences in relaxation time between the MI and remote area. Areas of increased signal intensities after gadolinium injection and areas with increased T_{RAFF2} relaxation time were highly correlated with the MI area determined from Sirius Red-stained histology sections (LGE: $R^2 = 0.92$, $P < 0.01$, T_{RAFF2}: $R^2 = 0.95$, $P < 0.001$). Infarct area determined based on $T_{1\rho}$ relaxation time correlated highly with Sirius Red histology sections ($R^2 = 0.97$, $P < 0.01$). The smallest overestimation of the LGE-defined MI area was obtained for T_{RAFF2} (5.6 ± 4.2%) while for $T_{1\rho}$ overestimation percentage was > 9% depending on $T_{1\rho}$ pulse power.

Conclusion: $T_{1\rho}$ and T_{RAFF2} relaxation time maps can be used to determine accurately MI area at various time points in the mouse heart. Determination of MI size based on T_{RAFF2} relaxation time maps could be performed without contrast agents, unlike LGE, and with lower specific absorption rate compared to on-resonance $T_{1\rho}$ relaxation time mapping.

Keywords: Cardiovascular magnetic resonance, Magnetic resonance imaging (MRI), Myocardial infarction (MI), Relaxation time, T_{RAFF2}, T_{RAFF4}, $T_{1\rho}$, T_2, LGE, Sirius red staining

---

* Correspondence: timo.liimatainen@oulu.fi
[3] Research Unit of Medical Imaging, Physics and Technology, University of Oulu, Oulu, Finland
[4] Department of Diagnostic Radiology, University Hospital of Oulu, P.O. Box 50, 90029 OYS Oulu, Finland
Full list of author information is available at the end of the article

Background

Cardiovascular diseases are the leading causes of death worldwide [1, 2]. Myocardial infarction (MI) is caused by a complete or partial blockage of the coronary artery, leading to inflammation, arrhythmia, and prolonged absence of perfusion [3–8]. The formation of fibrosis and collagen together with the loss of myocytes can lead to harmful remodeling of the myocardium and finally heart failure [3–7, 9]. Perfusion deficits cause cell death via necrosis and increases in extracellular space, which increases the tissue free water content and affects water-macromolecular interactions [10]. MI is a dynamic process since further loss of myocytes may occur, and collateral angiogenesis may decrease the infarct volume as a function of time [4, 6]. Scar tissue eventually replaces the damaged myocytes within 1–2 weeks after MI [4].

Several cardiovascular magnetic resonance (CMR) methods, for example T_2 and $T_{1\rho}$ relaxation time mappings and CMR spectroscopy, have been implemented to detect both acute and chronic MI [11–13]. Currently, the golden standard to detect chronic or irreversible injury using CMR is late gadolinium (Gd) enhancement (LGE). LGE creates a high contrast between normal myocardium and irreversible infarcted areas [11, 14, 15]. Contraindications for the use of Gd-based contrast agents are known Gd allergy and acute or chronic renal dysfunction [11, 16], which limit its clinical use.

Conventional transverse, or spin-spin, relaxation time, T_2, shows the difference between acute and chronic MI [15, 17]. Edema in the acute infarct phase increases free water content, significantly affecting heart function and T_2 relaxation time [12, 18]. Regions of acute MI can involve a mixture of tissue edema, hemorrhage, and inflammation, which leads to the underestimation of water movement in extracellular space and the overestimation of the infarct area in the T_2 relaxation time map [15, 19].

Rotating frame relaxation times are used to characterize the relaxation during radiofrequency (RF) pulses. This differs from conventional T_1 and T_2 relaxations where relaxation occurs during free precession. Longitudinal rotating frame relaxation time, $T_{1\rho}$, refers to relaxation along the RF field, which takes place typically during on-resonance RF irradiation. When RF irradiation is on-resonance and spins are locked along the RF field, the spins experience the RF field, instead of the main magnetic field. This leads to sensitivity of $T_{1\rho}$ to slow molecular motions with frequencies close to RF pulse frequency, which are typically in the range of 0.1 to 10 kHz in vivo. Comparatively, conventional T_1 is sensitive for Larmor frequency of the main magnetic field (B_0) which is typically in the range 10–500 MHz resembling high frequencies, i.e., fast molecular motions including the motion of free water. Increased $T_{1\rho}$ relaxation in MI has been associated with increased extracellular volume and alterations in proton exchange between water and macromolecules [11, 16]. Furthermore, $T_{1\rho}$ relaxation times are affected by macromolecule concentrations, viscosity, molecular weight and pH, since these factors change water mobility in tissue. Collectively, these factors affect molecular correlation times and therefore can explain $T_{1\rho}$ relaxation time increases in MI and other pathologies [16, 20]. Area with elevated $T_{1\rho}$ relaxation time show high correspondence with the MI area detected by LGE in mice [21] and in humans [11].

Specific absorption rate (SAR) often limits rotating frame relaxation measurements, especially in clinical settings, since high SAR may lead to tissue heating. One method to reduce SAR in rotating frame relaxation measurements is relaxation along a fictitious field (RAFF) in n^{th} rotating frame (RAFFn) [22–24]. RAFFn is produced by nested sine amplitude and cosine frequency modulated RF pulses operating in a sub-adiabatic regime and RF waveforms become more complicated when n increases [22, 23]. A fast, sub-adiabatic sweep of the effective RF field produces a fictitious field, which forms a part of the final effective RF field and magnetization precesses around this effective field [22]. When n increases in RAFFn, the tolerance for B_0 and radiofrequency field (B_1) inhomogeneities increases [23]. Due to lower flip angles with increasing n, the pulse bandwidth increases significantly [24]. Amplitude and frequency modulations, increase of bandwidth, decrease of flip angle together with remarkably lower (approximately 80%) SAR-values of RAFF4 and (approximately 30%) SAR-values of RAFF2 compared to continuous wave spin lock ($T_{1\rho}$) are clear advantages of RAFFn [22–24] and make RAFFn more suitable for clinical use than $T_{1\rho}$.

In the current study, we have optimized infarct sizing using T_{RAFF2} and T_{RAFF4} relaxation time mappings. The results were compared with $T_{1\rho}$ and T_2 relaxation time mappings, LGE and histology staining with Sirius Red.

Methods

Animal model

The left anterior descending artery (LAD) was ligated permanently in 10 female C57BL mice (20-24 g) as previously described [25]. Mice were anesthetized by 4% of isoflurane (Piramal Healthcare, Northumberland, UK), and anesthesia was maintained with 2.0% during the operation. The left side of mouse chest from sternum to Linea axillaris posterior was shaved and disinfected with 75% ethanol. An approximately 1.5 cm long transversal incision was made at the level of the fourth rib to left intercostal space. Through the incision and with help of a self-retaining retractor, the heart was exposed. The LAD was ligated with a 6.0 silk suture approximately at midway between its origin and the apex of the heart.

After the LAD ligation, the heart was placed back to its original location. The skin were sutured in layers with 5.0 nylon suture. After the surgery, 0.05–0.1 mg/kg buprenorphine (0.3 mg/ml Temgesic, RB Pharmaceuticals, Slough, UK) and 5 mg/kg carprofen (50 mg/ml, Rimadyl, Pfizer Oy Animal Health, Helsinki, Finland) for analgesia were injected subcutaneously and repeated at days 1 and 2 after the surgery. All surgical procedures were performed according to protocols approved by the Finnish Committee for the use and care of laboratory animals.

CMR

Mice underwent CMR at 1 (*n* = 10), 3 (*n* = 9), 7 (*n* = 5) and 21 (*n* = 5) days after LAD occlusion. All experiments were performed using a horizontal 9.4 T magnet (Varian Inc. Palo Alto, California, USA) with a gradient set with maximum gradient strength of 600 mT/m and controlled by a Bruker console (Bruker GmbH, Ettlingen, Germany). Quadrature volume transceiver with a coil diameter of 35 mm (Rapid Biomed GmbH, Ettlingen, Germany) was used for all CMR experiments. Mice were anesthetized for CMR with 4% isoflurane mixed in oxygen and nitrogen with ratio of 1:3. The level of isoflurane was decreased to 1% for the imaging. Mouse body temperature was kept close to 37 °C by circulating warm water tubes placed under the mouse. Electrocardiography (ECG) was measured from fore paws using needle electrodes and a pneumatic pillow placed under the mouse monitored respiration. Both signals were registered using Model 1025 monitoring and gating system (Small Animal Instruments Inc., Stony Brook, New York, USA) during the experiments. Both ECG and respiration signals were used to gate CMR experiments.

Multi-slice cine images covering the whole heart were taken using fast imaging with balanced steady state precession (FISP) readout sequence. The imaging parameters for cine images were FOV = 4 × 4 cm^2, slice thickness = 1 mm, matrix size = 192 × 192, TE = 1.9 ms, TR = 8.0 ms, scan TR = 99.0 ms, flip angle = 10° and number of frames 10–11 depending on mouse heart rate. Depending on the size of the heart, 8–10 slices were imaged.

The rotating frame preparation modules used to measure T_{RAFFn} consisted of RAFF2 or RAFF4 pulses (pulses RF power ($\gamma B_1/(2\pi)$) 1250 Hz and 648 Hz, respectively, duration 2.26 ms) which were applied in pulse trains of lengths 0, 9.1, 18.1 and 36.2 ms. Before the RAFFn pulse train, a delay with durations of 36.2, 27.15, 18.1 and 0 ms, respectively, was added to adjust imaging to occur at the same cardiac phase for weightings with different durations. An illustration of a rotating frame preparation module and readout sequence is shown in Fig. 1.

$T_{1\rho}$ preparation was performed using a rotating frame preparation module (Fig. 1) which contained adiabatic half passage (AHP) pulse (power 1250 Hz, duration 2.0 ms), continuous wave spin-lock-pulse with time-to-spin-lock (TSL) = 0.4, 9.4, 27.4 and 45.4 ms and AHP-back pulse (power 1250 Hz, duration 2.0 ms) [21]. Before $T_{1\rho}$ preparation a delay (45.4, 27.4, 9.4 and 0 ms, respectively to TSL) was added. $T_{1\rho}$ dispersion was measured by altering the spin lock power ($\gamma B_1/(2\pi)$) in a range of (400, 625 and 1250 Hz) and keeping AHP and AHP-back pulses the same.

T_2 measurements were conducted using Hahn double echo preparation containing an AHP excitation-pulse (power 1250 Hz, duration 3.0 ms), two Hyperbolic Secant (HS1)-pulses (power 1250 Hz, duration 4.5 ms) and a reversed AHP-pulse (power 1250 Hz, duration 3.0 ms) (Fig. 1). Between the pulses symmetric delays were used resulting in total TEs of 0.05, 2.3, 4.5, and 14.0 ms. Delays in front of T_2 preparation were 14.0, 4.5, 2.3 and 0.05 ms, respectively.

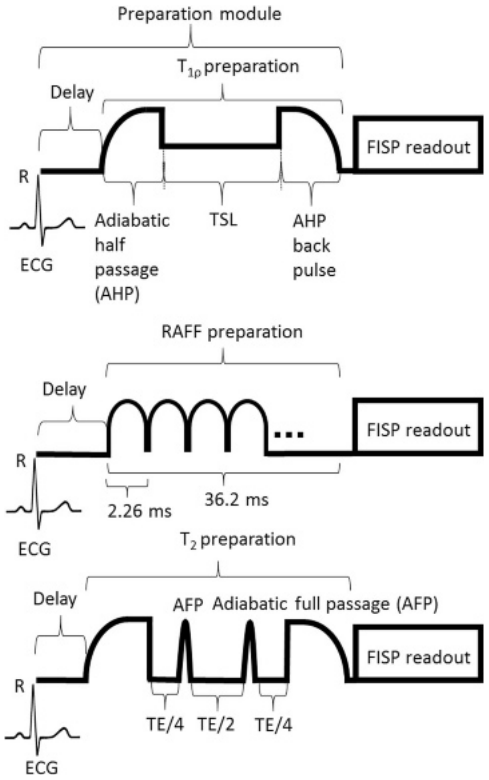

Fig. 1 An illustration of CMR pulse sequences consisting of the preparation module for different weightings and FISP readout. ECG, electrocardiogram; TE, echo time

B_1 was measured by applying a block pulse with power of 625 Hz. The B_1 block pulse was applied with pulse durations 0, 0.25, 0.5, 0.75, 1.0, 1.25, 1.5 and 1.75 ms [26].

All relaxation time maps and B_1 measurements were acquired using a FISP-readout sequence in a single short-axis slice at the mid-ventricular level. The following parameters: FOV = 4 × 4 cm^2, slice thickness = 1 mm, matrix size = 256 × 256 (for B_1 measurements, the matrix size was 128 × 128), TE = 1.9 ms, TR = 14.9 ms, and flip angle = 90° were used for the FISP-readout. A delay between weighting pulses depended on respiratory rate being at least 1460 ms.

At the last time point before sacrificing the mice, LGE images were acquired in the same slice as all other measurements using an inversion prepared pulse sequence with an inversion time of 300 ms, FISP-readout, FOV = 4 × 4 cm^2, slice thickness = 1 mm, matrix size = 256 × 192, TE = 2.0 ms, TR = 5.6 ms, scan TR = 3000.0 ms and flip angle = 90° [27]. The gadobutrol (Gadovist, Bayern Oy, Turku, Finland) intravenous injection volume was 5 ml/kg per mouse.

Only five mice survived to 21 days and were sacrificed for histology after imaging. For histology, the hearts were perfused through the left ventricle with phosphate buffered saline and then immersion fixed with 4% paraformaldehyde with sucrose in phosphate buffered solution for 4 h. After 4 h, the hearts were placed into 15% sucrose. Paraffin-embedded, 4 μm thick, cross-sections of the heart were stained with Sirius Red to determine the fibrotic areas of the infarcted myocardium. Histological sections were analyzed and photographed with microscopy (Nikon Eclipse, Ni-E, Tokyo, Japan).

Data analysis

All relaxation time maps were reconstructed from signal intensities with pixel-by-pixel analysis using Aedes software package (http://aedes.uef.fi/) in Matlab platform (Mathworks Inc. Natick, Massachusetts, USA). $T_{1\rho}$ and T_2 relaxation time maps were fitted using linear function for linearized data. T_{RAFF2} and T_{RAFF4} were fitted by using single mono-exponential decay function without taking into account the steady state formation. Regions of interest (ROIs) were manually traced with visual delineations of MI and remote areas based on relaxation time maps, cine images and images of Sirius Red-stained sections. End systolic volume (ESV), end diastolic volume (EDV), ejection fraction (EF), and cardiac output (CO) were defined based on endocardial border in cine images.

Infarct percentage analysis was done with midline length-based method with a function of $(L_{(infarct)}/\ L_{(circumference)})\bullet 100\%$, where L denotes measured length from either T_{RAFF2}, T_{RAFF4}, $T_{1\rho}$, T_2, LGE or Sirius Red-stained section [28]. Relative relaxation time difference (RRTD) values were calculated with function of $(T_{(infarct)}\ -T_{(remote)})/\ T_{(remote)}$, where T denotes either T_{RAFF2}, T_{RAFF4}, $T_{1\rho}$ or T_2 relaxation time.

Amount of overestimation (AOE) of infarct area relative to the LGE-defined MI area, as the gold standard, was calculated based on midline length-based method with a function of $((L_{(infarct)}\ -LGE_{(infarct)})/\ L_{(infarct)})\bullet 100\%$, where L denotes either T_{RAFF2}, T_{RAFF4}, $T_{1\rho}$ or T_2 relaxation time [29].

Statistics: All numerical values are given as mean ± standard deviation (SD). Two-way ANOVA with Bonferroni post hoc testing was applied to compare the spatial and temporal changes between the infarct and remote areas of myocardium, and the analyses were performed using GraphPad Prism software (GraphPad Software, La Jolla, California, USA). Two-way ANOVA with Bonferroni post hoc testing was performed to compare changes between RRTD values of different relaxation times. One-way ANOVA with Bonferroni post hoc testing for multiple comparisons were applied to compare time point differences between relaxation times and also the differences between time points of cardiac functions.

Results

Increased relaxation time constants were found in the MI areas after LAD ligation. Infarct areas obtained with relaxation time mappings were compared with infarct areas derived based on LGE-images, cine-images and Sirius Red-stained histological sections (Fig. 2).

T_{RAFF2} relaxation times were significantly higher in the infarct areas compared to remote areas ($P < 0.001$) (Fig. 3a). T_{RAFF2} relaxation times in infarct area increased significantly up to 7 days and remained elevated until day 21 after the LAD ligation ($P < 0.05$, $P < 0.05$, respectively) (Fig. 3a). T_{RAFF4} relaxation time in the infarct area was significantly elevated at all time points compared to the remote area ($P < 0.001$, Fig. 3b). The remaining relaxation times ($T_{1\rho1250}$, $T_{1\rho625}$, $T_{1\rho400}$ and T_2) were significantly elevated in the infarct area compared to remote areas ($P < 0.001$, respectively), and there were significant differences, except in $T_{1\rho1250}$, between time points ($P < 0.05$, respectively, Fig. 3c-f). Specifically, $T_{1\rho625}$ relaxation times increased significantly in the infarct area at 7 days after the LAD ligation ($P < 0.01$) and remained elevated until day 21 ($P < 0.001$, Fig. 3e). There was a significant increase in $T_{1\rho625}$ relaxation times in infarct area at days 7 and 21 compared to day 1 after the LAD occlusion ($P < 0.05$, $P < 0.05$ respectively), and it also increased significantly from day 3 to day 21 ($P < 0.05$, Fig. 3e). Additionally, the trend between infarct and remote areas in $T_{1\rho625}$, $T_{1\rho400}$ and T_2 relaxation times differed significantly ($P < 0.05$, respectively) from each other (Fig. 3c, e, f). A decrease in T_2 relaxation time was detected from day 3 to day 21 after the LAD ligation ($P < 0.05$, Fig. 3c).

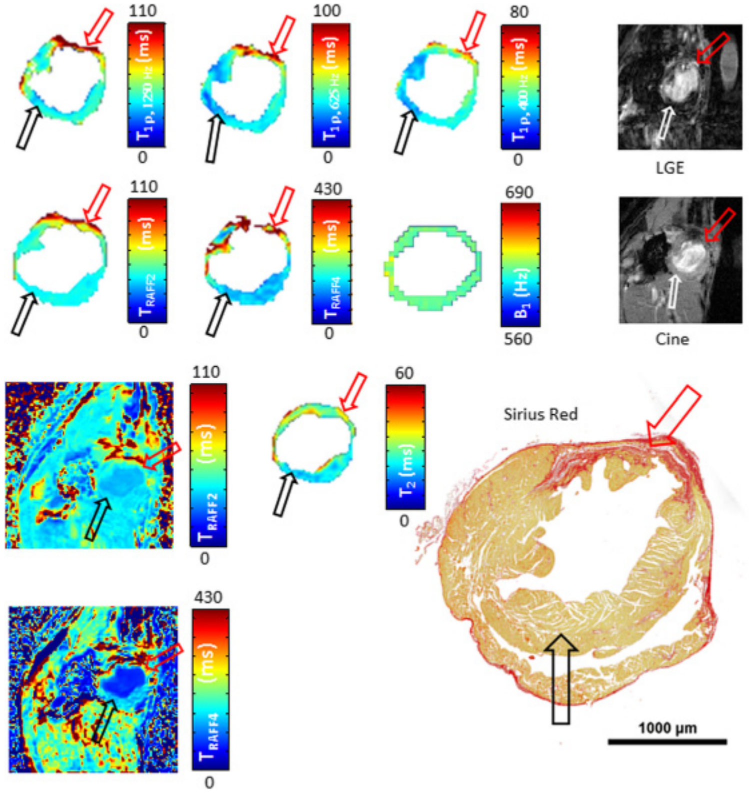

Fig. 2 Relaxation time maps, late gadolinium enhancement (LGE), cine and a corresponding histology image with Sirius Red-stained section from infarcted mouse heart at the last (21 day) time point after left anterior descending (LAD) myocardial infarction (MI). Red arrows indicate the infarct area and black/white arrows show the remote control area. B_1 homogeneity was verified to be nominal ±10% Hz in the area of the whole myocardium

There were no significant changes in the relaxation times in the remote areas between the imaging time points ($P > 0.05$, Fig. 3).

RRTD provided a measure of differences in relaxation time values between infarct and remote areas for the relaxation measurements (Table 1). RRTD values of T_{RAFF4} differed significantly from other relaxation time methods at several different time points (Table 1). There were significant differences in RRTD values of some of the $T_{1\rho}$ relaxation times when comparing RRTD values at day 1 (Table 1).

AOE values were determined for all relaxation times (Fig. 4a). AOE was lowest for T_{RAFF2} indicating that area of increased T_{RAFF2} is most similar to LGE-measured infarct area (Fig. 4a).

Infarct sizes were calculated also as a ratio between the arc of infarct and the circumference of the whole myocardium from relaxation time maps and LGE-images (Figs. 4b and 5). These infarct sizes were correlated with the ones measured based on Sirius Red-stained histology-images (Fig. 5). The highest Spearman correlations were obtained with $T_{1\rho}$ ($R^2 = 0.97$, $P < 0.01$). Infarct sizes from T_{RAFF2} ($R^2 = 0.93$, $P < 0.001$) and T_{RAFF4} ($R^2 = 0.94$, $P < 0.001$) showed a high correlation as well as LGE ($R^2 = 0.92$, $P < 0.01$) with infarct size from Sirius Red-stained sections (Fig. 5). The infarct fraction given as a percentage at early time points obtained from T_2 relaxation time map was largest but decreased to similar percentages as obtained from the other relaxation time maps at day 21 (Fig. 4b).

Dispersion of $T_{1\rho}$ relaxation times ($\Delta T_{1\rho}$) was calculated by subtracting $T_{1\rho}$ relaxation times measured with different spin lock powers (Fig. 6). Significant differences between different $T_{1\rho}$ relaxation times in infarct and remote areas were not found, and the difference in both areas remained almost constant between the time points (Fig. 6).

Parameters of cardiac function indicate that MI has developed as a function of time (Table 2). Specifically EF decreased as a function of time and, three weeks after

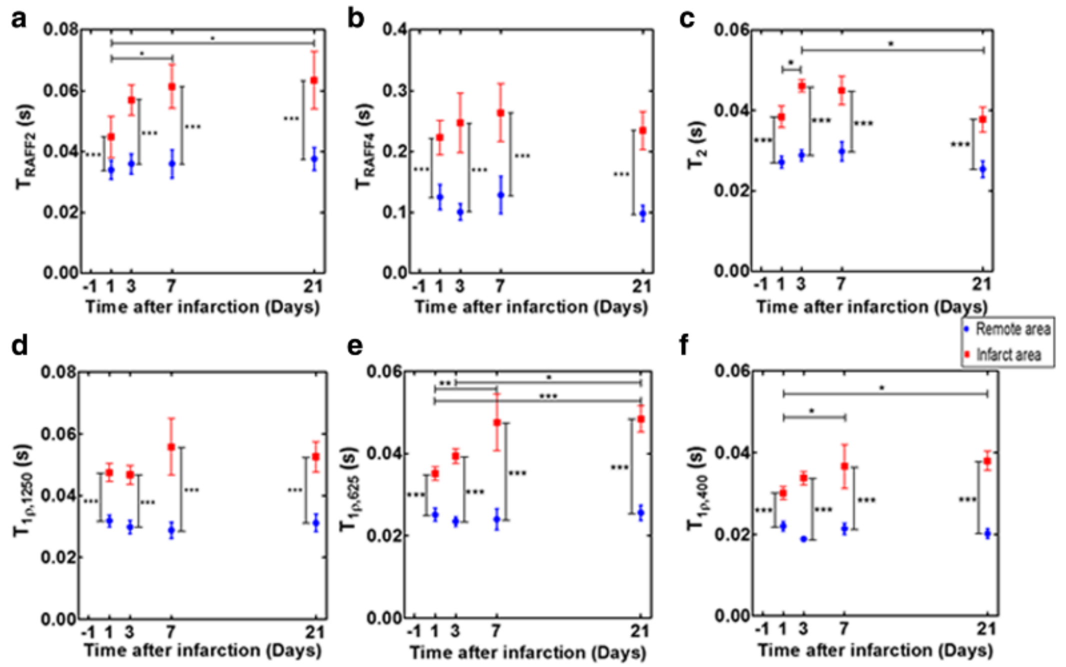

Fig. 3 Different relaxation times (mean ± SD). T_{RAFF2} (**a**), T_{RAFF4} (**b**), T_2 (**c**), $T_{1\rho1250}$ (**d**), $T_{1\rho625}$ (**e**) and $T_{1\rho400}$ (**f**) were calculated in infarct and remote areas at different time points after the LAD ligation. Blue circles indicate remote and red squares infarct area. (*$P < 0.05$, **$P < 0.01$ and ***$P < 0.001$, Two-way ANOVA with Bonferroni post hoc test)

MI, EF had decreased to 0.35 (Table 2). Increased cardiac output between days 1 and 7 was found, although it was assumed to decrease (Table 2).

Discussion

In this murine study, relaxation times were measured in infarct and remote areas at several time points after MI. Infarct size was measured based on different relaxation times, the results were compared to infarct sizes derived from CMR LGE-image and Sirius Red-stained histology sections. MI size from $T_{1\rho}$, T_{RAFF2} and T_{RAFF4} relaxation time maps showed a high correlation with MI size determined based on Sirius Red-stained histology sections.

T_{RAFF2} relaxation times in infarct areas increased significantly from day 1 to day 21 after the LAD ligation and the RRTD values increased as a function of time. Differences between infarct and remote areas in T_{RAFF2} relaxation times were statistically significant. Low AOE-value obtained with T_{RAFF2} relaxation time demonstrate that elevated T_{RAFF2} denotes permanently damaged area. These findings together with a high

Table 1 Relative relaxation time difference (RRTD) values formed by infarct and remote area relaxation times presented as mean ± SD

Relaxation time constant	Day 1	Day 3	Day 7	Day 21
$T_{1\rho1250}$	0.49 ± 0.11$^{\square}$	0.60 ± 0.29$^{\square\square\square}$	0.91 ± 0.42*	0.69 ± 0.16$^{\square\square}$
$T_{1\rho625}$	0.41 ± 0.09$^{\square\square}$	0.70 ± 0.27$^{\square\square\square}$	0.99 ± 0.44**	0.90 ± 0.24*
$T_{1\rho400}$	0.37 ± 0.09$^{\square\square}$	0.79 ± 0.21**,$^{\square\square}$	0.69 ± 0.33$^{\square}$	0.90 ± 0.27**
T_2	0.41 ± 0.11$^{\square\square}$	0.61 ± 0.19$^{\square\square\square}$	0.51 ± 0.11$^{\square\square}$	0.50 ± 0.19$^{\square\square\square}$
T_{RAFF2}	0.41 ± 0.12$^{\square\square}$	0.62 ± 0.43$^{\square\square\square}$	0.73 ± 0.22	0.66 ± 0.21$^{\square\square}$
T_{RAFF4}	0.90 ± 0.45	1.36 ± 0.62	1.22 ± 0.59	1.39 ± 0.37

Significance of differences in RRTD values were calculated by Two-way ANOVA with Bonferroni post hoc test ($^{\square}$=P<0.05, $^{\square\square}$=P<0.01, $^{\square\square\square}$=P<0.001 for difference to T_{RAFF4} at that specific time point) and One-way ANOVA with Bonferroni post hoc test (*=P<0.05, **=P<0.01 for difference to day 1)

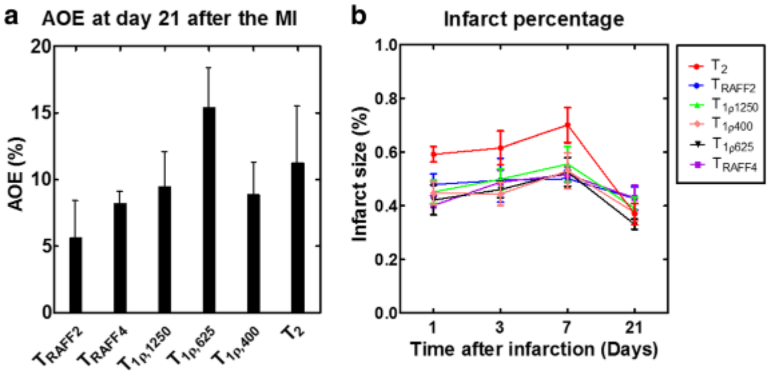

Fig. 4 Amount of overestimation (AOE) with regard to the LGE-defined MI area based on the relaxation time maps at 21 days after infarct (**a**) and infarct percentages at every time point based on the relaxation time maps (**b**)

correlation between T_{RAFF2} and histology derived infarct size, demonstrate that T_{RAFF2} relaxation time detects MI area with high accuracy. Previously, T_{RAFF2} relaxation time has been measured in a rat malignant glioma model where T_{RAFF2} showed a high correlation with decreased cell density in tumors [30]. Furthermore, cell density decreases in the infarct area as the tissue is replaced by fibrotic tissue, which leads to an increase of extracellular space [10]. Most likely, increase of T_{RAFF2} in both of these cases is caused by increases in extracellular space and, therefore, an increase in free water content. This suggest that fibrotic tissue can be differentiated healthy tissue using the T_{RAFF2} map. This is important since fibrosis detection also plays a central role in MI detection. Our results demonstrate the potential of T_{RAFF2} mapping to determine and accurately assess the MI area in both acute and chronic phase of the disease. Another explanation for elevated T_{RAFF2} is altered ^{1}H chemical exchange between water and macromolecules due to changes induced by infarct in exchange of populations,

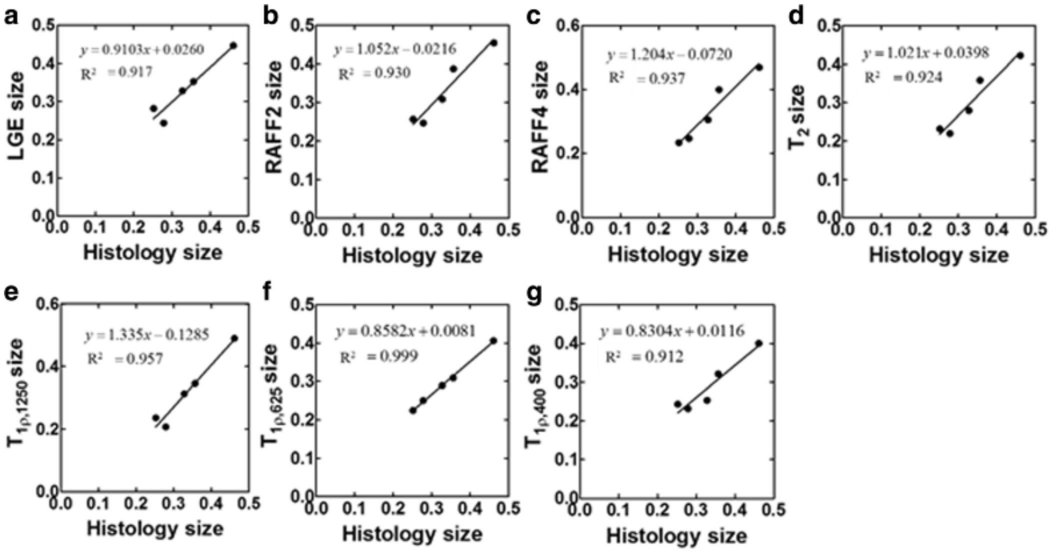

Fig. 5 Linear correlation from the ratios between the arc of infarct and the circumferences of the whole myocardium determined from LGE-image (**a**), T_{RAFF2} (**b**), T_{RAFF4} (**c**), T_2 (**d**), $T_{1\rho1250}$ (**e**), $T_{1\rho625}$ (**f**), $T_{1\rho400}$ (**g**) and Sirius Red-stained histology sections. Formulas of linear relationships are shown next to correlation line

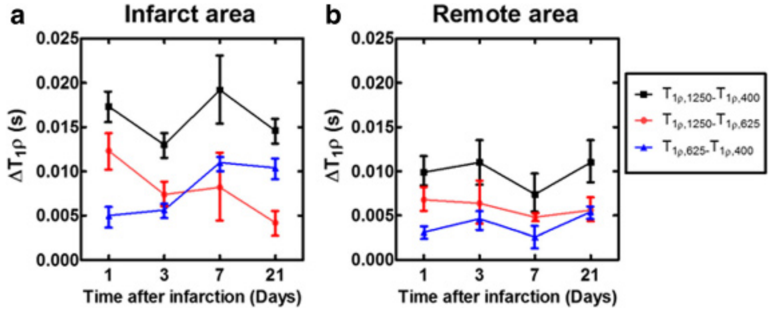

Fig. 6 Dispersion of $T_{1\rho}$ relaxation time in infarct area (**a**) and in remote area (**b**). Red color shows subtraction between $T_{1\rho1250}$ - $T_{1\rho625}$, black color shows subtraction between $T_{1\rho1250}$ - $T_{1\rho400}$ and blue color shows subtraction between $T_{1\rho625}$ - $T_{1\rho400}$

exchange rates, or chemical shifts between exchanging sites [30]. The extracellular pH may also change in MI, which may induce alterations to exchange rates [30].

Our results showed that T_{RAFF4} relaxation times were elevated at all time points in the MI area and the difference between infarct and remote areas in T_{RAFF4} was significant. Our findings suggest that T_{RAFF4} relaxation time mapping can be applied to detect chronic MI since infarct size derived from T_{RAFF4} map correlated highly ($R^2 = 0.94$, $P < 0.001$) with histology derived infarct area together with small AOE-value.

$T_{1\rho1250}$ relaxation time determined at infarct area was significantly higher when compared to remote areas of the myocardium. In addition, infarct size derived from $T_{1\rho1250}$ map correlated with infarct size from Sirius Red sections ($R^2 = 0.96$, $P < 0.01$) and its AOE-value was close to zero. The largest RRTD between infarct and remote area was found with $T_{1\rho625}$. Infarct size based on $T_{1\rho625}$ and $T_{1\rho400}$ relaxation time maps showed high correlations ($R^2 = 0.99$, $P < 0.001$, $R^2 = 0.96$, $P < 0.05$, respectively) with Sirius Red staining but $T_{1\rho625}$ showed the largest AOE-value (15.4 ± 6.1%). $T_{1\rho}$ relaxation times have previously been known to be two times longer in scar tissue than in normal myocardium in porcine heart [16]. However, the origin of $T_{1\rho}$ increase at MI is still unclear. Most likely it is due to increased fibrosis content, cellularity, or ^1H chemical exchange [11, 31]. In addition, there is a suggestion that leaking protein material from sarcolemma into extracellular space minimizes effects of proteins on water molecules or macromolecules in acute MI in patients and swine [10, 17]. Selective sensitivity to correlation times near to $1/(\gamma B_1)$ is an advantage of $T_{1\rho}$ relaxation time [21].

In a previous study, the $T_{1\rho}$ relaxation time with different spin-lock powers increased significantly 7 days after MI compared to the remote area [21] and $T_{1\rho}$ relaxation times elevated almost monotonically during 2 weeks after MI [21]. These findings were explained by granulation and scar tissue formation [11, 21]. Similar increase was detected in this study with $T_{1\rho}$s, T_{RAFF2}, and T_{RAFF4}.

T_2 relaxation times increased significantly from day 1 to day 3 in infarct area and T_2 relaxation times in infarct area were significantly higher than T_2 relaxation times in remote area. These results are in line with previous findings showing that damaged area in myocardium is reversible in acute phase of MI [12, 18, 32]. It has previously been shown that T_2 relaxation time overestimates the size of acute MI compared to chronic MI, since the inflammation and edema have resolved from the chronic MI [18]. Similar findings were observed in this study since infarct percentages based on T_2 maps were higher as compared to percentages based on the other relaxation times at early time points. Therefore, increased T_2 relaxation time shows the area of edema rather than the

Table 2 Values of cardiac function parameters which are presented as mean ± SD

Cardiac function parameters	Day 1	Day 3	Day 7	Day 21
End diastolic volume (mm^3)	48.4 ± 20.7	47.1 ± 24.6	72.9 ± 26.7	90.3 ± 30.2*,$^{\square}$
End systolic volume (mm^3)	22.7 ± 13.0	21.9 ± 13.8	39.9 ± 17.6	58.0 ± 18.5**,$^{\square\square}$
Ejection Fraction (%)	0.55 ± 0.12	0.56 ± 0.09	0.46 ± 0.09	0.35 ± 0.04**,$^{\square\square}$
Cardiac output (mm^3)	14,570 ± 3680	15,140 ± 5770	20,280 ± 8130*	19,800 ± 8680
Heart rate (bpm)	580.2 ± 82.5	599.0 ± 64.9	615.5 ± 48.0	632.0 ± 52.3

Differences between time points of different cardiac measures were analyzed by One-way ANOVA with Bonferroni post hoc test (*=P<0.05 for difference to day 1) ($^{\square}$=P<0.05, $^{\square\square}$=P<0.01 for difference to day 3) actual size of MI [18]. T_2 relaxation times did not differ between day 1 and day 21, which suggests that part of the damage in myocardium was reversible without the scar formation. In a previous study, T_2 relaxation times were significantly higher in acute MI area compared to chronic MI area [12].

The MI areas defined based on CMR images were in good agreement with the areas determined with Sirius Red-stained histology. To our knowledge, elevated relaxation times, at least $T_{1\rho}$ relaxation times, at 21 days after MI are due to fibrosis and scar tissue formation. The locations of fibrotic areas in Sirius Red-stained sections and the elevated relaxation times on relaxation time maps agreed well. Notable, our results are based on quantitative relaxation times instead of weighted images. These results also suggest that especially T_{RAFF2}, T_{RAFF4} and $T_{1\rho}$ relaxation time mappings may be useful for broad range of clinical applications where myocardial tissue characterization is needed, for example in myocarditis, various size and locations of scars, sarcoidosis and hypertrophy. Operating at lower main magnetic field strengths will have some impact on rotating frame relaxation times; however, the main influence is the strength of the spin-lock power [33]. Water molecules with correlation times close to $1/(\gamma B_1)$ contribute to rotating frame contrasts [33]. Adaption of rotating frame measurements to MI characterization at clinics needs further study since we demonstrated advantages of relaxation times only in MI mouse model where one artery (LAD) was occluded.

MI area was detectable in all relaxation time maps and it was the most visible at day 21. At the first time points, the MI area was larger than at the later time points most likely due to inflammation surrounding the infarction area. In a mouse model, MI area consists of over 90% of necrotic tissue only two days after LAD ligation and the necrotic tissue is transformed into granulation tissue one week after MI and into scar two weeks after the LAD ligation [5].

The LAD ligations were successfully performed since our results show a clear visibility of infarct in Sirius Red-stained sections and decreased EF values as a function of time. Additionally, EDV and ESV tend to increase post MI due to changes in physiology of the myocardium. Changes in physiology with decreased perfusion inside the myocardium lead also to a decrease of EF as a function of time. Our EF values agreed with EF values reported in the literature [34, 35]. Increased EDV and ESV at day 21 compared to day 1 after MI resulted in an increased stroke volume (23%) which together with increased heart rate (8%) lead to increased cardiac output. The ventricular dilation after MI is typical [34, 35] and was also observed in our cine images. However, increased stroke volume after MI is rare [34, 35]. Differences in anesthesia level or mice increased tolerance to anesthetic during subsequent CMR exams might be the reasons for the increased heart rates.

Conclusions

All relaxation time maps showed high contrast between infarct and remote areas. $T_{1\rho}$, T_{RAFF2} and T_{RAFF4} relaxation time maps correlated significantly with the infarct size determined by histology. As a conclusion, T_{RAFF2} and T_{RAFF4} relaxation time maps can be used to accurately determine infarct size in mouse myocardial infarct without the use of contrast agent with clinically tolerable specific absorption rates.

Abbreviations

AHP: Adiabatic half passage; AOE: Amount of overestimation; CMR: Cardiovascular magnetic resonance; CO: Cardiac output; ECG: Electrocardiogram; EDV: End-diastolic volume; EF: Ejection fraction; ESV: End-systolic volume; Gd: Gadolinium; LAD: Left anterior descending coronary artery; LGE: Late gadolinium enhancement; MI: Myocardial infarction; RAFF: Relaxation along a fictitious field; RF: Radiofrequency; ROI: Region of interest; RRTD: Relative relaxation time difference; SAR: Specific absorption rate; TSL: Time to spin lock

Acknowledgements

The authors thank Maarit Pulkkinen for technical assistance. The authors thank Nicholas Downes for checking the language of the manuscript.

Funding

Sigrid Juselius foundation and University of Eastern Finland Doctoral Programme of Molecular Medicine.

Availability of data and materials

The datasets used and/or analyzed during the current study are available from the corresponding author on reasonable request.

Authors' contributions

Each author contributed significantly to the submitted work: EYH was involved in the design of the study, performed CMR measurements, performed data analysis, interpreted the data and drafted the manuscript. SL did LAD surgeries, histology and revised the manuscript. HL helped to design CMR measurements, helped in CMR measurements and revised the manuscript. TL designed the study and revised the manuscript. All authors read and approved the final manuscript.

Ethics approval and consent to participate

All surgical procedures were performed according to protocols approved by the Finnish Committee for the use and care of laboratory animals.

Competing interests

The authors declare that they have no competing interests.

Publisher's Note

Author details

[1]A.I. Virtanen Institute for Molecular Sciences, University of Eastern Finland, Kuopio, Finland. [2]Center for Magnetic Resonance Research, Minneapolis, MN, USA. [3]Research Unit of Medical Imaging, Physics and Technology, University of Oulu, Oulu, Finland. [4]Department of Diagnostic Radiology, University Hospital of Oulu, P.O. Box 50, 90029 OYS Oulu, Finland.

Received: 12 September 2017 Accepted: 24 May 2018

References

1. Ylä-Herttuala S, Bridges C, Katz MG, Korpisalo P. Angiogennic gene therapy in cardiovascular diseases: dream or vision? Eur Heart J. 2017;38:1365–71.
2. Ylä-Herttuala S, Baker AH. Cardiovascular gene therapy: past, present, and future. Mol Ther. 2017;25:1095–106.
3. Blankesteijn WM, Creemers E, Lutgens E, Cleutjens JP, Daemen MJ, Smits JF. Dynamics of cardiac wound healing following myocardial infarction: observations in genetically altered mice. Acta Physiol Scand. 2001;173:75–82.
4. Ertl G, Frantz S. Healing after myocardial infarction. Cardiovasc Res. 2005;66:22–32.
5. Virag JI, Murry CE. Myofibroblast and endothelial cell proliferation during murine myocardial infarct repair. Am J Pathol. 2003;163:2433–40.
6. Holmes JW, Yamashita H, Waldman LK, Covell JW. Scar remodeling and transmural deformation after infarction in the pig. Circulation. 1994;90:411–20.
7. McKay RG, Pfeffer MA, Pasternak RC, Markis JE, Come PC, Nakao S, Alderman JD, Ferguson JJ, Safian RD, Grossman W. Left ventricular remodeling after myocardial infarction: a corollary to infarct expansion. Circulation. 1986;74:693–702.
8. Frangogiannis NG, Smith CW, Entman ML. The inflammatory response in myocardial infarction. Cardiovasc Res. 2002;53:31–47.
9. Gaudron P, Kugler I, Hu K, Bauer W, Eilles C, Ertl G. Time course of cardiac structural, functional and electrical changes in asymptomatic patients after myocardial infarction: their inter-relation and prognostic impact. J Am Coll Cardiol. 2001;38:33–40.
10. Muthupillai R, Flamm SD, Wilson JM, Pettigrew RI, Dixon WT. Acute myocardial infarction: tissue characterization with $T_{1\rho}$-weighted MR imaging - initial experience. Radiology. 2004;232:606–10.
11. van Oorschot JWM, El Aidi H, Jansen of Lorkeers SJ, Gho JM, Froeling M, Visser F, Chamuleau SA, Doevendans PA, Luijten PR, Lainer T, Zwanenburg JJ. Endogenous assessment of chronic myocardial infarction with $T_{1\rho}$-mapping in patients. J Cardiovasc Magn Reson. 2014;16:104–12.
12. Verhaert D, Thavendiranathan P, Giri S, Mihai G, Rajagopalan S, Simonetti OP, Raman SV. Direct T_2 quantification of myocardial edema in acute ischemic injury. JACC Cardiovasc Imaging. 2011;4:269–78.
13. de Roos A, van der Wall EE. Evaluation of ischemic heart disease by magnetic resonance imaging and spectroscopy. Radiol Clin N Am. 1994; 32:581–92.
14. Huber S, Muthupillai R, Lambert B, Pereyra M, Napoli A, Flamm SD. Tissue characterization of myocardial infarction using $T_{1\rho}$: influence of contrast dose and time of imaging after contrast administration. J Magn Reson Imaging. 2006;24:1040–6.
15. Abdel-Aty H, Zagrosek A, Schultz-Menger J, Taylor AJ, Messroghli D, Kumar A, Gross M, Dietz T, Friedrich MG. Delayed enhancement and T_2-weighted cardiovascular magnetic resonance imaging differentiate acute from chronic myocardial infarction. Circulation. 2004;109:2411–6.
16. Witschey WR, Zsido GA, Koomalsingh K, Kondo N, Minakawa M, Shuto T, McGarvey JR, Levack MM, Contijoch F, Pilla JJ, Gorman JH 3rd, Gorman RC. In vivo chronic myocardial infarction characterization by spin locked cardiovascular magnetic resonance. J Cardiovasc Magn Reson. 2012;14:37.
17. Witschey WR, Pilla JJ, Ferrari G, Koomalsingh K, Haris M, Himmon R, Zsido G, Gorman JH 3rd, Gorman RC, Reddy R. Rotating frame spin lattice relaxation in a swine model of chronic, left ventricular myocardial infarction. Magn Reson Med. 2010;64:1453–60.
18. Abdel-Aty H, Simonetti O, Friedrich MG. T_2-weighted cardiovascular magnetic resonance imaging. J Magn Reson Imaging. 2017;26:452–9.
19. Reimer KA, Jennings RB. The changing anatomic reference base of evolving myocardial infarction. Underestimation of myocardial collateral blood flow and overestimation of experimental anatomic infarct size due to tissue edema, hemorrhage and acute inflammation. Circulation. 1979;60:866–76.
20. Hakumäki JM, Gröhn OH, Tyynelä K, Valonen P, Ylä-Herttuala S, Kauppinen RA. Early gene therapy-induced apoptotic response in BT4C gliomas by magnetic resonance relaxation contrast T_1 in the rotating frame. Cancer Gene Ther. 2002;9:338–45.
21. Mustafa HSN, Dragneva G, Lottonen L, Merentie M, Petrov L, Heikura T, Ylä-Herttuala E, Ylä-Herttuala S, Gröhn O, Liimatainen T. Longitudinal rotating frame relaxation time measurements in infarcted mouse myocardium in vivo. Magn Reson Med. 2013;69:1389–95.
22. Liimatainen T, Sorce DJ, O'Donnell R, Michaeli S. MRI contrasts from relaxation along a fictitious field (RAFF). Magn Reson Med. 2010;64:983–94.
23. Liimatainen T, Hakkarainen H, Mangia S, Huttunen JM, Storino C, Idiyatullin D, Sorce D, Garwood M, Michaeli S. MRI contrasts in high rank rotating frames. Magn Reson Med. 2015;73:254–62.
24. Hakkarainen H, Sierra A, Mangia S, Garwood M, Michaeli S, Gröhn O, Liimatainen T. MRI relaxation in the presence of fictitious fields correlates with myelin content in normal rat brain. Magn Reson Med. 2016;75:161–8.
25. Gao E, Lei YH, Shang X, Huang ZM, Zuo L, Boucher M, Fan Q, Chuprun JK, Ma XL, Koch WJ. A novel and efficient model of coronary artery ligation and myocardial infarction in the mouse. Circ Res. 2010;107:1445–53.
26. Vaughan JT, Garwood M, Collins CM, Liu W, DelaBarre L, Adriany G, Andersen P, Merkle H, Goebel R, Smith MB, Urgurbil K. 7 T vs. 4 T: RF power, homogeneity, and signal-to-noise comparison in head images. Magn Reson Med. 2001;46:24–30.
27. Amano Y, Tachi M, Kumita S. Three-dimensional look-locker MRI for evaluation of postcontrast myocardial and blood T_1 values: comparison with two-dimensional look-locker and late gadolinium enhancement MRI. Acta Radiol. 2013;54:8–13.
28. Park C, Park EH, Chang K, Hong KS. Sector-based assessment of infarct size on late-gadolinium-enhancement MRI in a mouse model of acute myocardial infarction. Int Heart J. 2016;57:736–41.
29. Ugander M, Bagi PS, Oki AJ, Chen B, Hsu LY, Aletras AH, Shah S, Greiser A, Kellman P, Arai AE. Myocardial edema as detected by pre-contrast T1 andT2 CMR delineates area at risk associated with acute myocardial infarction. JACC Cardiovasc Imaging. 2012;5:595–603.
30. Liimatainen T, Sierra A, Hanson T, Sorce DJ, Ylä-Herttuala S, Garwood M, Michaeli S, Gröhn O. Glioma cell density in a rat gene therapy model gauged by water relaxation rate along a fictitious magnetic field. Magn Reson Med. 2012;67:269–77.
31. Kettunen MI, Sierra A, Närväinen MJ, Valonen PK, Ylä-Herttuala S, Kauppinen RA, Gröhn OH. Low spin-lock field T_1 relaxation in the rotating frame as a sensitive MR imaging marker for gene therapy treatment response in rat glioma. Radiology. 2007;243:796–803.
32. Bönner F, Jacoby C, Temme S, Borg N, Ding Z, Schrader J, Flögel U. Multifunctional MR monitoring of the healing process after myocardial infarction. Basic Res Cardiol. 2014;109:430.
33. Mäkelä HI, De Vita E, Gröhn OH, Kettunen MI, Kayec M, Lythgoe M, Garwood M, Ordidge R, Kauppinen RA. B0 dependence of the on-resonance longitudinal relaxation time in the rotating frame (T1rho) in protein phantoms and rat brain in vivo. Magn Reson Med. 2004;51:4–8.
34. Haberkorn SM, Jacoby C, Ding Z, Keul P, Bönner F, Polzin A, Levkau B, Schrader J, Kelm M, Flögel U. Cardiocascular magnetic resonance relaxometry predicts regional functional outcome after experimental myocardial infarction. Circ Cardiovasc Imaging. 2017;10:e006025.
35. Nahrendorf M, Hiller KH, Hu K, Ertl G, Haase A, Bauer WR. Cardiac magnetic resonance imaging in small animal models of human heart failure. Med Image Anal. 2003;7:369–75.

III

Downregulation of VEGFR3 signaling alters cardiac lymphatic vessel organization and leads to a higher mortality after acute myocardial infarction

Vuorio T, Ylä-Herttuala E, Laakkonen JP, Laidinen S, Liimatainen T, Ylä-Herttuala S

Scientific Reports 8:16709, 2018

www.nature.com/scientificreports

SCIENTIFIC REPORTS

Received: 11 December 2017
Accepted: 26 October 2018

Downregulation of VEGFR3 signaling alters cardiac lymphatic vessel organization and leads to a higher mortality after acute myocardial infarction

Taina Vuorio[1], Elias Ylä-Herttuala[1], Johanna P. Laakkonen[1], Svetlana Laidinen[1], Timo Liimatainen[2,4] & Seppo Ylä-Herttuala[1,3]

Heart has a wide lymphatic network but the importance of cardiac lymphatic system in heart diseases has remained unclear. Vascular Endothelial Growth Factor Receptor 3 (VEGFR3) is a key molecule in the development and maintenance of cardiac lymphatic vessels. Here we characterized the role of VEGFR3 in healthy hearts and after myocardial infarction (MI) by using sVEGFR3 transgenic mice expressing a soluble decoy VEGFR3 under K14 promoter and Chy mice which have an inactivating mutation in the VEGFR3 gene. Cardiac lymphatic vessels were significantly dilated in the healthy hearts of sVEGFR3 mice when compared to controls. Lymphatic vessels formed large sheet-like structures in Chy mice. Attenuated VEGFR3 signaling led to a more severe MI predisposing to a significantly higher mortality in sVEGFR3 mice than in control mice. sVEGFR3 mice displayed intramyocardial hemorrhages in the infarcted area indicating hyperpermeability of the vasculature. Furthermore, novel MRI methods TRAFF2 and TRAFF4 and histological analysis revealed a modified structure of the fibrotic infarcted area in sVEGFR3 mice. In conclusion, the downregulation of VEGFR3 signaling modifies the structure of cardiac lymphatic network and causes vascular leakiness and increased mortality after MI.

Lymphatic vessels were long considered as passive drainage conduits of extracellular fluid but their role has been extended since the mechanisms of their development and function in several pathophysiological processes have been identified[1]. Lymphatic system regulates many processes involved in cardiac physiology and pathology, such as inflammatory reactions[2], tissue fluid balance[3], reverse cholesterol transport[4] and atherosclerosis[5,6] which can eventually change heart function. Therefore, the role of lymphatic vessels in myocardial infarction (MI) and other heart conditions can be more significant than previously anticipated[7,8].

The development of mouse cardiac lymphatic vessels starts at E12-14 when lymphatic endothelial cells (LECs) derived mainly from the common cardinal vein transmigrate to the dorsal and ventral surfaces of the heart and start to form lymphatic tubules and subsequently lymphatic capillary plexus[9,10]. In adults, capillary size lymphatic vessels cover the myocardium and subendocardium and also the atrioventricular and semilunar valves in most mammalian species[11,12]. It has been shown that cardiac lymph flow begins from small endocardial lymphatics and continues through myocardium into subepicardial capillaries that converge into larger collecting lymphatic vessels. Finally, cardiac lymph passes through the mediastinal lymph nodes into the thoracic duct[13].

Only a few studies have focused on the function of lymphatic vessels in regulating cardiac physiology or their role in cardiac pathologies. The effect of cardiac lymph flow impairment has been studied by blocking ventricular and mediastinal lymphatic ducts in large animals (reviewed by Cui[14]). In these studies, the obstruction of lymphatic flow led to subepicardial edema, depressed left ventricle (LV) contractile function and hemorrhages.

[1]A.I. Virtanen Institute for Molecular Sciences, University of Eastern Finland, P.O. Box 1627, FI-70211, Kuopio, Finland. [2]Research Unit of Medical Imaging, Physics and Technology, University of Oulu, Oulu, Finland. [3]Heart Center and Gene Therapy Unit, Kuopio University Hospital, P.O. Box 1777, FI-70211, Kuopio, Finland. [4]Department of Diagnostic Radiology, University Hospital of Oulu, P.O. Box 50, FI-90029 OYS, Oulu, Finland. Correspondence and requests for materials should be addressed to S.Y.-H. (email: Seppo.Ylaherttuala@uef.fi)

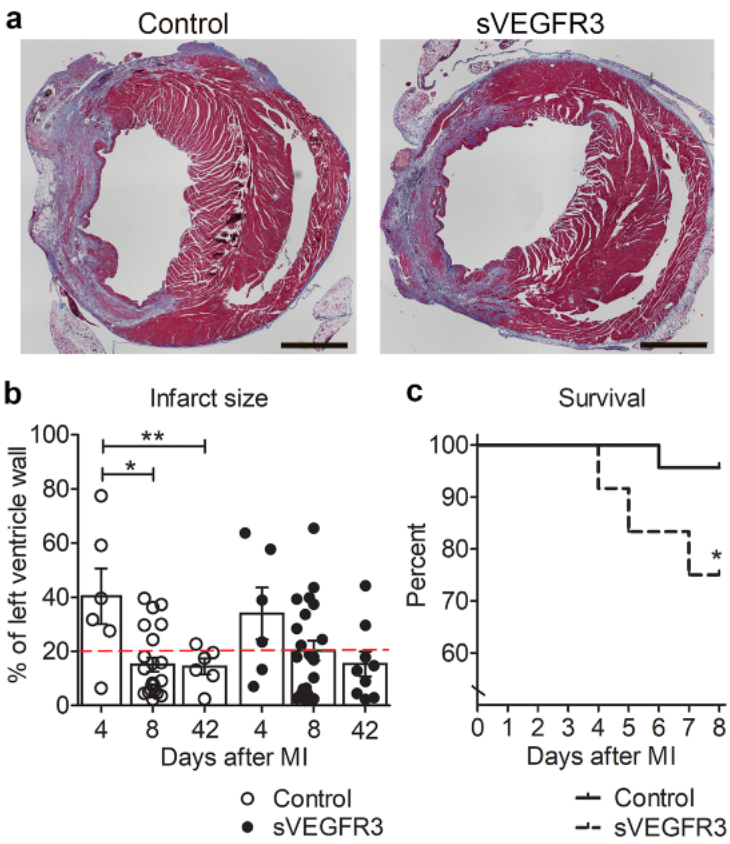

Figure 1. MI leads to higher mortality in sVEGFR3 mice compared to the controls. (**a**) Representative images of heart cross-sections stained with Masson's Trichrome staining show collagen accumulation and necrotic infarction scar in sVEGFR3 and control mice 8 days post-MI. (**b**) Quantification of infarction area sizes 4, 8 and 42 days post-MI (n = 6/group, n = 22/group and n = 6–9, respectively). Infarct areas above the red dashed line (20%) are considered large. (**c**) Mortality of sVEGFR3 and control mice during 8 day follow-up after LAD ligation (n = 23–24/group). Scale bar in (**a**) is 1,000 µm. Values represent mean ± SEM. Statistical analyses were performed using two-way ANOVA with Bonferroni's post-hoc test or Kaplan-Mayer with log-rank test for survival curve. $^{*}P < 0.05$, $^{**}P < 0.01$.

Cardiac arrhythmias have also been associated with lymphedema both in humans and in animal models[14]. On the other hand, lymphangiogensis has been observed in rats[15] and humans[11] after MI. In addition, lymphangiogenic therapy with vascular endothelial growth factor receptor 3 (VEGFR3)-specific vascular endothelial growth factor C (VEGF-C) protein improved LV function after MI in mice[9] and resolved cardiac edema and fibrosis in rats[16]. It has also recently been shown in a human phase 1 clinical trial that the gene transfer of another VEGFR3 ligand, VEGF-D, improves cardiac blood flow in refractory angina patients[17].

Here we analyzed the role of VEGFR3 in cardiac lymphatic vessel morphology and cardiac function in healthy hearts and after MI in mice. We used two mouse models with defective VEGFR3 signaling: sVEGFR3 mice expressing soluble decoy VEGFR3 (sVEGFR3) and Chy mice with inactivating point mutation in VEGFR3 gene (Chy)[6]. The blocking of the VEGFR3 signaling altered the structure of cardiac lymphatics in healthy hearts but did not affect cardiac function. After MI, sVEGFR3 mice had significantly higher mortality than the control littermates, intramyocardial hemorrhages, a reduced capability to respond to lymphangiogenic signals and a modified structure of the infarcted area.

Results

sVEGFR3 mice have higher mortality after MI than control mice.

To study the role of lymphatic vessels in MI, the anterior branch of the left descending coronary artery (LAD) was ligated in sVEGFR3 and control mice to generate an anteroapical infarctionin the LV wall (LVW). In order to analyze different stages of myocardial healing after LAD ligation, mice were followed for 4, 8 or 42 days. LAD ligation induced typical signs of MI, such as inflammatory cell accumulation, fibrosis and scar formation (Fig. 1a). The largest infarction areas

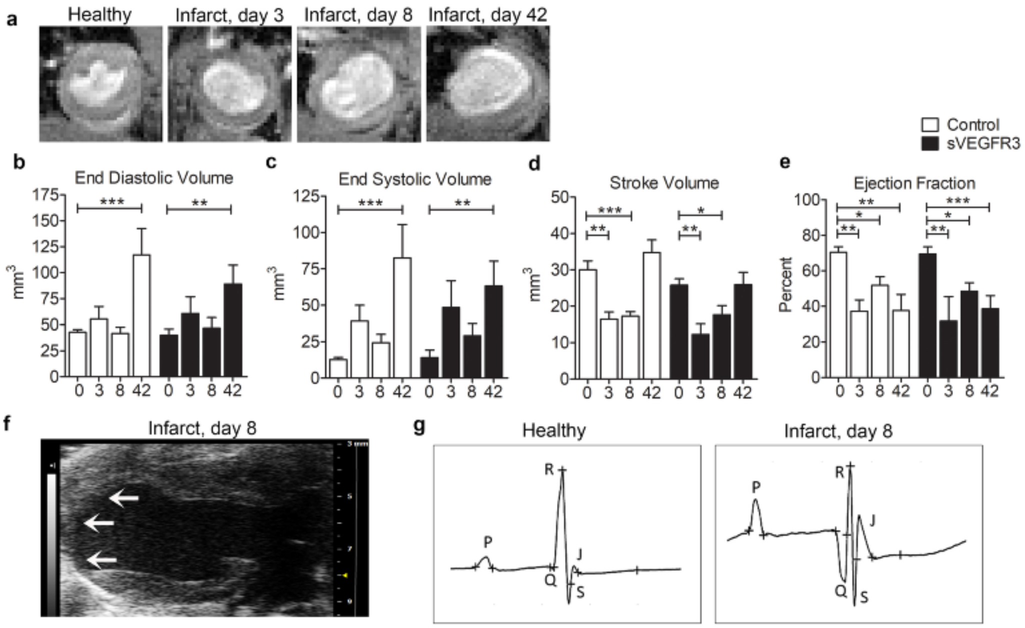

Figure 2. sVEGFR3 mice and control mice have similar heart function. **(a)** Examples of MRI cine images from healthy and infarcted hearts 3, 8 and 42 days post-MI show dilatation of the heart and thinning of the LVW. **(b,e)** EDV (**b**), ESV (**c**), SV (**d**) and EF (**e**) measured from cine MRI images in healthy hearts (0) and 3, 8 and 42 days post-MI (n = 8–11/group, n = 4/group, n = 14–18/group and n = 6–9/group, respectively). (**f**) An example of echocardiogram image from infarcted heart shows clear thinning of the apical LVW. Infarction scar is shown by arrows. (**g**) Examples of ECG profiles show pathological Q waves and changes in R and S wave amplitudes in an infarcted heart compared to a healthy heart. Values represent mean ± SEM. Statistical analyses were performed using two-way ANOVA with Bonferroni's post-hoc test. ${}^{*}P < 0.05$, ${}^{**}P < 0.01$, ${}^{***}P < 0.001$.

were detected already 4 days after MI both in sVEGFR3 mice and control mice. The average infarction area was decreased at the later time points in both groups reaching significance in control mice (39.6% at 4 days post-MI vs. 15.1% at 8 days post-MI, $P < 0.01$ and 14.4% 42 days post-MI, $P < 0.01$) (Fig. 1b). During the 8 day follow-up, the mortality of sVEGFR3 mice was significantly higher compared to the control group (25% vs. 4%, respectively, $P < 0.05$) (Fig. 1c). This might be explained by a higher proportion of the larger infarction areas in sVEGFR3 mice than in control mice: 40.9% of sVEGFR3 mice had infarction areas spanning more than 20% of the LVW, whereas only 27.2% of control mice had these large infarcted areas (Fig. 1b). Furthermore, 5 out of 6 sVEGFR3 mice that died during the 8 day follow-up had infarction areas larger than 20% of the LVW (Fig. 1b).

MI induced changes in the cardiac function in sVEGFR3 mice and control mice. Cardiac magnetic resonance imaging (cMRI) was utilized to measure heart function and to visualize the infarction area. The thinning of the LVW and the dilatation of the LV were easily detectable from cine MRI images at all time points after MI (Fig. 2a). LV volumes in diastole (EDV) and systole (ESV) were measured from cine MRI images (Fig. 2b,c). Additionally, stroke volume (SV) and ejection fraction (EF) were calculated by using EDV and ESV values (Fig. 2d,e). Compared to healthy hearts, ESV values increased slightly already 3 and 8 days after MI (Fig. 2c) and EDV and ESV values were significantly increased 42 days post-MI both in sVEGFR3 mice (EDV: 40.0 mm^3 in healthy hearts vs. 89.1 mm^3 8 days post-MI, $P < 0.01$) and in control mice (EDV: 42.8 mm^3 in healthy hearts vs. 117.2 mm^3 at 42 days post-MI, $P < 0.001$), which confirms the dilatation of the LVW (Fig. 2b,c). Increased ESV values caused SV values to decrease significantly 3 and 8 days post-MI both in sVEGFR3 mice (25.8 mm^3 in healthy hearts vs. 12.3 mm^3 at 3 days post-MI, $P < 0.01$ and 17.6 mm^3 at 8 days post-MI, $P < 0.05$) and in control mice (30.0 mm^3 at in healthy hearts vs. 16.4 mm^3 at 3 days post-MI, $P < 0.01$ and 17.3 mm^3 at 8 days post-MI, $P < 0.05$) (Fig. 2d). Compared to healthy hearts, EF was significantly decreased 3, 8 and 42 days post-MI sVEGFR3 mice (69.4% vs. 31.7%, $P < 0.01$, 48.4%, $P < 0.05$ and 38.6%, $P < 0.001$, respectively) and in control mice (70.4% vs. 37.2%, $P < 0.01$, 51.8%, $P < 0.05$ and 37.6%, $P < 0.01$, respectively) indicating progressive reduction in the pumping efficacy of the infarcted hearts (Fig. 2e).

Echocardiography was performed for the healthy hearts and 7 and 35 days post-MI to obtain more knowledge about the changes in heart function caused by LAD ligation. The thinning of the LVW was easily visible from long-axis view (LAX) of echocardiography 8 days post-MI (Fig. 2f). In addition, electrocardiograms (ECG) were recorded during echocardiography. As previously described[18], pathological Q waves appeared in ECG post-MI

		QRS (ms)	Q dur (ms)	Amp Q (mV)	Amp R (mV)	Amp S (mV)	HR (bpm)
Healthy	Control	10.1	1.0	−0.2	12.5	−6.4	454
	sVEGFR3	10.4	0.4	0.0	11.8	−5.1	463
Infarcted, 7 days post-MI	Control	12.3	3.1	−0.8	9.3	−4.8	480
	sVEGFR3	12.2	2.7*	−0.7	8.1	−4.0	486
Infarcted, 35 days post-MI	Control	12.1	5.5***	−1.4	4.5**	−2.4**	507
	sVEGFR3	10.4	2.1#	−1.2	6.9*	−5.4	489

Table 1. Quantification of ECG profiles in healthy hearts and 8 days and 35 days post-MI in sVEGFR3 mice and the control mice. QRS: Duration of QRS complex, Q dur: Q wave duration, Amp Q: Q wave amplitude, Amp R: R wave amplitude, Amp S: S wave amplitude, HR: heart rate. bpm: beats per minute. n = 9–10/group in healthy hearts, n = 17–20/group 7 days post-MI and n = 5–9/group 35 days post-MI. Values represent mean ± SEM. Statistical analyses were performed using one-way ANOVA with Bonferroni's post-hoc test. $^{*}P < 0.05$, $^{**}P < 0.01$, $^{***}P < 0.001$ when compared to healthy heart, $^{\#}P < 0.05$ when compared to control mice at the same time point.

both in sVEGFR3 and control mice (Fig. 2g). In addition, clear changes in R wave and S wave amplitudes were detected. ECG profiles were similar between sVEGFR3 mice and controls both in healthy and post-MI states (Table 1).

Cardiac lymphatic vessel morphology and lymphangiogenesis are modified in sVEGFR3 mice.

To determine the effect of attenuated VEGFR3 signaling on lymphatic vessel morphology, 3D hierarchy of cardiac lymphatic vessels was studied after immunostaining with LYVE1 marker from the anterior surface of the heart (Fig. 3a) and specifically from the anterioapical pieces of the heart (Fig. 3b). Lymphatic vessels were shown to be dilated in otherwise healthy sVEGFR3 mice in comparison to control mice. In Chy mice, the vessels had completely lost their fishnet-like organization and formed large sheet-like structures (Fig. 3a,b). Nuclear PROX1 staining indicated that the abnormal morphology did not result from the proliferation of LECs (Fig. 3c). sVEGFR3 mice had significantly increased lymphatic vessel area (24.2%) compared to control mice (18.7%) ($P < 0.05$). In Chy mice, lymphatic area in the region-of-interest (ROI) varied from approximately 39% up to 90% ($P < 0.001$) (Fig. 3d). Gender or diet did not affect the cardiac lymphatic vessel organization (data not shown).

Attenuated lymphatic vessel function leads to the accumulation of tissue fluids[19]. Long-lasting edema can influence the development of fibrosis and thereby alter the healing after MI[20]. Previously, T_2 weighted MRI method has been used to noninvasively visualize and quantitate edematous regions in humans and animal models[21–23]. Here we used T_2 weighted MRI to measure cardiac edema in healthy hearts, 8 days and 42 days post-MI (Fig. 4a). T_2 relaxation times were significantly increased in infarcted hearts at both time points compared to the healthy hearts (0.027 s at d0 vs. 0.046 s 8 days after MI, $p < 0.001$ and 0.047 s 42, $p < 0.001$ in sVEGFR3 mice).

To resolve the accumulation of fluids and inflammatory cells in the myocardium after MI, lymphangiogenesis is activated both in the infarcted regions and in healthy LVW[16]. Here we analyzed the expression of VEGFR3 and VEGF-C with RT-qPCR to determine if these main lymphangiogenic regulators are activated after MI. VEGF-C was upregulated both in sVEGFR3 and control mice when compared to healthy hearts 8 days after MI ($P < 0.05$) (Fig. 4b). Also, the expression of VEGFR3 was considerably increased in sVEGFR3 mice and it was significantly upregulated in control mice ($P < 0.01$). Furthermore, the localization and number of lymphatic vessels after MI was evaluated from the cross-sections of LVW stained with LYVE1 antibody (Fig. 4c,d). In the controls, lymphatic vessels formed a dense network indicating activated lymphangiogenesis especially in the border zone of the infarcted area whereas in sVEGFR3 mice lymphatic vessels were nearly absent 8 days after MI (Fig. 4c). The amount of lymphatic vessels was similar in sVEGFR3 mice and control mice 4 days after MI but it was significantly increased in control mice 8 days after MI (3,9 /mm^2 4 days post-MI vs. 10.5 /mm^2 8 days post-MI. $P < 0.05$) and remained at high level until the day 42 (Fig. 4d) confirming strongly activated lymphangiogenesis in control mice during the healing of the myocardium after MI. In contrast, the amount of lymphatic vessels increased only slightly in sVGEFR3 mice during the follow-up and the amount was significantly lower in sVEGFR3 mice compared to control mice 8 days after MI (6.1/mm^2 vs. 10.5/mm^2, respectively. $P < 0.05$) (Fig. 4d) indicating attenuated capability to respond to lymphangiogenic signals.

sVEGFR3 mice display intramyocardial hemorrhages.

To evaluate the angiogenic response after MI, blood capillaries were stained with Lectin (Fig. 5a) and quantified from the border zone of the infarcted area (Fig. 5b). The highest amount of capillaries was detected 4 days after MI in both groups and it was significantly decreased at the later time points. The amount of capillaries was equal between sVEGFR3 mice and control mice indicating similar responses to angiogenic signals. Unexpectedly, most of the sVEGFR3 mice that died during the 8 day follow-up displayed large hemorrhages in the infarcted area indicating leakiness from blood vessels (Fig. 5c). The scoring of the hemorrhagic areas of infarcted areas covering more than 10% of LVW revealed large accumulations of erythrocytes especially in sVEGFR3 mice followed for 8 days (Fig. 5d). As downregulation of VEGFR3 signaling has been shown to increase VEGFR2 levels and thereby vascular permeability[24], we measured the levels of VEGFR2 in healthy hearts by Western blotting (Fig. 5e). The amount of VEGFR2 protein was significantly increased in the healthy hearts of sVEGFR3 mice ($P < 0.05$) (Fig. 5f). Additionally, the expression of endothelial nitric oxide synthase (eNOS) was upregulated in sVEGFR3 mice 8 days after MI compared to controls

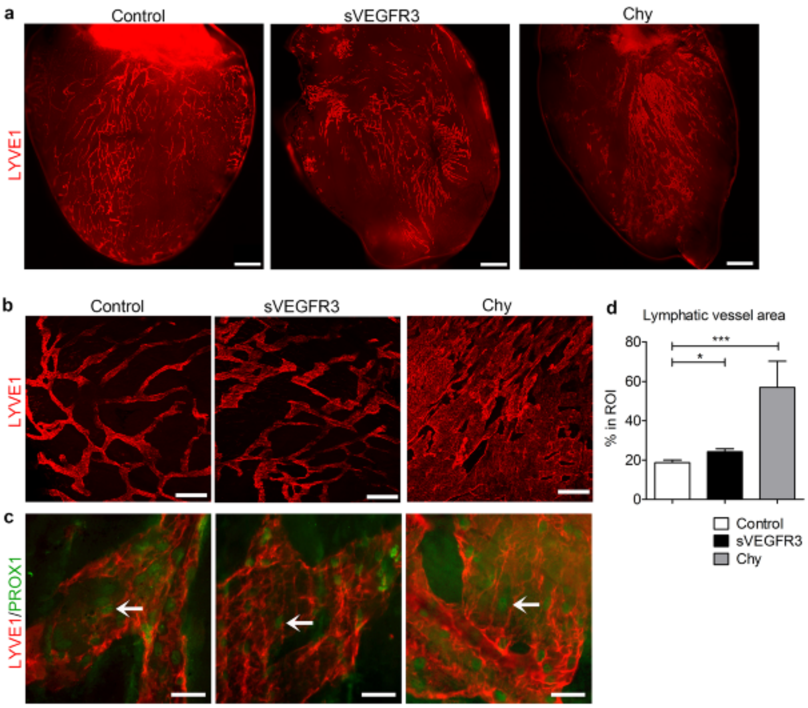

Figure 3. Cardiac lymphatic vessels are dilated in healthy sVEGFR3 mice and completely loose their organization in Chy mice. (**a**) Representative images of LYVE1 positive subepicardial cardiac lymphatics in the anterior side of the heart in the healthy control mice, sVEGFR3 mice and Chy mice. (**b**) Representative images of LYVE1 positive cardiac lymphatic vessels in LVW in the healthy control mice, sVEGFR3 mice and Chy mice. (**c**) Representative images of PROX1 and LYVE1 double-stainings in LVW in the healthy control mice, sVEGFR3 mice and Chy mice. Arrows indicate PROX1-positive LEC nuclei. (**d**) Quantification of LYVE1 stainings ($n = 11$/control mice, $n = 17$/sVEGFR3 mice and $n = 4$/Chy mice). Scale bar in (**a**) is 1,000 µm, in (**b**) 200 µm and in (**c**) 50 µm. Values represent mean ± SEM. Statistical analyses were performed using Student's t-test. $^{*}P < 0.05$, $^{***}P < 0.001$.

($p = 0.07$) indicating that the expression of sVEGFR3 may induce changes in the heart vasculature during MI by modulating VEGFR2-mediated vascular permeability.

sVEGFR3 mice and control mice had equal levels of inflammatory cells. Myocardial necrosis after MI triggers the recruitment of inflammatory cells that clear the wound from dead cells and matrix debris. To analyze the inflammatory reaction after MI, macrophages and lymphocytes were stained with F4-80 and CD45 antibodies, respectively, from the cross-sections of infarcted hearts. Eight days after MI, F4-80+ macrophages were mainly located in the epicardium of LVW (Fig. 6a) whereas CD45+ lymphocytes were scattered throughout the infarction area (Fig. 6b). Healthy areas were almost completely devoid of inflammatory cells. Even though sVEGFR3 mice had a slight increase in the amount of lymphocytes, no significant changes in the amount of inflammatory cells in LVW were detected between control mice and sVEGFR3 mice 8 days after MI (Fig. 6c).

Histology and novel MRI methods revealed changes in the structure of infarcted areas in sVEGFR3 mice. After the infiltration of inflammatory cells, proinflammatory signaling is suppressed in the infarcted areas and fibroblasts turn into activated myofibroblasts. Myofibroblasts produce large amounts of collagens that provide tensile strength for the myocardial wall and protect it from rupture[25]. To assess the production of fibrotic and contractile proteins in the myocardium after MI, RT-qPCR analyses were performed for collagens (Col1A2 and Col3A1), periostin (Postn), smooth muscle cell actin (Acta2) and transforming growth factor beta 1 (Tgfb1) (Fig. 7a). The expression of collagens and Postn were significantly decreased 42 days after MI compared to the expression in the 8 day samples. The expression of both Col1A2 and Col2A3 were slightly but not significantly decreased in sVEGFR3 mice compared to the controls 8 days post-MI. Acta1 was strongly upregulated in sVEGFR3 mice 42 days after MI ligation indicating accumulation of α-SMA positive cells (primarily myofibroblasts) in the LVW. This finding was supported by immunohistochemical staining for α-sma which revealed the accumulation of individual α-sma positive cells and small arterioles in the healthy LVW of sVEGFR3 mice 42 days after MI whereas α-sma was more prominently expressed in the larger arteries in control

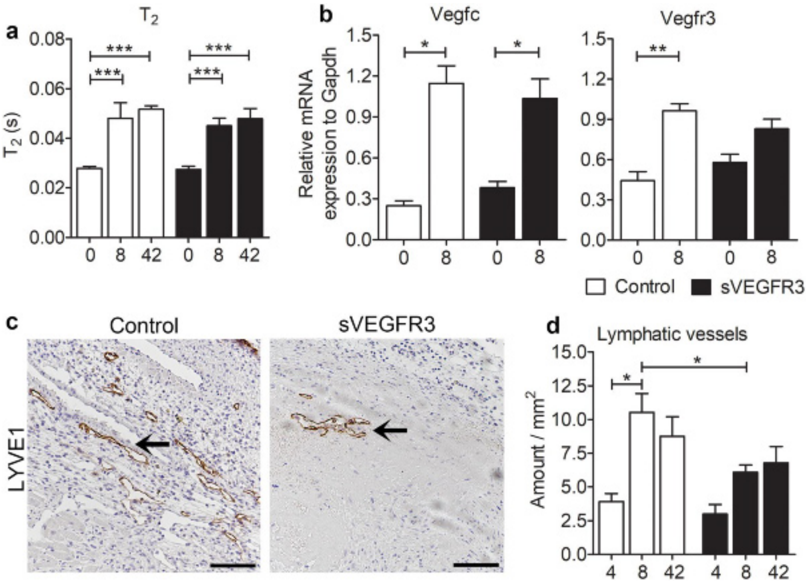

Figure 4. Cardiac lymphatic vessels in sVEGFR3 mice are unable to respond to lymphangiogenic signals after MI. (**a**) MRI T_2 relaxation times in healthy hearts and 8 and 42 days post-MI (n = 8–9/group, n = 5–6/group and n = 8–9/group, respectively). (**b**) RT-qPCR analyses for Vegf-c and Vegfr3 mRNA in healthy hearts and 8 days post-MI (n = 2–3/group and n = 9–15/group, respectively). (**c**) Representative images of LYVE1 positive cardiac lymphatic vessels in heart cross-sections 8 days post-MI in sVEGFR3 and control mice. Arrows indicate LYVE-1 positive lymphatic vessels. (**d**) Quantification of LYVE1 stainings 4, 8 and 42 days post-MI (n = 5–6/group, n = 12–16/group and n = 6–9/group, respectively). Scale bar in (**c**) is 125 µm. Values represent mean ± SEM. Statistical analyses were performed using two-way ANOVA with Bonferroni's post-hoc test or Student's t-test. $^{*}P < 0.05$, $^{**}P < 0.01$, $^{***}P < 0.001$.

mice (Fig. 7b). sVEGFR3 mice and control mice had similar amounts of α-sma positive structures (Fig. 7c) but sVEGFR3 mice displayed a trend towards smaller α-sma positive cells and arterioles whereas the proportion of large α-sma positive arteries was significantly higher in control mice than in sVEGFR3 mice (57.1% vs. 48.0%, $P < 0.05$, respectively)(Fig. 7d).

The amount of fibrosis was further analyzed from heart cross-sections stained with Picro-Sirius red that allowed the visualization of collagen types I and III. Interestingly, the intensity of collagen staining was fainter in several sVEGFR3 mice compared to control mice 8 days post-MI (Fig. 7d), which indicates a different composition of the fibrotic area. However, there were no differences in the total amount of collagen in LVW between sVEGFR3 mice and control mice 8 days or 42 days after MI (Fig. 7e).

Recently, a new non-invasive MRI method, longitudinal relaxation time in rotating frame ($T_{1\rho}$) has been introduced to detect granulation and scar tissue formation in myocardial ischemia in mice[26]. Additionally, relaxation times of relaxation along a fictitious field (T_{RAFF2} and T_{RAFF4}) are novel rotating frame relaxation time methods for measuring damaged areas of acute and chronic MI scar components with high accuracy and with lower specific absorption rate than $T_{1\rho}$[27]. To analyze the changes in LVW composition after MI, we performed $T_{1\rho}$, T_{RAFF2} and T_{RAFF4} relaxation time cMRI for a subset of mice 7 days after LAD ligation (Fig. 7f,h). All methods were able to differentiate infarcted regions of the LVW from the remote healthy areas. Interestingly, sVEGFR3 mice had significantly increased T_{RAFF4} relaxation times compared to the controls (0.263 s vs. 0.149 s, respectively. $P < 0.05$) and also a trend towards higher T_{RAFF2} relaxation times (0.0795 s vs. 0.0596 s, respectively) in the infarcted region of LVW (Fig. 7g,h). These findings indicate changes in the composition of infarcted area in sVEGFR3 mice after MI.

Discussion

We have studied the role of VEGFR3 in cardiac lymphatic vessels and in healing after MI. Confocal microscopy analyses revealed that cardiac lymphatic vessels formed an organized network in the epicardium of the LVW in control mice. In contrast, cardiac lymphatic vessels in sVEGFR3 and Chy mice had more disorganized and dilated morphology. Interestingly, the mortality of the sVEGFR3 mice was significantly higher in the acute phase after MI than their control littermates, emphasizing the importance of VEGFR3 signaling and the function of lymphatic vessels in the healing after MI.

VEGFR3 is the primary lymphangiogenic receptor for growth factors VEGF-C[28] and VEGF-D[29]. It is expressed in cardiac LECs both during the development and postnatally[9]. In the current study, we used transgenic mice that produce VEGFR3 decoy receptor under the K14 promoter that targets the receptor expression

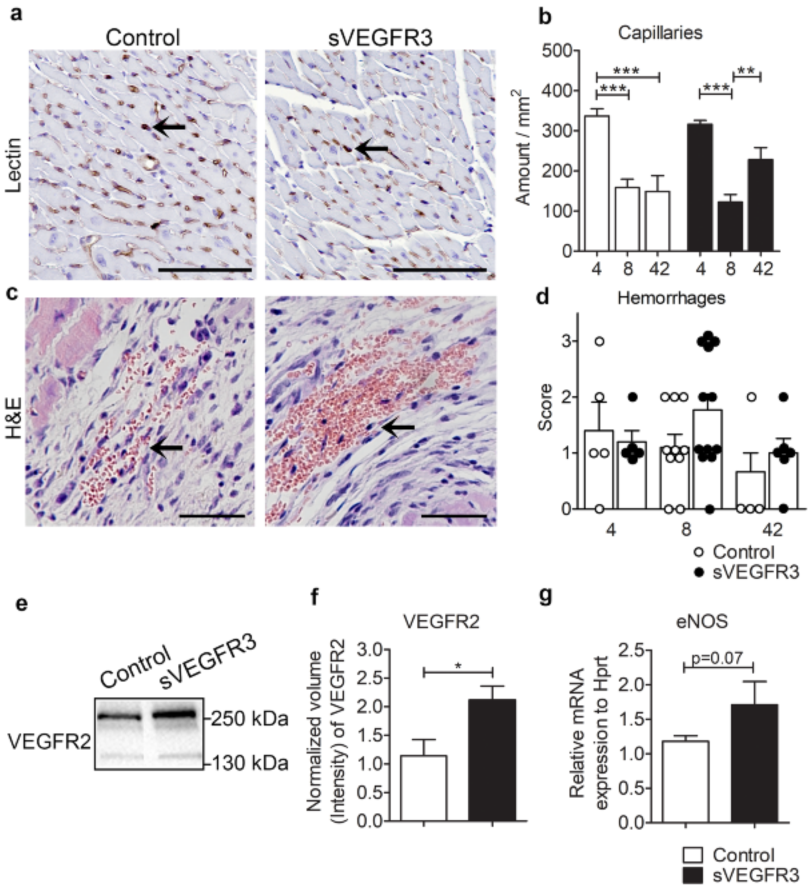

Figure 5. Histological examination revealed hemorrhages in the infarcted areas of sVEGFR3 mice. (**a**,**b**) Representative images of Lectin positive cardiac blood capillaries in heart cross-sections 8 days post-MI in sVEGFR3 and control mice. Arrows indicate Lectin positive capillaries. (**b**) Quantification of Lectin stainings 4, 8 and 42 days post-MI (n = 6/group, n = 21/group and n = 6–9/group). (**c**) Representative images of intramyocardial hemorrhages in control mice and sVEGFR3 mice. Arrows indicate red blood cells (RBCs) (**d**) Scoring of RBCs in infarcted area of LVW 4, 8 and 42 days post MI (n = 5/group, n = 10–12/group and n = 4–5/group, respectively). Score 0: no RBCs, 1: few RBCs, 2: hemorrhages 3: multiple hemorrhages. (**e**,**f**) Western blot (**e**) and quantification (**f**) of VEGFR2 in the healthy hearts of sVEGFR3 mice (n = 4–5/group). (**g**) qPCR analysis of eNOS in the hearts of sVEGFR3 mice and controls 8 days after the infarction (n = 9–15/group). Scale bar is (**a**) 100 µm and in (**c**) 50 µm. Values represent mean ± SEM. Statistical analyses were performed using two-way ANOVA with Bonferroni's post-hoc test or Student's t-test. $^{*}P < 0.05$, $^{**}P < 0.01$, $^{***}P < 0.001$.

in the keratinocytes of the skin. sVEGFR3 protein is secreted in the blood stream and has shown to cause both metabolic[6,30] and structural effects[31] in the lymphatics. Even though VEGFR3 function is not completely lost in sVEGFR3 mice, partial inhibition of VEGF-C and VEGF-D was sufficient for the downregulation of lymphangiogenic signaling leading to modifications in the structure of cardiac lymphatics. Additionally, cardiac lymphatic vessel morphology was significantly altered and lymphatics formed large sheet-like structures in the Chy mice that have an inactivating mutation in the VEGFR3 gene. Unfortunately, the analysis of Chy mice is very challenging due to their poor breeding performance and intolerance for anesthetics. It is likely that the formation of cardiac lymphatic vessels is already altered during embryonic development both in sVEGFR3 and Chy mice. This is supported by the previous findings from other parts of the body showing that many internal organs in the sVEGFR3 newborn mice are devoid of lymphatic vessels[31] and some newborn Chy mice develop abdominal chylous ascites that is not absorbed due to defective lymphatic network[32]. Unexpectedly, 25% of the sVEGFR3 mice died during the first week after MI whereas control mice survived much better during this acute phase after MI indicating that either the structural changes in cardiac lymphatic system or downregulation of VEGFR3 signaling is detrimental for the healing after MI.

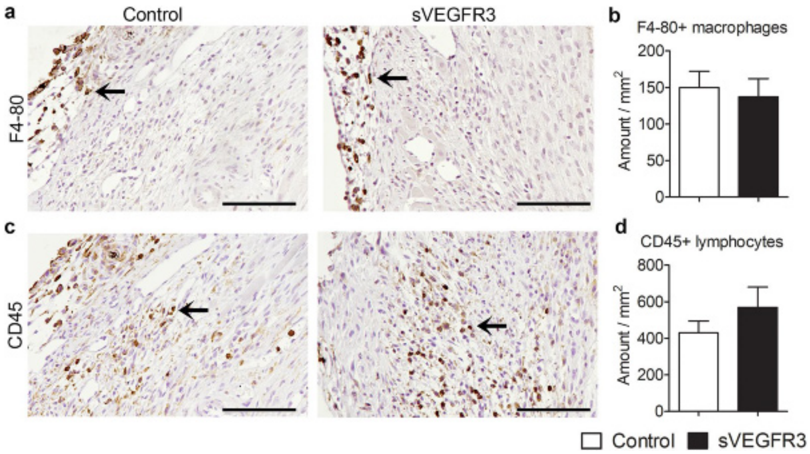

Figure 6. sVEGFR3 mice and control mice display similar amounts of inflammatory cells in LVW. (**a**,**b**) Representative images (a) and quantification (b) of F4–80 stainings 8 days post-MI (n = 14–17/group). (**c**,**d**) Representative images (c) and quantification (d) of CD45 stainings 8 days post-MI (n = 16–17/group). Scale bar in (**a**) and (**c**) is 100 µm. Values represent mean ± SEM. Statistical analyses were performed using Student's t-test.

MI causes decreased cardiac lymph flow leading to edema both in humans[33] and in large animals[34]. Cardiac edema can strongly modulate cardiac function and lead to dangerous ventricular arrhythmias[14] that are typically the main cause of sudden death after MI[35]. As in previous studies[15,16], control mice in this study exhibited activated lymphangiogenesis leading to dense lymphatic capillary network. In contrast, sVEGFR3 mice did not respond to VEGF-C upregulation and displayed significantly less lymphatics than control mice. It still remains an open question, whether cardiac lymphatic vessels in sVEGFR3 mice are unable to respond to lymphangiogenic signals after MI or if the pre-existing lymphatics were not functional due to developmental defects. To test this in the future, lymphangiogenesis could be inhibited using conditional transgenic mouse lines or by administering viral vector expressing sVEGFR3 to the myocardium of an adult animal during MI. We assumed that the lower number of cardiac lymphatics would lead to an accumulation of fluids in the heart muscle. T_2 relaxation times were indeed significantly increased 8 days and 42 days post-MI in both groups but T_2 relaxation time did not differ between the groups. However, the effects of cardiac edema cannot be totally ruled out as even small increase in the water content of the heart significantly decreases cardiac output[36]. In a recent clinical trial, the activation of both angiogenesis and lymphangiogenesis with adenoviral VEGF-D therapy was shown to be beneficial for myocardial perfusion and might have also improved cardiac fluid balance[17]. Additionally, VEGF-C therapy in a rat model decreased cardiac water content only by 0.8% compared to the controls but was shown to be beneficial for cardiac healing[16]. Therefore, even a slight increase in cardiac fluid accumulation after MI can lead to a higher mortality in sVEGFR3 mice. Additionally, the accumulation of macrophages has been associated with increased vascular leakage and tissue edema[37] and activation of lymphangiogenesis could help to resolve innate inflammatory reaction[38]. We did not discover differences in the inflammatory cell counts between sVEGFR3 mice and control mice indicating similar responses to inflammatory activation at least in the current study setup. However, VEGFR3 signaling can modulate macrophage polarization[30], which might modify myocardial healing after MI.

sVEGFR3 mice followed for 8 days displayed intramyocardial hemorrhages indicating microvascular dysfunction and vascular leakage of erythrocytes. Hemorrhages can cause detrimental remodeling and reduced wall motion of the LVW[39] and they are often discovered in mice with lethal cardiac rupture[40]. Mechanistically, hypoxia after coronary artery occlusion induces the expression of cytokines, growth factors and reactive oxygen species, which can alter the integrity of the microvascular endothelium and lead to increased vascular permeability[41]. The expression of sVEGFR3 led to significantly increased VEGFR2 protein levels in healthy hearts of sVEGFR3 mice compared to controls, which induced the expression of eNOS, one of the main factors regulating vascular permeability[42]. In addition to eNOS, upregulated levels of VEGFR2 can cause increased vascular permeability by decreasing VE-cadherin at endothelial cell junctions without changing vascular structure or density[24], which might be an additional mechanism also in sVEGFR3 mice. Furthermore, chow-fed sVEGFR3 mice are hypercholesterolemic[6], which could cause vascular dysfunction and increased vascular permeability in the heart[43].

Vascular leakage and persisted edema has been shown to modify the development of fibrosis in the heart[20]. Although the expression of ECM proteins, Col1a2, Col3a1 and Postn were at a similar level both in the controls and sVEGFR3 mice, some sVEGFR3 mice had fainter histological staining of collagen I and III after MI. Accordingly, sVEGFR3 mice had a significantly different composition of the infarcted area compared to the controls when the infarcted area was analyzed with novel MRI techniques, T_{RAFF2} and T_{RAFF4} rotating frame relaxation methods. T_{RAFFn} is produced by nested sine amplitude and cosine frequency modulated radio frequency (RF) pulses[44]. The method is based on a fast, sub-adiabatic sweep of effective RF field which produces a fictitious

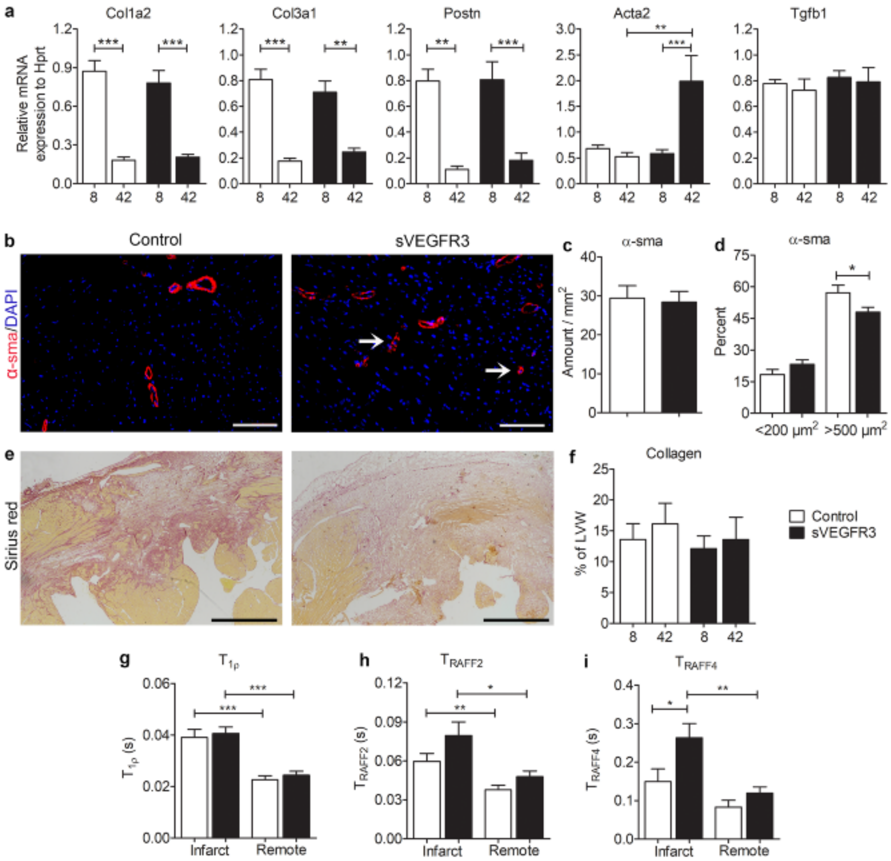

Figure 7. Histology and novel MRI methods display differential fibrosis in sVEGFR3 mice when compared to the controls. (**a**) RT-qPCR analyses for Col1a2, Col3a1, Postn, Acta2 and Tgfb1 mRNAs 8 and 42 days post-MI (n = 14–18/group and n = 4–9/group, respectively). (**b**) Representative images of α-sma staining in heart cross-sections 42 days post-MI in sVEGFR3 and control mice. Arrows point at individual α-sma positive cells. (**c**) Amount of α-sma positive area in the healthy LVW in sVEGFR3 and control mice (n = 6–9/group). (**d**) Proportion of small (<200 µm) and large (>500 µm) α-sma positive structures in the healthy LVW (n = 6–9/group). (**e**) Representative images of Sirius Red staining in heart cross-sections 8 days post-MI in sVEGFR3 and control mice. (**f**) Quantification of collagen in LVW from Sirius Red stainings 8 and 42 days post-MI (n = 17–18/group and n = 6–9/group, respevctively). (**g,i**) MRI $T_{1\rho}$ (**g**), T_{RAFF2} (**h**) and T_{RAFF4} (**i**) relaxation times 7 days post-MI in infarcted and remote regions (n = 5–11/group). Scale bar in (**e**) is 100 µm and in (**h**) 500 µm. Values represent mean ± SEM. Statistical analyses were performed using two-way ANOVA with Bonferroni's post-hoc test or Student's t-test. $^{*}P < 0.05$, $^{**}P < 0.01$, $^{***}P < 0.001$.

magnetic field. The fictitious field component together with RF pulse induced magnetic field and off-resonance component forms a final effective RF field. Magnetization precesses around this final effective field and relaxes as a function of time[45]. T_{RAFF} has been shown to detect especially slow molecular motions[44]. T_{RAFF2} and T_{RAFF3} relaxation times increased at fibrotic areas in transverse aortic constriction mouse model[45] and T_{RAFF4} was recently utilized to differentiate white and grey matter and correlate highly with myelin content of the brain[46] with remarkably lower (approximately 80%) SAR-values of RAFF4 and (approximately 30%) SAR-values of RAFF2 compared to continuous wave $T_{1\rho}$ which is an advantage of RAFFn[44,46,47]. Interestingly, changes in infarcted area of sVEGFR3 mice were not detected with conventional MRI methods, T2 or T1ρ, indicating that T_{RAFFn} could be used to detect more specific modifications in the infarcted area related to chemical exchange of hydrogen between hydroxide groups and free water.

Even though novel imaging methods and transgenic animal models have provided new insights into the function of systemic and tissue-specific lymphatic vessels, the effects of altered cardiac lymphatic function in the healthy hearts and after MI have not been described. Here we show that VEGFR3 has an essential role in cardiac lymphatic vessel morphology and attenuated VEGFR3 signaling exposes mice to higher mortality, hemorrhages and a modified structure of the infarcted area verifying the importance of lymphatic vessel function in the healing after MI. Additionally, we showed that novel MRI techniques provide useful information about the changes in the LVW structure during the myocardial healing and these non-invasive methods could be utilized to determine the scar structures also in the clinical settings.

Materials and Methods

Animals. sVEGFR3 and Chy mice in LDLR$^{-/-}$ x ApoB$^{100/100}$ background were bred as previously described[6]. LDLR x ApoB$^{100/100}$ littermates from the breedings with sVEGFR3 mice served as controls. Mice were housed in the Laboratory Animal Center of University of Eastern Finland and they were fed ad libitum with water and normal rodent chow diet. Additionally, to test the effect of high-fat diet on cardiac lymphatic vessel morphology, mice were fed with Western type high-fat diet (TD.88137 Harlan Teklad; 42% of energy from fat, 0.2% cholesterol) for 12 weeks before euthanasia (n = 7/control mice n = 13/sVEGFR3 mice and n = 4/Chy mice). Mice were euthanized with carbon dioxide (CO_2) and perfused with phosphate-buffered saline (PBS) through the LV. All animal experiments were approved by National Experimental Animal Board of Finland and were carried out in accordance with the Act on the Protection of Animals Used for Scientific or Educational Purposes (497/2013).

Myocardial infarction (MI). Approximately 13–17 week old sVEGFR3 mice and control mice (n = 22/group) were used for MI study. Both female and male mice were used in equal numbers. Mice were anesthetized with isoflurane inhalation (Univentor-400, Univentor, Zejtun, Malta) 4% induction followed by 2% maintenance and MI was induced as previously described[48,49]. Briefly, the heart was exposed, pushed out of the thorax with a direct visual control and LAD was ligated at a site ≈5 mm from its origin using a 6-0 silk suture. Mice were sacrificed 8 days after the operation. In addition, some analyses were performed on mice followed for 4 days (n = 6/group) or 42 days (n = 10/control mice and n = 11/sVEGFR3 mice) after MI and a subset of mice used for $T_{1\rho}$ and T_{RAFFn} weighted MRI was followed for 7 days (n = 11/control mice and n = 7/sVEGFR3 mice). In total, 95 mice were used for the MI experiments.

Cardiac magnetic resonance imaging (cMRI). MRI was performed before the LAD ligation and during the follow-up (day 3, 8 and 42). All MRI experiments were done using a horizontal 9.4 T magnet controlled by a Bruker console (Bruker GmbH, Ettlingen, Germany). Quadrature volume transceiver with coil inner diameter of 35 mm (Rapid Biomed GmbH, Ettlingen, Germany) was used in MRI experiments. Mice were anesthetized for MRI with 4% isoflurane with oxygen and nitrogen gases by fraction of 1:3 (Piramal Healthcare, Northumberland, UK). The level of isoflurane was decreased to 1–1.5% level during the imaging. Mice body temperature was kept at natural temperature level (37 °C) by circulating warm water in watertubes which were placed under mice. ECG was measured using needle electrodes from fore paws and respiration was controlled by a pneumatic pillow placed under the mouse. Both signals were registered using Model 1025 (Small Animal Instruments Inc., NY, USA) during the experiments. All MRI experiments were gated with ECG and respiration.

Multi-slice cine images were taken to image the whole heart by using gradient echo based fast imaging with steady state precession (FISP) readout sequence. The imaging parameters for cine images were field-of-view = 4 × 4 cm^2, slice thickness = 1 mm, matrix size = 192 × 192, Time of Echo (TE) = 1.9 ms, Time repetition (TR) = 8.0 ms, scan TR = 99.0 ms, flip angle = 10° and number of frames were 10–11 depending on heart rate, 8–10 slices were imaged depending on the size of the heart. EDV and ESV were analyzed from cine frames with Matlab software using Aedes toolbox. SV was calculated using formula SV = EDV − ESV and EF was calculated using formula EF = (SV/EDV) × 100%.

T_2 measurements contained Hahn double echo preparation which included an adiabatic half passage (AHP) excitation-pulse (power = 1250 Hz, duration = 3.0 ms), two Hyperbolic Secant 1-pulses (power = 1250 Hz, duration = 4.5 ms) and AHP-backpulse (power = 1250 Hz, duration = 3.0 ms). Between the pulses symmetric delays were used resulting in total TEs of 0.05, 2.3, 4.5, 14.0 ms. Delays in front of T_2 preparation were 14.01 4.5, 2.3 and 0.05 ms, respectively. Rotating frame preparation module to measure T_{RAFFn} consisted of RAFF2 or RAFF4 pulses (pulses RF power 1250 Hz and 648 Hz, respectively duration 2.26 ms) applied in pulse trains of lengths 0, 9.1, 18.1 and 36.2 ms. In front of the RAFFn pulse trains was a delay with durations of 36.2, 27.15, 18.1 and 0 ms, respectively, to adjust imaging to occur at the same cardiac phase for weightings with different durations. $T_{1\rho}$ preparation was done using a rotating frame preparation module which consisted AHP pulse (power = 625 Hz, duration = 2.0 ms), continuous wave spin-lock-pulse with time-to-spin-lock TSL = 0.4, 9.4, 27.4 and 45.4 ms and AHP-backpulse[26]. Before $T_{1\rho}$ preparation a delay (45.4, 27.4, 9.4 and 0 ms, respectively to TSL) was added. FISP-readout sequence for a single slice was used in all relaxation time measurements with parameters: field-of-view = 4 × 4 cm^2, slice thickness = 1 mm, matrix size = 256 × 256, flip angle = 90°, TE = 1.9 ms, TR = 14.9 ms, scan was dependent both on the heart rate and the respiratory rate. Minimum delay between weighting pulses was 1460 ms. $T_{1\rho}$ and T_2 relaxation time maps were fitted by using a linear function. T_{RAFF2} and T_{RAFF4} were fitted by using a single mono-exponential decay function without taking into account the steady state formation.

Echocardiography and electrocardiography (ECG). Transthoracic echocardiography was performed on healthy mice and before the sacrification (day 7 or day 35). Mice were anesthetized with isoflurane and imaged using a high-frequency, high-resolution imaging system for small animals (Vevo 2100, VisualSonics, Toronto, Canada) equipped with a transducer probe operating at 18–38 MHz (MS-400, VisualSonics). In addition, surface electrocardiography (ECG) signal was acquired during echocardiography. The paws of the mice were attached to the electrode pads of the heated platform (36–37 °C). ECG data were exported from Vevo software (VisualSonics) and analyzed with rodent ECG imaging software (Kubios HRV 2.0, Kuopio, Finland) as previously[18].

Real-time Quantitative PCR (RT-qPCR). The proximal part of the heart was snap-frozen in liquid nitrogen for molecular biology analyzes. RNA was extracted with RNeasy Mini Kit (Qiagen, Hilden, Germany) and RNase treatment was performed with Turbo DNA-Free^{TM} kit (ThermoFisher Scientific, Waltham, MA, USA) according to the manufacturer's protocols. RNA was transcribed into cDNA with RevertAid Reverse Transcriptase (ThermoFisher Scientific). Taqman assays (ThermoFisher Scientific) as well as PrimeTime qPCRs (IDT, Coralville, IA, USA) were used to analyze the expression of genes related to lymphangiogenesis and fibrosis.

Histology and immunohistochemistry. For immunohistology, tissue samples were fixated in 4% paraformaldehyde-PBS overnight. After fixation, approximately 1 mm thick piece of the anterior side of the heart was stored in PBS for confocal microscopy. Samples for histological stainings were processed to paraffin and cut as 4 µm sections.

For visualization of lymphatic vessels, tissues were incubated with a LYVE1 antibody (1:1000, Reliatech, Wolfenbuttel, Germany) with 5% goat serum in PBS containing 0.3% Triton-x100 and 0.2% BSA overnight following washing steps and incubation with a Goat anti-rabbit Alexa 594 (1:500, ThermoFisher Scientific) secondary antibody overnight. For further visualization of LECs, tissues were first incubated with PROX1 antibody (1:50, R&D Systems, Minneapolis, MN, USA) using Donkey anti-goat Alexa 594 (1:500,ThermoFisher Scientific) as a secondary antibody and then with LYVE1 antibody using Chicken anti-rabbit Alexa 488 (1:500,ThermoFisher Scientific) as a secondary antibody. After washes with PBS, tissues were imaged with confocal microscope (Zeiss LSM700, Carl Zeiss, Oberkochen, Germany) or fluorescent microscope (Nikon Eclipse Ni, Nikon, Tokyo, Japan). Lymphatic vessels area in ROI was quantified with ImageJ software.

Infarct sizes and hemorrhages were analyzed from Hematoxylin-Eosin stainings 4, 8 and 42 days post-MI at the level of papillary muscles (3–4 tissue sections/mouse). To analyze post-MI fibrosis, tissue sections were stained with Masson's trichrome (Sigma-Aldrich, St Louis, MO, USA) and Picro Sirius red (Abcam, Cambridge, UK) according to the manufacturer's protocols. Immunohistochemical stainings were performed with antibodies recognizing lymphatic vessels (LYVE1, 1:1000), macrophages (F4-80, 1:500, Biorad, Hercules, CA, USA), lymphocytes (CD45, 1:50, BD Biosciences, San Jose, CA, USA) and α-sma (anti-alpha smooth muscle actin-Cy3, 1:200, Sigma-Aldrich). Blood capillaries were stained with biotinylated lectin (Biotinylated Griffonia (Bandeiraea) Simplicifolia Lectin I, 1:100, Vector Laboratories). To improve unmasking of the antigen and enhance the intensity of the staining, antigen retrieval with boiling in citrate buffer was used for LYVE1 and F4-80 antibodies and BD Retrievagen A solution (BD Biosciences) for CD45 antibody. To visualize the binding of the antibody, tissue sections were incubated with biotinylated IgG secondary antibodies (1:500, Vector Laboratories, Burlingame, CA, USA) followed by avidin-biotin-HRP step (Vector Laboratories) and a choromogen DAB (ThermoFisher Scientific). Tissue slides were mounted with Permount (ThermoFisher Scientific) for light imaging or Vectashield mounting medium with DAPI (Vector Laboratories) for fluorescent imaging. Tissue sections were imaged with NIS elements software (AR5.50.00, Nikon) connected to a light microscope (Nikon Eclipse Ni, Nikon). Image analyses were performed with ImageJ software equipped with Fiji image processing package.

Protein extraction and western blotting. Proteins were extracted using T-PER Tissue Protein Extraction Reagent (Thermo Fisher Scientific) and total protein content was determined using BCA protein assay (Pierce, Thermo Fisher Scientific). 40 µg of protein was separated on Mini-PROTEAN TGX Stain-Free gels (BioRad). Gel was activated by UV for 2.5 min and proteins were transferred to nitrocellulose membrane (BioRad). The membrane was blocked in TBST (Tris-buffered saline with Tween 20) containing 5% nonfat dry milk and incubated with a rabbit anti-mouse VEGFR2 (Cell Signaling) primary antibody and a goat anti-rabbit secondary antibody (Thermo Fisher Scientific). Total protein amount was measured with ChemiDox XRS before enhanced chemiluminescence (ECL) detection. Specific bands were normalized to total protein using the ImageLab (Bio-Rad) software.

Statistical analyses. Two-tailed unpaired t-test, one-way or two-way ANOVA followed by Bonferroni correction when appropriate. Survival curves were created using Kaplan-Mayer method and survival curves were compared with a log-rank test. Data is presented as mean ± SEM and $P < 0.05$ was considered significant. Statistical analyses was performed with GraphPad Prism software (GraphPad Software, La Jolla, CA, USA).

Data Availability

No datasets were generated or analyzed during the current study.

References

1. Aspelund, A., Robciuc, M. R., Karaman, S., Makinen, T. & Alitalo, K. Lymphatic System in Cardiovascular Medicine. *Circ. Res.* **118**, 515–530 (2016).
2. Kim, K. W. & Song, J. H. Emerging Roles of Lymphatic Vasculature in Immunity. *Immune Netw.* **17**, 68–76 (2017).
3. Breslin, J. W. Mechanical forces and lymphatic transport. *Microvasc. Res.* **96**, 46–54 (2014).
4. Martel, C. *et al*. Lymphatic vasculature mediates macrophage reverse cholesterol transport in mice. *J. Clin. Invest.* **123**, 1571–1579 (2013).
5. Milasan, A., Ledoux, J. & Martel, C. Lymphatic network in atherosclerosis: the underestimated path. *Future Sci. OA* **1**, FSO61 (2015).
6. Vuorio, T. *et al*. Lymphatic vessel insufficiency in hypercholesterolemic mice alters lipoprotein levels and promotes atherogenesis. *Arterioscler. Thromb. Vasc. Biol.* **34**, 1162–1170 (2014).
7. Vuorio, T., Tirronen, A. & Yla-Herttuala, S. Cardiac Lymphatics - A New Avenue for Therapeutics? *Trends Endocrinol. Metab.* **28**, 285–296 (2017).
8. Huang, L. H., Lavine, K. J. & Randolph, G. J. Cardiac Lymphatic Vessels, Transport, and Healing of the Infarcted Heart. *JACC Basic Transl. Sci.* **2**, 477–483 (2017).
9. Klotz, L. *et al*. Cardiac lymphatics are heterogeneous in origin and respond to injury. *Nature* **522**, 62–67 (2015).
10. Flaht-Zabost, A. *et al*. Cardiac mouse lymphatics: developmental and anatomical update. *Anat. Rec. (Hoboken)* **297**, 1115–1130 (2014).
11. Kholova, I. *et al*. Lymphatic vasculature is increased in heart valves, ischaemic and inflamed hearts and in cholesterol-rich and calcified atherosclerotic lesions. *Eur. J. Clin. Invest.* **41**, 487–497 (2011).

12. Ratajska, A. *et al*. Comparative and developmental anatomy of cardiac lymphatics. *Scientific World Journal* **2014**, 183170 (2014).
13. Norman, S. & Riley, P. R. Anatomy and development of the cardiac lymphatic vasculature: Its role in injury and disease. *Clin. Anat.* **29**, 305–315 (2016).
14. Cui, Y. The role of lymphatic vessels in the heart. *Pathophysiology* **17**, 307–314 (2010).
15. Sun, Q. N., Wang, Y. F. & Guo, Z. K. Reconstitution of myocardial lymphatic vessels after acute infarction of rat heart. *Lymphology* **45**, 80–86 (2012).
16. Henri, O. *et al*. Selective Stimulation of Cardiac Lymphangiogenesis Reduces Myocardial Edema and Fibrosis Leading to Improved Cardiac Function Following Myocardial Infarction. *Circulation* **133**, 1484–97; discussion 1497 (2016).
17. Hartikainen, J. *et al*. Adenoviral intramyocardial VEGF-DDeltaNDeltaC gene transfer increases myocardial perfusion reserve in refractory angina patients: a phase I/IIa study with 1-year follow-up. *Eur. Heart J.* **38**, 2547–2555 (2017).
18. Merentie, M. *et al*. Mouse ECG findings in aging, with conduction system affecting drugs and in cardiac pathologies: Development and validation of ECG analysis algorithm in mice. *Physiol. Rep*. **3**, https://doi.org/10.14814/phy2.12639 (2015).
19. Alitalo, K. The lymphatic vasculature in disease. *Nat. Med.* **17**, 1371–1380 (2011).
20. Davis, K. L. *et al*. Effects of myocardial edema on the development of myocardial interstitial fibrosis. *Microcirculation* **7**, 269–280 (2000).
21. Beyers, R. J. *et al*. T(2) -weighted MRI of post-infarct myocardial edema in mice. *Magn. Reson. Med.* **67**, 201–209 (2012).
22. Garcia-Dorado, D. *et al*. Analysis of myocardial oedema by magnetic resonance imaging early after coronary artery occlusion with or without reperfusion. *Cardiovasc. Res.* **27**, 1462–1469 (1993).
23. Eitel, I. & Friedrich, M. G. T2-weighted cardiovascular magnetic resonance in acute cardiac disease. *J. Cardiovasc. Magn. Reson.* **13**, 13-429X–13-13 (2011).
24. Heinolainen, K. *et al*. VEGFR3 Modulates Vascular Permeability by Controlling VEGF/VEGFR2 Signaling. *Circ. Res.* **120**, 1414–1425 (2017).
25. Talman, V. & Ruskoaho, H. Cardiac fibrosis in myocardial infarction-from repair and remodeling to regeneration. *Cell Tissue Res.* **365**, 563–581 (2016).
26. Musthafa, H. S. *et al*. Longitudinal rotating frame relaxation time measurements in infarcted mouse myocardium *in vivo*. *Magn. Reson. Med.* **69**, 1389–1395 (2013).
27. Yla-Herttuala, E., Laidinen, S., Laakso, H. & Liimatainen, T. Quantification of myocardial infarct area based on TRAFFn relaxation time maps - comparison with cardiovascular magnetic resonance late gadolinium enhancement, T1rho and T2 *in vivo*. *J. Cardiovasc. Magn. Reson.* **20**, 34-018–0463-x (2018).
28. Joukov, V. *et al*. A novel vascular endothelial growth factor, VEGF-C, is a ligand for the Flt4 (VEGFR-3) and KDR (VEGFR-2) receptor tyrosine kinases. *EMBO J.* **15**, 1751 (1996).
29. Achen, M. G. *et al*. Vascular endothelial growth factor D (VEGF-D) is a ligand for the tyrosine kinases VEGF receptor 2 (Flk1) and VEGF receptor 3 (Flt4). *Proc. Natl. Acad. Sci. USA* **95**, 548–553 (1998).
30. Karaman, S. *et al*. Blockade of VEGF-C and VEGF-D modulates adipose tissue inflammation and improves metabolic parameters under high-fat diet. *Mol. Metab.* **4**, 93–105 (2014).
31. Makinen, T. *et al*. Inhibition of lymphangiogenesis with resulting lymphedema in transgenic mice expressing soluble VEGF receptor-3. *Nat. Med.* **7**, 199–205 (2001).
32. Karkkainen, M. J. *et al*. A model for gene therapy of human hereditary lymphedema. *Proc. Natl. Acad. Sci. USA* **98**, 12677–12682 (2001).
33. Nilsson, J. C. *et al*. Sustained postinfarction myocardial oedema in humans visualised by magnetic resonance imaging. *Heart* **85**, 639–642 (2001).
34. Ludwig, L. L. *et al*. Impairment of left ventricular function by acute cardiac lymphatic obstruction. *Cardiovasc. Res.* **33**, 164–171 (1997).
35. Bunch, T. J., Hohnloser, S. H. & Gersh, B. J. Mechanisms of sudden cardiac death in myocardial infarction survivors: insights from the randomized trials of implantable cardioverter-defibrillators. *Circulation* **115**, 2451–2457 (2007).
36. Laine, G. A. & Allen, S. J. Left ventricular myocardial edema. Lymph flow, interstitial fibrosis, and cardiac function. *Circ. Res.* **68**, 1713–1721 (1991).
37. Gousopoulos, E., Proulx, S. T., Scholl, J., Uecker, M. & Detmar, M. Prominent Lymphatic Vessel Hyperplasia with Progressive Dysfunction and Distinct Immune Cell Infiltration in Lymphedema. *Am. J. Pathol.* **186**, 2193–2203 (2016).
38. Vieira, J. M. *et al*. The cardiac lymphatic system stimulates resolution of inflammation following myocardial infarction. *J. Clin. Invest.* **128**, 3402–3412 (2018).
39. Mather, A. N., Fairbairn, T. A., Ball, S. G., Greenwood, J. P. & Plein, S. Reperfusion haemorrhage as determined by cardiovascular MRI is a predictor of adverse left ventricular remodelling and markers of late arrhythmic risk. *Heart* **97**, 453–459 (2011).
40. Gao, X. M., Xu, Q., Kiriazis, H., Dart, A. M. & Du, X. J. Mouse model of post-infarct ventricular rupture: time course, strain- and gender-dependency, tensile strength, and histopathology. *Cardiovasc. Res.* **65**, 469–477 (2005).
41. Betgem, R. P. *et al*. Intramyocardial haemorrhage after acute myocardial infarction. *Nat. Rev. Cardiol.* **12**, 156–167 (2015).
42. Fukumura, D. *et al*. Predominant role of endothelial nitric oxide synthase in vascular endothelial growth factor-induced angiogenesis and vascular permeability. *Proc. Natl. Acad. Sci. USA* **98**, 2604–2609 (2001).
43. Rodriguez-Porcel, M. *et al*. Hypercholesterolemia impairs myocardial perfusion and permeability: role of oxidative stress and endogenous scavenging activity. *J. Am. Coll. Cardiol.* **37**, 608–615 (2001).
44. Liimatainen, T. *et al*. MRI contrasts in high rank rotating frames. *Magn. Reson. Med.* **73**, 254–262 (2015).
45. Khan, M. A. *et al*. The follow-up of progressive hypertrophic cardiomyopathy using magnetic resonance rotating frame relaxation times. *NMR Biomed*. **31**, https://doi.org/10.1002/nbm.3871. Epub2017 Dec 15 (2018).
46. Hakkarainen, H. *et al*. MRI relaxation in the presence of fictitious fields correlates with myelin content in normal rat brain. *Magn. Reson. Med.* **75**, 161–168 (2016).
47. Liimatainen, T., Sorce, D. J., O'Connell, R., Garwood, M. & Michaeli, S. MRI contrast from relaxation along a fictitious field (RAFF). *Magn. Reson. Med.* **64**, 983–994 (2010).
48. Gao, E. *et al*. A novel and efficient model of coronary artery ligation and myocardial infarction in the mouse. *Circ. Res.* **107**, 1445–1453 (2010).
49. Turunen, M. P. *et al*. Epigenetic upregulation of endogenous VEGF-A reduces myocardial infarct size in mice. *PLoS One* **9**, e89979 (2014).

Acknowledgements

This study was supported by Finnish Academy Center of Excellence, Finnish Foundation for Cardiovascular Research, ERC Advanced Grant, The Paolo Foundation and Urho Känkänen Foundation.

Author Contributions

T.V. designed the study, performed ultrasound imaging and histology, analyzed the data as well as prepared the figures and wrote the manuscript, E.Y-H. performed MR imaging, analyzed the MRI data and wrote the manuscript, J.P.L. performed confocal microscopy, S.L. operated the animals, T.L. supervised the study and S.Y-H. conceived and supervised the study.

Additional Information

Competing Interests: The authors declare no competing interests.

IV

Lymphatic insufficiency increases cardiac edema and has distinct fibrosis content after myocardial infarction as assessed by magnetic resonance T_{RAFFn} and T_2 relaxation times

Ylä-Herttuala E, Vuorio T, Laidinen S, Ylä-Herttuala S and Liimatainen T

Under review

ELIAS YLÄ-HERTTUALA

Magnetic resonance imaging is a versatile non-invasive imaging tool to characterize soft tissues. Different kinds of contrasts have been used to create medical images, but more specific new contrasts are needed for the characterization of specific pathologies in different tissues. In this thesis, novel rotating relaxation time methods ($T_{1\rho}$ and RAFFn) for creating a unique endogenous contrast was implemented and studied in myocardial infarction in ischemic hearts, and hearts with insufficient lymphatic system mice models.

UNIVERSITY OF
EASTERN FINLAND

uef.fi

**PUBLICATIONS OF
THE UNIVERSITY OF EASTERN FINLAND**
Dissertations in Health Sciences

ISBN 978-952-61-3375-1
ISSN 1798-5706